

## INFORMATION TO USERS

This manuscript has been reproduced from the microfilm master. UMI films the text directly from the original or copy submitted. Thus, some thesis and dissertation copies are in typewriter face, while others may be from any type of computer printer.

**The quality of this reproduction is dependent upon the quality of the copy submitted.** Broken or indistinct print, colored or poor quality illustrations and photographs, print bleedthrough, substandard margins, and improper alignment can adversely affect reproduction.

In the unlikely event that the author did not send UMI a complete manuscript and there are missing pages, these will be noted. Also, if unauthorized copyright material had to be removed, a note will indicate the deletion.

Oversize materials (e.g., maps, drawings, charts) are reproduced by sectioning the original, beginning at the upper left-hand corner and continuing from left to right in equal sections with small overlaps. Each original is also photographed in one exposure and is included in reduced form at the back of the book.

Photographs included in the original manuscript have been reproduced xerographically in this copy. Higher quality 6" x 9" black and white photographic prints are available for any photographs or illustrations appearing in this copy for an additional charge. Contact UMI directly to order.

**UMI<sup>®</sup>**

Bell & Howell Information and Learning  
300 North Zeeb Road, Ann Arbor, MI 48106-1346 USA  
800-521-0600



**University of Alberta**

**Search for Vector Leptoquarks in  
Electron-Positron Annihilations at  $\sqrt{s} = 183$  GeV**

by  
Philip Issa Kayal ©

A thesis  
submitted to the Faculty of Graduate Studies and Research  
in partial fulfillment of the requirements for the degree  
of

**Doctor of Philosophy**

**Department of Physics**

**Edmonton, Alberta**

**Spring 1999**



**National Library  
of Canada**

**Acquisitions and  
Bibliographic Services**

**395 Wellington Street  
Ottawa ON K1A 0N4  
Canada**

**Bibliothèque nationale  
du Canada**

**Acquisitions et  
services bibliographiques**

**395, rue Wellington  
Ottawa ON K1A 0N4  
Canada**

*Your file Votre référence*

*Our file Notre référence*

**The author has granted a non-exclusive licence allowing the National Library of Canada to reproduce, loan, distribute or sell copies of this thesis in microform, paper or electronic formats.**

**The author retains ownership of the copyright in this thesis. Neither the thesis nor substantial extracts from it may be printed or otherwise reproduced without the author's permission.**

**L'auteur a accordé une licence non exclusive permettant à la Bibliothèque nationale du Canada de reproduire, prêter, distribuer ou vendre des copies de cette thèse sous la forme de microfiche/film, de reproduction sur papier ou sur format électronique.**

**L'auteur conserve la propriété du droit d'auteur qui protège cette thèse. Ni la thèse ni des extraits substantiels de celle-ci ne doivent être imprimés ou autrement reproduits sans son autorisation.**

**0-612-39550-2**

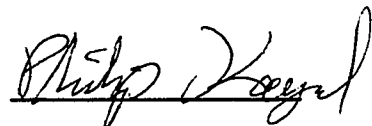
**Canada**

UNIVERSITY OF ALBERTA  
LIBRARY RELEASE FORM

NAME OF AUTHOR: Philip Issa Kayal  
TITLE OF THESIS: Search for Vector Leptoquarks in  
Electron-Positron Annihilations  
at  $\sqrt{s} = 183$  GeV  
DEGREE: Doctor of Philosophy  
YEAR THE DEGREE GRANTED: 1999

Permission is hereby granted to the University of Alberta Library to reproduce single copies of this thesis and to lend or sell such copies for private, scholarly, or scientific research purposes only.

The author reserves all other publication and other rights in association with the copyright in the thesis, and except as hereinbefore provided, neither the thesis nor any substantial portion thereof may be printed or otherwise reproduced in any material form whatever without the author's prior written permission.



Philip Issa Kayal

22 Wellington Ave.

Victoria, B.C.

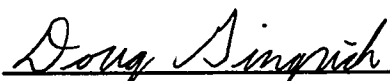
V8V 4H6

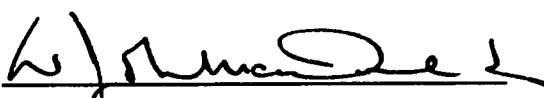
JAN 25, 1999

# UNIVERSITY OF ALBERTA

## FACULTY OF GRADUATE STUDIES AND RESEARCH

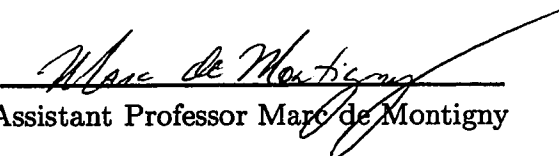
The undersigned certify that they have read, and recommend to the Faculty of Graduate Studies and Research for acceptance, a thesis entitled "Search for Vector Leptoquarks in Electron-Positron Annihilations at  $\sqrt{s} = 183$  GeV", submitted by Philip Issa Kayal in partial fulfillment of the requirements for the degree of Doctor of Philosophy.

  
Associate Professor Douglas M. Gingrich


  
Professor John McDonald

  
Professor Nathan L. Rodning

  
Associate Professor Richard Sydnor

  
Assistant Professor Marc de Montigny

Date: 20 JAN. 1999

  
Associate Professor Kenneth J. Ragan

# Abstract

This thesis presents the results of a search for vector leptoquarks in electron-positron annihilations using data collected with the OPAL detector at LEP. The search was performed using a data sample of  $55.9 \text{ pb}^{-1}$  at a centre-of-mass energy of 183 GeV. The leptoquarks are assumed to be produced in pairs through gauge couplings to the photon and the  $Z^0$ . A total of 8 candidate events are found in the data. There is an expectation of 8.7 events from Standard Model processes. Lower limits on vector leptoquark masses are presented. For all types of vector leptoquarks, the lower limit on the mass is determined to be greater than  $84 \text{ GeV}/c^2$ , at the 95% confidence level. This is close to the kinematic threshold of  $91.5 \text{ GeV}/c^2$ .

## Acknowledgements

I would like to thank Dr. Douglas M. Gingrich of the University of Alberta for his interest in and support of my leptoquark research during the last three years, and in fact for being my supervisor for the past five years.

Dr. Marco Cuffiani and Luca Brigliadori of the University of Bologna deserve my thanks for the numerous useful discussions we have had, and for their valuable contributions to leptoquark research within the OPAL collaboration.

The members of the examining committee have my gratitude for their many useful comments.

Finally, I would like to thank all of my friends and colleagues for their support.

# Contents

**Abstract**

**Acknowledgements**

**Contents**

**List of Tables**

**List of Figures**

<b>1</b>	<b>Introduction</b>	<b>1</b>
<b>2</b>	<b>Physics Motivation</b>	<b>3</b>
2.1	Leptoquark-Fermion Interactions . . . . .	5
2.2	Leptoquark Interactions with the Photon and the Z Boson . . . . .	7
2.3	Effective Lagrangian . . . . .	9
2.4	Feynman Rules . . . . .	10
2.5	Production Cross-Sections . . . . .	10
2.5.1	Scalar Leptoquarks . . . . .	12
2.5.2	Vector Leptoquarks . . . . .	14
2.5.3	Leptoquark Widths . . . . .	16
2.5.4	Coupling Strengths and Branching Fractions . . . . .	16

2.6	Previous Searches for Leptoquarks . . . . .	18
2.7	Leptoquarks at LEP . . . . .	23
<b>3</b>	<b>The LEP Collider</b>	<b>25</b>
<b>4</b>	<b>The OPAL Detector</b>	<b>28</b>
4.1	Overview . . . . .	28
4.2	The Magnet and Beam Pipe . . . . .	31
4.3	The Central Detector . . . . .	31
4.3.1	Silicon Microvertex Detector . . . . .	32
4.3.2	Vertex Chamber . . . . .	32
4.3.3	Jet Chamber . . . . .	34
4.3.4	Z-Chambers . . . . .	35
4.4	Electromagnetic Calorimeter . . . . .	35
4.4.1	Time-of-Flight Systems . . . . .	36
4.4.2	Barrel Electromagnetic Presampler . . . . .	36
4.4.3	Barrel Lead Glass Calorimeter . . . . .	37
4.4.4	Endcap Electromagnetic Presampler . . . . .	37
4.4.5	Endcap Electromagnetic Calorimeter . . . . .	37
4.5	Hadron Calorimeter . . . . .	38
4.5.1	Barrel and Endcap Hadron Calorimeters . . . . .	38

4.5.2	Pole-Tip Hadron Calorimeter . . . . .	39
4.6	Muon Detector . . . . .	39
4.6.1	Barrel Muon Detector . . . . .	40
4.6.2	Endcap Muon Detector . . . . .	40
4.7	Forward Detector . . . . .	41
4.8	Silicon Tungsten Detector . . . . .	42
4.9	The Trigger . . . . .	43
4.10	Online Data Acquisition System . . . . .	43
<b>5</b>	<b>Leptoquark Simulation and Search</b>	<b>45</b>
5.1	General Method of Searching for Evidence of Vector Leptoquarks . . . .	46
5.2	Simulated Signal Events . . . . .	48
5.3	Simulated Background Events . . . . .	49
5.4	Selection Criteria . . . . .	51
5.4.1	Preselection Criteria . . . . .	53
5.4.2	Type A Selection Criteria . . . . .	54
5.4.3	Type B Selection Criteria . . . . .	55
5.4.4	Type C Selection Criteria . . . . .	56
5.5	Effect of Selection Criteria on Signal . . . . .	57
5.6	Effect of Selection Criteria on Backgrounds . . . . .	64

5.7	183 GeV Data Sample . . . . .	76
5.8	Comparison of Simulated Data to OPAL Data . . . . .	77
<b>6</b>	<b>Limits on Vector Leptoquark Production</b>	<b>89</b>
6.1	Determination of Upper Limits on the Leptoquark Production Cross- Section . . . . .	90
6.2	Determination of Leptoquark Mass Limits . . . . .	92
6.2.1	Vector Leptoquarks Which Have a Fixed Value of $\beta$ . . . . .	94
6.2.2	Vector Leptoquarks Which Do Not Have a Fixed Value of $\beta$ . . . . .	99
6.2.3	Upper Limit on Production Cross-Section as a Function of $\beta$ . . .	104
6.3	Discussion of Uncertainties . . . . .	107
<b>7</b>	<b>Summary</b>	<b>109</b>

# List of Tables

2.1	Quantum numbers and couplings to lepton-quark pairs, for the leptons which appear in the Lagrangian. $D$ is the dimension in $SU(2)$ , $F$ is the fermion number, $T_3$ is the third component of isospin, $Q_{em}$ is the electromagnetic charge, and $g$ and $h$ are general couplings to lepton-quark pairs. . . . .	8
2.2	A summary of the most recent leptoquark mass lower limits obtained by various experiments, including the assumptions that were made. The mass limits are all at the 95% confidence level. . . . .	22
5.1	Cross-section for hadronic events from $e^+e^- \rightarrow Z^{0*}/\gamma^* \rightarrow q\bar{q}(\gamma)$ at 183 GeV (PYTHIA). . . . .	49
5.2	Cross-sections for two-photon hadronic events (1018 (PHOJET) and 1126 (HERWIG)) and two-photon eel (VERMASEREN) at 183/4 GeV. . . . .	50
5.3	Cross-sections for neutral current eeff via s-channel ( $\gamma/Z$ - $\gamma/Z$ ) and t-channel ( $\gamma/Z$ - $ee$ ) (GRC4F) at 183/4 GeV. . . . .	50
5.4	Cross-sections for neutral current ( <i>eg.</i> $Z\gamma$ , $ZZ$ ) and charged current ( <i>eg.</i> $WW$ , $W\epsilon\nu$ ) processes (final states: $qqqq$ , $llqq$ , $llll$ ) (GRC4F) at 183/4 GeV. . . . .	50
5.5	Number of events remaining after selection criteria have been applied, and corresponding efficiency for first-generation decays via Topology A. . . . .	58

5.6	Number of events remaining after selection criteria have been applied, and corresponding efficiency for first-generation decays via Topology B. . . . .	58
5.7	Number of events remaining after selection criteria have been applied, and corresponding efficiency for first-generation decays via Topology C. . . . .	59
5.8	Number of events remaining after selection criteria have been applied, and corresponding efficiency for second-generation decays via Topol- ogy A. . . . .	59
5.9	Number of events remaining after selection criteria have been applied, and corresponding efficiency for second-generation decays via Topol- ogy B. . . . .	60
5.10	Number of events remaining after selection criteria have been applied, and corresponding efficiency for second-generation decays via Topol- ogy C. . . . .	60
5.11	Number of events remaining after each successive cut, for type A selection criteria. (Runs 5050, 1018 & 1126.) . . . . .	64
5.12	Number of events remaining after each successive cut, for type A selection criteria. (Runs 1005, 1013 & 1786.) . . . . .	65
5.13	Number of events remaining after each successive cut, for type A selection criteria. (Runs 6819, 6615, 6616 & 7055.) . . . . .	65
5.14	Number of events remaining after each successive cut, for type A selection criteria. (Runs 7051, 7050 & 6641.) . . . . .	66

5.15	Number of events remaining after each successive cut, for type B selection criteria. (Runs 5050, 1018 & 1126.) . . . . .	66
5.16	Number of events remaining after each successive cut, for type B selection criteria. (Runs 1005, 1013 & 1786.) . . . . .	67
5.17	Number of events remaining after each successive cut, for type B selection criteria. (Runs 6819, 6615, 6616 & 7055.) . . . . .	67
5.18	Number of events remaining after each successive cut, for type B selection criteria. (Runs 7051, 7050 & 6641.) . . . . .	68
5.19	Number of events remaining after each successive cut, for type C selection criteria. (Runs 5050, 1018 & 1126.) . . . . .	68
5.20	Number of events remaining after each successive cut, for type C selection criteria. (Runs 1005, 1013 & 1786.) . . . . .	69
5.21	Number of events remaining after each successive cut, for type C selection criteria. (Runs 6819, 6615, 6616 & 7055.) . . . . .	69
5.22	Number of events remaining after each successive cut, for type C selection criteria. (Runs 7051, 7050 & 6641.) . . . . .	70
5.23	Number of events processed and the number of events which pass the selection criteria for each topology (A, B and C) and for each back- ground process (by run number). . . . .	71
5.24	Number of background events in the $55.9 \text{ pb}^{-1}$ of data that are expected to pass the selection criteria, including statistical uncertainties, for each of the background processes and for each of the three sets of selection criteria. . . . .	73

5.25	The number of data events which pass each set of selection criteria, in the 55.9 pb <sup>-1</sup> of data recorded by OPAL in 1997, at a centre-of-mass energy of 183 GeV. . . . .	76
6.1	Expected number of background events to pass the selection criteria for 55.9 pb <sup>-1</sup> of data, and actual number of data events in 55.9 pb <sup>-1</sup> of data which pass the selection criteria, for all three topologies. . . . .	90
6.2	Allowed value(s) of $\beta$ for each vector leptoquark. . . . .	93
6.3	Lower limits on the mass of those vector leptoquarks which have a fixed value of $\beta$ , for both first- and second-generation, at the 95% confidence level. . . . .	97

# List of Figures

2.1	A general leptoquark vertex, showing a leptoquark (LQ) coupling to a lepton (l) and a quark (q). l is a generic lepton or anti-lepton, and q is a generic quark or anti-quark. . . . .	4
2.2	Lowest-order Feynman diagrams for leptoquark pair-production in $e^+e^-$ annihilations. The top diagram is the s-channel process; the lower diagram is the t-channel process. . . . .	11
2.3	Production cross-section as a function of leptoquark mass for all nine vector leptoquarks, at a centre-of-mass energy of 183 GeV. The couplings $\lambda_{L,R}$ are set to 0.001. . . . .	17
3.1	The LEP collider at CERN, showing the location of the four $e^+e^-$ interaction points. Also shown are the PS and SPS accelerators. . . . .	27
4.1	A cutaway view of the OPAL detector. . . . .	29
4.2	A cutaway view of the OPAL Silicon Microvertex Detector. . . . .	33
4.3	The OPAL Vertex Chamber. . . . .	34
4.4	Cross-sectional view of the OPAL Forward Detector region. . . . .	41
5.1	( <i>top</i> ) Definition of branching fraction (also known as branching ratio (BR)); ( <i>bottom</i> ) the three decay topologies (A, B & C left-to-right) available to pair-produced leptoquarks. . . . .	47

5.2	Flow chart showing the steps taken in the production and analysis of simulated signal and background events, and in the analysis of OPAL data. . . . .	52
5.3	Signal efficiency versus leptoquark mass for all three topologies (C, B & A), for first-generation leptoquarks. . . . .	62
5.4	Signal efficiency versus leptoquark mass for all three topologies (C, B & A), for second-generation leptoquarks. . . . .	63
5.5	The visible energy after the preselection criteria have been applied, for both the 183 GeV data sample, and the total of the simulated background processes. (Energy is in GeV.) . . . . .	78
5.6	The cosine of the angle between the missing momentum and the z-axis, after the selection criterion A1 has been applied (for Topology A selection criteria), for both the 183 GeV data sample, and the total of the simulated background processes. Also shown is the same variable, for simulated first-generation 90 GeV/c <sup>2</sup> leptoquark pair-production and subsequent decay via Topology A. . . . .	79
5.7	The amount of missing transverse momentum, after the selection criterion A2 has been applied (for Topology A selection criteria), for both the 183 GeV data sample, and the total of the simulated background processes. Also shown is the same variable, for simulated first-generation 90 GeV/c <sup>2</sup> leptoquark pair-production and subsequent decay via Topology A. . . . .	81

5.8	The value of $Y_{23}$ (the resolution parameter when reconstructing events into four jets using the Durham algorithm), after the selection criterion A3 has been applied (for Topology A selection criteria), for both the 183 GeV data sample, and the total of the simulated background processes. Also shown is the same variable, for simulated first-generation 90 GeV/c <sup>2</sup> leptoquark pair-production and subsequent decay via Topology A. . . . .	82
5.9	The cosine of the angle between the missing momentum and the $z$ -axis, after the selection criterion B1 has been applied (for Topology B selection criteria), for both the 183 GeV data sample, and the total of the simulated background processes. Also shown is the same variable, for simulated first-generation 90 GeV/c <sup>2</sup> leptoquark pair-production and subsequent decay via Topology B. . . . .	83
5.10	Histogram of $R_{mis}$ (the ratio between missing momentum and $\sqrt{s}$ ), after the selection criterion B2 has been applied (for Topology B selection criteria), for both the 183 GeV data sample, and the total of the simulated background processes. Also shown is the same variable, for simulated first-generation 90 GeV/c <sup>2</sup> leptoquark pair-production and subsequent decay via Topology B. . . . .	84

5.11	The value of $Y_{43}$ (the resolution parameter when reconstructing events into four jets using the Durham algorithm), after the selection criterion C1 has been applied (for Topology C selection criteria), for both the 183 GeV data sample, and the total of the simulated background processes. Also shown is the same variable, for simulated first-generation 90 GeV/c <sup>2</sup> leptoquark pair-production and subsequent decay via Topology C. . . . .	85
5.12	The energy of the most energetic electron, after the selection criterion C3 has been applied (for Topology C selection criteria), for both the 183 GeV data sample, and the total of the simulated background processes. Also shown is the same variable, for simulated first-generation 90 GeV/c <sup>2</sup> leptoquark pair-production and decay via Topology C. . .	87
5.13	The energy of the most energetic positron, after the selection criterion C3 has been applied (for Topology C selection criteria), for both the 183 GeV data sample, and the total of the simulated background processes. Also shown is the same variable, for simulated first-generation 90 GeV/c <sup>2</sup> leptoquark pair-production and decay via Topology C. . .	88
6.1	Upper limit on the cross-section at the 95% confidence level as a function of leptoquark mass, for $\beta = 0$ . Also shown are the theoretical cross-sections for the leptoquarks (1) $^{-2/3}\tilde{V}_2$ and (2) $^{-1/3}U_3$ . . . . .	95
6.2	Upper limit on the cross-section at the 95% confidence level as a function of leptoquark mass, for $\beta = 0.5$ . Also shown is the theoretical cross-section for the leptoquark (1) $^{2/3}U_3$ . . . . .	96

6.3	Upper limit on the cross-section at the 95% confidence level as a function of leptoquark mass, for $\beta = 1.0$ . Also shown are the theoretical cross-sections for the leptoquarks (1) $^{1/3}\tilde{V}_2$ , (2) $^{4/3}V_2$ , (3) $^{5/3}\tilde{U}_1$ and (4) $^{5/3}U_3$ .	98
6.4	The upper limit on the cross-section at the 95% confidence level as a function of mass, for various values of $\beta$ , for both first- and second-generation leptoquarks. Also shown is the theoretical cross-section for the leptoquark (1) $^{1/3}V_2$ .	100
6.5	$\beta$ versus lower limit on the mass of the vector leptoquark $^{1/3}V_2$ , for both first- and second-generation at the 95% confidence level.	101
6.6	The upper limit on the cross-section at the 95% confidence level as a function of mass, for various values of $\beta$ , for both first- and second-generation leptoquarks. Also shown is the theoretical cross-section for the leptoquark (1) $^{2/3}U_1$ .	102
6.7	$\beta$ versus lower limit on the mass of the vector leptoquark $^{2/3}U_1$ , for both first- and second-generation at the 95% confidence level.	103
6.8	Upper limit on the production cross-section versus $\beta$ , for both first- and second-generation leptoquarks, at the 95% confidence level, assuming a leptoquark mass of 85 GeV/c <sup>2</sup> .	105
6.9	Upper limit on the production cross-section versus $\beta$ , for both first- and second-generation leptoquarks, at the 95% confidence level, assuming a leptoquark mass of 90 GeV/c <sup>2</sup> .	106

# CHAPTER 1

## Introduction

The Standard Model [1] of particles and interactions has been very successful in describing observed subatomic physical phenomena. However, the Standard Model has several shortcomings, such as: there is no explanation for the family and multiplet structure of the fermions, there are many free parameters, the interaction of gravity is not included, and there is no explanation for charge quantization. For this reason, the Standard Model is only an effective theory; that is, a low energy approximation of a more fundamental theory.

There are many theories which attempt to provide explanations which are lacking in the Standard Model. Some of these theories allow couplings between leptons and quarks (a feature which is not described in the Standard Model), and hence predict the existence of a boson called a leptoquark. Leptoquarks could exist in scalar and vector spin states.

It may be possible to pair-produce leptoquarks in electron-positron annihilations at high energies. Scalar leptoquarks have been searched for previously, but vector leptoquarks have received little attention. A search for vector leptoquarks is presented. It was performed using the LEP (Large Electron Positron) collider at CERN (the European Laboratory for Particle Physics, located in Geneva, Switzerland). LEP accelerates electrons and positrons in opposite directions along a circular path, and collides them at centre-of-mass energies of up to 189 GeV (achieved in

1998). The data sample analyzed was recorded by the OPAL (Omni-Purpose Apparatus for LEP) detector in 1997, and consists of electron-positron collisions at a centre-of-mass energy of 183 GeV. OPAL is a large, general-purpose detector, designed to reliably study the interactions which occur in electron-positron collisions.

The pair-production of vector leptoquarks in electron-positron collisions and their subsequent decay was simulated, for various leptoquark masses, at a centre-of-mass energy of 183 GeV. Also simulated were the relevant background processes, which yield decay products similar to those of pair-produced leptoquarks. The simulated signal samples and background processes were passed through a full simulation of the OPAL detector. Various kinematic selection criteria were applied to both the simulated signal events and the simulated background events. These selection criteria are designed to reject most of the background events, while preserving as many of the signal events as possible.

The selection criteria were then applied to the previously mentioned data sample. By comparing the results of the simulation studies with the result of the search through real data, we draw conclusions about the existence of vector leptoquarks, and place limits on various parameters. No evidence for leptoquarks with mass below  $86 \text{ GeV}/c^2$  is observed.

## CHAPTER 2

### Physics Motivation

In the Standard Model of particles and interactions, the fundamental particles are divided into two categories: fermions, which are the matter constituents, and bosons, which mediate interactions. The fermions are either quarks or leptons. The quarks and the leptons can each be divided into three families which exhibit similar properties in the Standard Model:

$$\begin{aligned} \text{Quarks : } & \begin{pmatrix} u \\ d \end{pmatrix}, \begin{pmatrix} c \\ s \end{pmatrix}, \begin{pmatrix} t \\ b \end{pmatrix} \\ \text{Leptons : } & \begin{pmatrix} \nu_e \\ e \end{pmatrix}, \begin{pmatrix} \nu_\mu \\ \mu \end{pmatrix}, \begin{pmatrix} \nu_\tau \\ \tau \end{pmatrix}. \end{aligned}$$

Each family is represented by a column vector of up and down type quarks (and their anti-particles), or a neutrino and a charged lepton (and their anti-particles). The first-generation family of fermions consists of  $u$ ,  $d$ ,  $\nu_e$ ,  $e$  and their anti-particles; the second-generation family of fermions consists of  $c$ ,  $s$ ,  $\nu_\mu$ ,  $\mu$  and their anti-particles; and the third-generation family of fermions consists of  $t$ ,  $b$ ,  $\nu_\tau$ ,  $\tau$  and their anti-particles.

The quarks and leptons are very similar with respect to the family and multiplet structure of electroweak interactions. Furthermore, the parallel assignment of quarks and leptons is necessary to cancel triangle anomalies, ensuring that the Standard Model is a consistent quantum field theory [2]. However, the Standard Model does not provide a motivation for the generation structure of the fermions,

nor does it explain the symmetry between the quark and lepton families.

The structure and symmetry of the fermion families could result from a more fundamental theory of quarks and leptons. Such a theory is expected to include new bosonic fields which would mediate lepton-quark transitions. Examples of such theories include Grand Unified Theories [3], the Pati-Salam  $SU(4)$  model [4], technicolour models [5], and compositeness models [6]. These new bosonic fields could allow for baryon and lepton number non-conservation, as well as flavour changing neutral current processes [7]. However, there are strong experimental bounds on this possibility, from proton lifetime measurements and rare processes. But, bosons which only couple to lepton-quark pairs, called *leptoquarks* (LQ), are fairly weakly constrained if the couplings are restricted to a single fermion family.

Figure 2.1 shows a general vertex for a leptoquark coupling to a lepton-quark pair. The lepton and the quark must belong to the same fermion family.

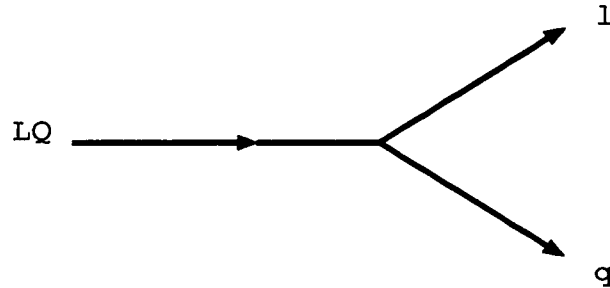


Figure 2.1: A general leptoquark vertex, showing a leptoquark (LQ) coupling to a lepton ( $l$ ) and a quark ( $q$ ).  $l$  is a generic lepton or anti-lepton, and  $q$  is a generic quark or anti-quark.

As a minimal requirement, it is assumed that the Lagrangian (density) describing the interactions of leptoquarks with the known particles respects the

$SU(3)_c \times SU(2)_L \times U(1)_Y$  group symmetry of the Standard Model. With this general assumption, only the leptoquark masses and the strengths of the leptoquark couplings,  $\lambda_{L,R}$ , to left- and right-handed fermions respectively, remain as free parameters. The couplings to the gauge bosons and the representations of the leptoquarks are completely determined by the electric charge and the third component of weak isospin. This results in nine scalar and nine vector leptoquarks, which in both cases are grouped into two weak isospin singlets, two doublets and one triplet.

Leptoquark interactions are further assumed to conserve lepton and baryon number, and so leptoquarks must be assigned lepton and baryon numbers. Finally, leptoquarks are assumed to couple diagonally, *i.e.* within a single fermion generation.

## 2.1 Leptoquark-Fermion Interactions

The interactions of leptoquarks with the known particles can be described by an effective Lagrangian, valid at low energies. This study is intended to be largely model-independent, however a few basic assumptions must be made. As mentioned previously, we demand that the effective Lagrangian respects the  $SU(3)_c \times SU(2)_L \times U(1)_Y$  symmetry of the Standard Model. Other assumptions that are made are that the couplings of leptoquarks to lepton-quark pairs are dimensionless, family-diagonal, and baryon and lepton number conserving.

Non-diagonal terms in the coupling matrix of a leptoquark to quarks and leptons are constrained by low energy measurements [7]. For example, limits on the branching fractions of  $K^+ \rightarrow \pi^+ \nu \bar{\nu}$  [8] and  $D^0 \rightarrow \mu^+ \mu^-$  [9] decays constrain the non-diagonal coupling strengths to about  $5 \times 10^{-5}$  for the first two generations.

Leptoquarks can exist as both scalar (spin 0) and vector (spin 1) particles. They carry both lepton (L) and baryon (B) quantum numbers. There are two classes of leptoquarks: colour triplets under  $SU(3)_c$  with fermion number  $|F| = 2$  (where  $F = 3B + L$ ), and colour anti-triplets with fermion number  $F = 0$ . The weak isospin can be 0,  $\frac{1}{2}$ , or 1.

Since the couplings are assumed to be family-diagonal, we can consider only the first generation, and can exchange first-generation fermions with the corresponding second- or third-generation fermions (in the massless limit) in the final result if we wish.

The effective Lagrangian ( $\mathcal{L}^f$ ) describing interactions between leptoquarks and fermions consists of the following two parts [10]:

$$\begin{aligned} \mathcal{L}_{|F|=2}^f = & (g_{1L}\bar{q}_L^c i\tau_2 l_L + g_{1R}\bar{u}_R^c e_R)S_1 + \tilde{g}_{1R}\bar{d}_R^c e_R\tilde{S}_1 + g_{3L}\bar{q}_L^c i\tau_2 \vec{\tau} l_L \vec{S}_3 \\ & + (g_{2L}\bar{d}_R^c \gamma^\mu l_L + g_{2R}\bar{q}_L^c \gamma^\mu e_R)\tilde{V}_{2\mu} + \tilde{g}_{2L}\bar{u}_R^c \gamma^\mu l_L \tilde{V}_{2\mu} + h.c., \end{aligned} \quad (2.2.1.1)$$

and

$$\begin{aligned} \mathcal{L}_{F=0}^f = & (h_{2L}\bar{u}_R l_L + h_{2R}\bar{q}_L i\tau_2 e_R)R_2 + \tilde{h}_{2L}\bar{d}_R l_L \tilde{R}_2 \\ & + (h_{1L}\bar{q}_L \gamma^\mu l_L + h_{1R}\bar{d}_R \gamma^\mu e_R)U_{1\mu} \\ & + \tilde{h}_{1R}\bar{u}_R \gamma^\mu e_R \tilde{U}_{1\mu} + h_{3L}\bar{q}_L \vec{\tau} \gamma^\mu l_L \vec{U}_{3\mu} + h.c., \end{aligned} \quad (2.2.1.2)$$

where  $F = 3B + L$ ,  $q_L$  and  $l_L$  denote  $SU(2)_L$  quark and lepton doublets, and  $u_R$ ,  $d_R$  and  $e_R$  are the corresponding singlet fields. Charge conjugated fields are denoted by  $f^c$ , and  $\tau_i$  are the Pauli matrices. The Hermitian conjugate terms are denoted by  $h.c.$  The colour and family indices have been suppressed for simplicity. The couplings are denoted by  $g$  and  $h$ .

One can produce a table showing the quantum numbers and couplings to lepton-quark pairs for each of the leptoquark species which appear in the Lagrangian

(Table 2.1). We have adopted the notation of reference [10]. The leptoquarks  $S_1$ ,  $\tilde{S}_1$ ,  $\tilde{S}_3$ ,  $V_{2\mu}$ ,  $\tilde{V}_{2\mu}$ ,  $U_{1\mu}$ ,  $\tilde{U}_{1\mu}$ ,  $\tilde{U}_{3\mu}$ ,  $R_2$ ,  $\tilde{R}_2$  correspond to  $S_0$ ,  $\tilde{S}_0$ ,  $S_1$ ,  $V_{1/2}$ ,  $\tilde{V}_{1/2}$ ,  $V_0$ ,  $\tilde{V}_0$ ,  $V_1$ ,  $S_{1/2}$ ,  $\tilde{S}_{1/2}$  in reference [11].

## 2.2 Leptoquark Interactions with the Photon and the Z Boson

The Standard Model is formulated in terms of massless particles. Masses of the heavy gauge bosons  $W^+$ ,  $W^-$  and  $Z^0$  are generated via spontaneous symmetry breaking. To preserve local gauge invariance, we must introduce the covariant derivative

$$D_\mu = \partial_\mu - ieQ^\gamma A_\mu - ieQ^Z Z_\mu. \quad (2.2.2.3)$$

which implements the minimal couplings of leptoquarks to the electroweak gauge bosons. Note that  $A_\mu$  and  $Z_\mu$  are linear combinations of the gauge bosons  $b_\mu^1$ ,  $b_\mu^2$ ,  $b_\mu^3$  (for  $SU(2)_L$ ) and  $\mathcal{A}_\mu$  (for  $U(1)_Y$ ).

For leptoquark couplings to the photon,  $eQ^\gamma$  is the coupling, and  $A_\mu$  is the vector potential describing the electromagnetic field; for couplings to the Z boson,  $eQ^Z$  is the coupling, and  $Z_\mu$  is a vector potential describing the Z boson. Now  $Q^\gamma = Q_{em}$ , the electromagnetic charge of a given leptoquark, while  $Q^Z$  is given by

$$Q^Z = \frac{T_3 - Q_{em}\sin^2\theta_W}{(\cos\theta_W)(\sin\theta_W)}, \quad (2.2.2.4)$$

where  $\theta_W$  is the weak mixing angle, and  $T_3$  is the third component of the weak isospin of the leptoquark.  $Q^Z$  is a combination of the  $U(1)$  quantum number ( $Q_{em}$ ) and the  $SU(2)$  quantum number ( $T_3$ ).

For each scalar leptoquark, we will have a term in the Lagrangian of the form

$$(D^\mu\Phi)^\dagger(D_\mu\Phi) - M_\Phi^2\Phi^\dagger\Phi, \quad (2.2.2.5)$$

$LQ_D$	Spin	F	$T_3$	$Q_{em}$	$\lambda_L(l^\pm q)$	$\lambda_R(l^\pm q)$	$\lambda_L(\nu q)$
$S_1$	0	-2	0	1/3	$g_{1L}$	$g_{1R}$	$-g_{1L}$
$\tilde{S}_1$	0	-2	0	4/3	0	$\tilde{g}_{1R}$	0
$\vec{S}_3$	0	-2	+1	4/3	$-\sqrt{2}g_{3L}$	0	0
			0	1/3	$-g_{3L}$	0	$-g_{3L}$
			-1	-2/3	0	0	$\sqrt{2}g_{3L}$
$R_2$	0	0	1/2	5/3	$h_{2L}$	$h_{2R}$	0
			-1/2	2/3	0	$-h_{2R}$	$h_{2L}$
$\tilde{R}_2$	0	0	1/2	2/3	$\tilde{h}_{2L}$	0	0
			-1/2	-1/3	0	0	$\tilde{h}_{2L}$
$V_{2\mu}$	1	-2	1/2	4/3	$g_{2L}$	$g_{2R}$	0
			-1/2	1/3	0	$g_{2R}$	$g_{2L}$
$\tilde{V}_{2\mu}$	1	-2	1/2	1/3	$\tilde{g}_{2L}$	0	0
			-1/2	-2/3	0	0	$\tilde{g}_{2L}$
$U_{1\mu}$	1	0	0	2/3	$h_{1L}$	$h_{1R}$	$h_{1L}$
$\tilde{U}_{1\mu}$	1	0	0	5/3	0	$\tilde{h}_{1R}$	0
$\vec{U}_{3\mu}$	1	0	+1	5/3	$\sqrt{2}h_{3L}$	0	0
			0	2/3	$-h_{3L}$	0	$h_{3L}$
			-1	-1/3	0	0	$\sqrt{2}h_{3L}$

Table 2.1: Quantum numbers and couplings to lepton-quark pairs, for the lepto-quarks which appear in the Lagrangian.  $D$  is the dimension in  $SU(2)$ ,  $F$  is the fermion number,  $T_3$  is the third component of isospin,  $Q_{em}$  is the electromagnetic charge, and  $g$  and  $h$  are general couplings to lepton-quark pairs.

where the field  $\Phi$  represents a scalar leptoquark, and  $M_\Phi$  is the mass of the leptoquark.

For each vector leptoquark, we will have a term in the Lagrangian of the form

$$-\frac{1}{2}G_{\mu\nu}^\dagger G^{\mu\nu} + M_\Phi^2 \Phi^{\mu\dagger} \Phi_\mu. \quad (2.2.2.6)$$

where the field  $\Phi^\mu$  represents a vector leptoquark, and the field strength tensor  $G_{\mu\nu}$  is defined as:

$$G_{\mu\nu} = D_\mu \Phi_\nu - D_\nu \Phi_\mu. \quad (2.2.2.7)$$

## 2.3 Effective Lagrangian

We are now ready to construct the effective Lagrangian density.

The most general effective Lagrangian describing the interactions of scalar and vector leptoquarks with fermions ( $\mathcal{L}^f$ ) and the neutral electroweak gauge bosons ( $\mathcal{L}^{\gamma,Z}$ ), is

$$\mathcal{L} = \mathcal{L}_{|F|=2}^f + \mathcal{L}_{F=0}^f + \mathcal{L}^{\gamma,Z}. \quad (2.2.3.8)$$

We require that baryon (B) and lepton (L) number are conserved, that the couplings to lepton-quark pairs are family-diagonal, and that we have  $SU(3)_c \times SU(2)_L \times U(1)_Y$  invariance.

In previous sections, we have shown that the interactions of leptoquarks with fermions can be described by Equations 2.2.1.1 ( $\mathcal{L}_{|F|=2}^f$ ) and 2.2.1.2 ( $\mathcal{L}_{|F|=0}^f$ ), and that the interactions of leptoquarks with the photon and Z boson are given by

$$\begin{aligned}
\mathcal{L}^{\gamma,Z} = & \sum_{\text{scalars}} \left[ (D^\mu \Phi)^\dagger (D_\mu \Phi) - M_\Phi^2 \Phi^\dagger \Phi \right] \\
& + \sum_{\text{vectors}} \left( -\frac{1}{2} G_{\mu\nu}^\dagger G^{\mu\nu} + M_\Phi^2 \Phi^{\mu\dagger} \Phi_\mu \right),
\end{aligned} \tag{2.2.3.9}$$

where the fields  $\Phi$  and  $\Phi^\mu$  denote the scalar and vector leptoquarks  $S_1, \tilde{S}_1, \vec{S}_3, R_2, \tilde{R}_2$ , and  $V_2^\mu, \tilde{V}_2^\mu, U_1^\mu, \tilde{U}_1^\mu, \vec{U}_3^\mu$ , respectively.

## 2.4 Feynman Rules

The relevant Feynman rules are applied in the usual manner to interactions between leptoquarks and fermions. It is further assumed that the couplings of scalar leptoquarks to the gauge bosons  $\gamma$  and  $Z^0$  are analogous to W boson couplings to these particles. For a vertex involving a vector leptoquark and a gauge boson, one has the Feynman rule [10]:

$$-ie\mathcal{Q}^{\gamma,Z}(\Phi)[(p+p')_\mu g_{\alpha\beta} - p'_\alpha g_{\beta\mu} - p_\beta g_{\alpha\mu}], \tag{2.2.4.10}$$

where  $p$  and  $p'$  are the ingoing and outgoing momenta respectively.

## 2.5 Production Cross-Sections

The lowest-order Feynman diagrams for leptoquark pair-production in  $e^+e^-$  annihilations are shown in Figure 2.2. There is an s-channel diagram, in which the electron and positron annihilate to form a virtual photon or a virtual Z boson, which then decays into a leptoquark and an anti-leptoquark. In the t-channel diagram, the electron and positron exchange a quark to become a leptoquark and an anti-leptoquark.

The s-channel diagram is available to all leptoquarks because it does not

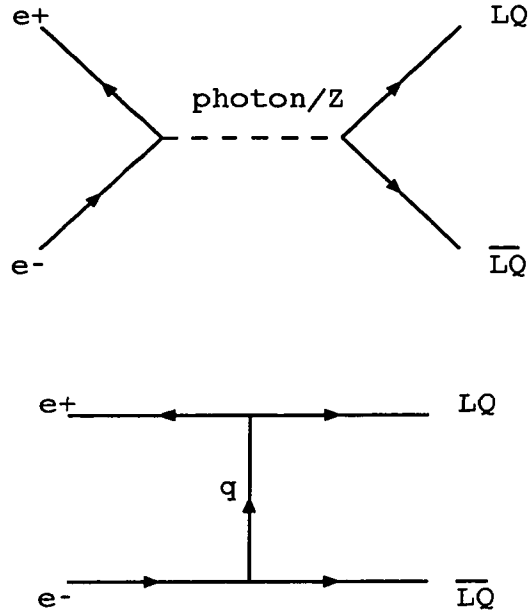


Figure 2.2: Lowest-order Feynman diagrams for leptoquark pair-production in  $e^+e^-$  annihilations. The top diagram is the s-channel process; the lower diagram is the t-channel process.

contain any vertices where a leptoquark couples to fermions. The t-channel diagram is available only to leptoquarks which couple to first-generation fermions.

Application of the usual Feynman rules for the process  $e^+e^- \rightarrow LQ \overline{LQ}$ , considering s-channel  $\gamma$  and  $Z^0$  exchange, and t-channel quark exchange, will lead to the differential scattering cross-section. This result is shown for both scalar and vector leptoquarks in the following sections, in the massless limit of the fermions.

### 2.5.1 Scalar Leptoquarks

For the differential cross-section of scalar leptoquarks, one obtains [10]:

$$\begin{aligned} \frac{d\sigma_{scalar}}{d(\cos \theta)} = & \frac{3\pi\alpha^2}{8s}\beta^3\sin^2\theta \sum_{a=L,R} \left[ |\kappa_a(s)|^2 + \left(\frac{\lambda_a}{e}\right)^2 \frac{4\text{Re}[\kappa_a(s)]}{t(\beta, \cos \theta)} \right. \\ & \left. + \left(\frac{\lambda_a}{e}\right)^4 \frac{4}{t^2(\beta, \cos \theta)} \right], \end{aligned} \quad (2.2.5.11)$$

where

$$\kappa_a(s) = \sum_{V=\gamma,Z} \mathcal{Q}_a^V(e) \frac{s}{s - M_V^2 + iM_V\Gamma_V} \mathcal{Q}^V(\Phi), \quad (2.2.5.12)$$

and  $\theta$  is the angle of a leptoquark with respect to the beam axis. Also,

$$\mathcal{Q}_{L,R}^\gamma(e) = -1. \quad (2.2.5.13)$$

$$\mathcal{Q}_L^Z(e) = \frac{-\frac{1}{2} + \sin^2\theta_W}{(\cos \theta_W)(\sin \theta_W)}. \quad (2.2.5.14)$$

and

$$\mathcal{Q}_R^Z(e) = \tan \theta_W \quad (2.2.5.15)$$

are the relevant electroweak charges for the electron,  $e$ .  $\mathcal{Q}^\gamma(\Phi)$  is the electromagnetic charge of the leptoquark, which is given in Table 2.1, and  $\mathcal{Q}^Z(\Phi)$  is given by Equation 2.2.2.4.  $M_V$  and  $\Gamma_V$  denote the mass and the width of the neutral current gauge bosons. The leptoquark-fermion couplings  $\lambda_{L,R}$  are given in Table 2.1. Also,

$$t(\beta, \cos \theta) = 1 + \beta^2 - 2\beta(\cos \theta), \quad (2.2.5.16)$$

where the kinematic threshold factor  $\beta$  is defined by

$$\beta = \sqrt{1 - \frac{4M_\Phi^2}{s}}, \quad (2.2.5.17)$$

where  $\sqrt{s}$  is the centre-of-mass energy of  $e^+e^-$  collisions. The above angular distribution of scalar leptoquarks applies to both  $|F| = 2$  and  $F = 0$  type leptoquarks.

From this, one calculates the following integrated cross-section:

$$\begin{aligned} \sigma_{scalar} = & \frac{\pi\alpha^2\beta^3}{2s} \sum_{a=L,R} \left[ |\kappa_a(s)|^2 + \left(\frac{\lambda_a}{e}\right)^2 \text{Re}[\kappa_a(s)] F_1(\beta) \right. \\ & \left. + \left(\frac{\lambda_a}{e}\right)^4 F_2(\beta) \right]. \end{aligned} \quad (2.2.5.18)$$

where

$$F_1(\beta) = \frac{3}{2} \left( \frac{1+\beta^2}{\beta^2} - \frac{(1-\beta^2)^2}{2\beta^3} \ln \frac{1+\beta}{1-\beta} \right). \quad (2.2.5.19)$$

and

$$F_2(\beta) = 3 \left( -\frac{1}{\beta^2} + \frac{1+\beta^2}{2\beta^3} \ln \frac{1+\beta}{1-\beta} \right). \quad (2.2.5.20)$$

The first term in Equation 2.2.5.18 is the pure s-channel contribution, the second term is the interference between s- and t-channel, and the third term is the pure t-channel contribution.

The relative magnitudes of  $F_1(\beta)$  and  $F_2(\beta)$  can be compared. We will be studying electron-positron collisions with a centre-of-mass energy of 183 GeV. For pair-produced leptoquarks, the kinematic limit on  $M_\Phi$  is therefore 91.5 GeV/c<sup>2</sup>. If we set  $M_\Phi = 80$  GeV/c<sup>2</sup> and  $\sqrt{s} = 183$  GeV, then  $\beta = 0.485$ . With this value, we obtain  $F_1(\beta) = 3.80$ , and  $F_2(\beta) = 4.45$ .

## 2.5.2 Vector Leptoquarks

The differential cross-section of vector leptoquarks, which are the focus of this thesis, is given by [10]:

$$\begin{aligned} \frac{d\sigma_{vector}}{d(\cos \theta)} &= \frac{3\pi\alpha^2}{8M_\Phi^2}\beta \sum_{a=L,R} \left[ |\kappa_a(s)|^2 \tilde{F}_1(\theta, \beta) + \left(\frac{\lambda_a}{e}\right)^2 \text{Re}[\kappa_a(s)] \tilde{F}_2(\theta, \beta) \right. \\ &\quad \left. + \left(\frac{\lambda_a}{e}\right)^4 \tilde{F}_3(\theta, \beta) \right], \end{aligned} \quad (2.2.5.21)$$

where

$$\tilde{F}_1(\theta, \beta) = \beta^2 \left[ 1 + \frac{1}{4}(1 - 3\beta^2)\sin^2\theta \right], \quad (2.2.5.22)$$

$$\begin{aligned} \tilde{F}_2(\theta, \beta) &= 2 \left( 1 - \frac{1 - \beta^2}{t(\beta, \cos \theta)} \right) (1 - \beta^2) + 4\beta^2 \\ &\quad - \beta^2 \left( 1 - 2 \frac{1 - \beta^2}{t(\beta, \cos \theta)} \right) \sin^2\theta, \end{aligned} \quad (2.2.5.23)$$

and

$$\tilde{F}_3(\theta, \beta) = 4 + \frac{\beta^2}{4} \left[ (1 - \beta^2) \left( \frac{4}{t(\beta, \cos \theta)} \right)^2 + \frac{s}{M_\Phi^2} \right] \sin^2\theta. \quad (2.2.5.24)$$

Again, the above angular distribution of vector leptoquarks applies to both  $|F| = 2$  and  $F = 0$  type leptoquarks.

The integrated cross-section is

$$\begin{aligned} \sigma_{vector} &= \frac{\pi\alpha^2\beta}{2M_\Phi^2} \sum_{a=L,R} \left[ |\kappa_a(s)|^2 \tilde{F}_1(\beta) + \left(\frac{\lambda_a}{e}\right)^2 \text{Re}[\kappa_a(s)] \tilde{F}_2(\beta) \right. \\ &\quad \left. + \left(\frac{\lambda_a}{e}\right)^4 \tilde{F}_3(\beta) \right], \end{aligned} \quad (2.2.5.25)$$

where

$$\tilde{F}_1(\beta) = \beta^2 \frac{7 - 3\beta^2}{4}, \quad (2.2.5.26)$$

$$\tilde{F}_2(\beta) = \frac{15}{4} + 2\beta^2 - \frac{3}{4}\beta^4 - \frac{3}{8\beta}(1 - \beta^2)^2(5 - \beta^2)\ln\frac{1 + \beta}{1 - \beta}, \quad (2.2.5.27)$$

and

$$\tilde{F}_3(\beta) = 3(1 + \beta^2) + \frac{\beta^2}{4} \frac{s}{M_\Phi^2} + \frac{3}{2\beta}(1 - \beta^4)\ln\frac{1 + \beta}{1 - \beta}. \quad (2.2.5.28)$$

The relative magnitudes of  $\tilde{F}_1(\beta)$ ,  $\tilde{F}_2(\beta)$  and  $\tilde{F}_3(\beta)$  can be compared. If one chooses  $\sqrt{s} = 183$  GeV and  $M_\Phi = 80$  GeV/c<sup>2</sup>, then  $\beta = 0.485$ . With these values, we obtain  $\tilde{F}_1(\beta) = 0.371$ ,  $\tilde{F}_2(\beta) = 1.90$ , and  $\tilde{F}_3(\beta) = 7.11$ .

The first term in Equation 2.2.5.25 is the pure s-channel contribution to the cross-section, the second term is the interference between s- and t-channel, and the third term is the pure t-channel contribution. The pure s-channel term and the term representing the interference of the s- and t-channel both approach a finite value for large values of s. However, the pure t-channel contribution to the cross-section grows proportional to s, in the case of vector leptoquarks. This would violate unitarity. The Lagrangian is thus assumed to describe leptoquark interactions only if the energy is kept sufficiently low (hence the term *effective* Lagrangian). At higher energies, it is assumed that a more fundamental theory will supercede our Lagrangian, and unitarity will be preserved.

It is important to note that the s-channel contribution to the cross-section is independent of the couplings  $\lambda_{L,R}$ . The t-channel contribution is proportional to  $\lambda_{L,R}^4$ , and the interference term is proportional to  $\lambda_{L,R}^2$ . So for small values of  $\lambda_{L,R}$ , the s-channel term will dominate the pair-production cross-section of vector (and scalar) leptoquarks in  $e^+e^-$  collisions.

Figure 2.3 shows the production cross-section as a function of leptoquark mass for all nine vector leptoquarks, as calculated using Equation 2.2.5.25, for electron-positron annihilations at a centre-of-mass energy of 183 GeV. Only the

s-channel contributions are included, which is approximately correct for small values of the couplings  $\lambda_{L,R}$ . QED corrections are incorporated in the cross-section calculation, and are discussed briefly in Section 5.2.

### 2.5.3 Leptoquark Widths

The partial width for a single decay channel is given by

$$\Gamma_{scalar} = \frac{\lambda_{L,R}^2 M_\Phi}{16\pi} \quad (2.2.5.29)$$

for scalar leptoquarks, and

$$\Gamma_{vector} = \frac{\lambda_{L,R}^2 M_\Phi}{24\pi} \quad (2.2.5.30)$$

for vector leptoquarks, where  $\lambda_{L,R}$  denotes the leptoquark couplings to a particular final state as given in Table 2.1. The total width for a particular leptoquark is then obtained by summing over all possible final states.

### 2.5.4 Coupling Strengths and Branching Fractions

The generalized Yukawa couplings  $\lambda_{L,R}$  by construction are dimensionless, but their magnitude is unknown. In discussing the leptoquark coupling strengths, the magnitude of the electromagnetic coupling  $\lambda_{em}$  is often used as a reference:

$$\lambda_{em} = \sqrt{4\pi\alpha_{em}} = 0.3, \quad (2.2.5.31)$$

where  $\alpha_{em}$  is the fine structure constant:

$$\alpha_{em} = \frac{e^2}{\hbar c} \approx \frac{1}{137}, \quad (2.2.5.32)$$

where  $e$  is the charge of the electron in Gaussian units,  $\hbar$  is Planck's constant, and  $c$  is the speed of light.

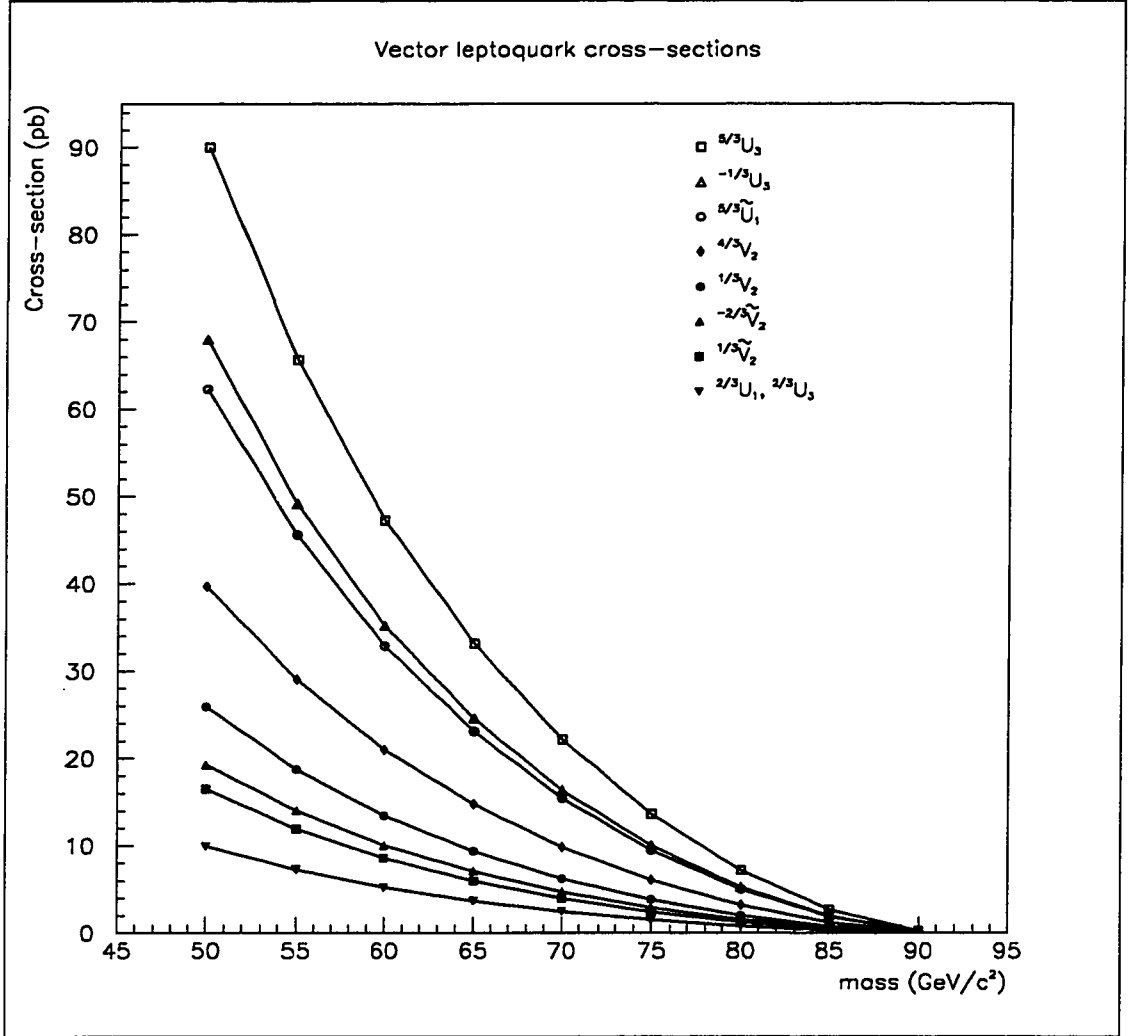


Figure 2.3: Production cross-section as a function of leptoquark mass for all nine vector leptoquarks, at a centre-of-mass energy of 183 GeV. The couplings  $\lambda_{L,R}$  are set to 0.001.

When searching for leptoquarks, experimental results often depend on  $\lambda_{L,R}$ . Typically, results are quoted for  $\lambda_{L,R} = \lambda_{em}$ ,  $\lambda_{L,R} < \lambda_{em}$  and/or  $\lambda_{L,R} \ll \lambda_{em}$ .

As mentioned previously, each leptoquark decays to a quark and a lepton. An important distinction is whether the lepton is a charged particle ( $l^\pm$ ), or a neutrino ( $\nu$ ). Decays to a quark and a charged lepton involve the unknown Yukawa couplings  $\lambda_{L,R}$ . However, because all neutrinos in the Standard Model are left-handed, decays to a quark-neutrino pair only involve the coupling  $\lambda_L$ .

The decay rates are proportional to  $\lambda_{L,R}^2$ . So for decays of a single leptoquark, defining  $\beta$  to be the branching fraction to a quark and a charged lepton (as opposed to a quark and a neutrino, which has corresponding branching fraction  $(1 - \beta)$ ), we have the following relations:

$$\beta = \frac{\lambda_L^2(l^\pm q) + \lambda_R^2(l^\pm q)}{\lambda_L^2(l^\pm q) + \lambda_R^2(l^\pm q) + \lambda_L^2(\nu q)} \quad (2.2.5.33)$$

and

$$1 - \beta = \frac{\lambda_L^2(\nu q)}{\lambda_L^2(l^\pm q) + \lambda_R^2(l^\pm q) + \lambda_L^2(\nu q)}. \quad (2.2.5.34)$$

So  $\beta$  is related to the relative magnitudes of  $\lambda_L^2$  and  $\lambda_R^2$ .

This discussion of coupling strengths and branching fractions is necessary because in the next section we discuss previous searches for leptoquarks, and many experiments have made specific assumptions about the magnitudes of  $\lambda_{L,R}$  or of  $\beta$ .

## 2.6 Previous Searches for Leptoquarks

Leptoquark masses and couplings are constrained by data from both high- and low-energy experiments. Direct searches for leptoquarks have been performed at LEP,

HERA and Fermilab. No experiment has ever seen clear evidence for leptoquarks. All previous searches for leptoquarks have focused on scalar leptoquarks.

Experiments searching for pair-produced leptoquarks have the advantage that the production cross-sections are independent of  $\lambda_{L,R}$  in s-channel. Hence, the limits obtained on the leptoquark mass are approximately independent of the couplings. Searches for singly produced leptoquarks always have to assume some values for  $\lambda_{L,R}$ .

In 1991, OPAL collaborators performed a search [12] for evidence of scalar leptoquarks in electron-positron collisions at LEP. At the time, LEP was operating at a centre-of-mass energy equivalent to the mass of the  $Z^0$  boson (about 91 GeV). Thus, the search was for leptoquarks that had been pair-produced in the decay of a  $Z^0$ . With a data sample of  $6.3 \text{ pb}^{-1}$ , no evidence of scalar leptoquarks was found. An upper limit of 1.7 pb on the production cross-section of leptoquarks was obtained at the 95% confidence level, assuming a branching ratio of 50% for the decay of a leptoquark into the channels with a charged lepton. Lower limits on the leptoquark mass of between  $41.4 \text{ GeV}/c^2$  and  $46.4 \text{ GeV}/c^2$  were obtained at the 95% confidence level, depending on the values assigned to the leptoquark couplings.

The other three LEP experiments also performed searches for pair-produced leptoquarks between 1991 and 1992 (ALEPH [13], DELPHI [14], L3 [15]). None of these searches found evidence of leptoquarks, and the limits obtained were similar to the results of the OPAL search. The overall LEP result excludes all types of scalar leptoquarks with masses below about  $45 \text{ GeV}/c^2$ , at the 95% confidence level.

Recently, the OPAL collaboration searched for pair-produced leptoquarks at centre-of-mass energies of 161 GeV and 172 GeV [16]. The data from the two energies were combined. The search was for scalar leptoquarks of the first or second

generation, which decay to a quark-neutrino pair with a large branching fraction. Two species of scalar leptoquarks ( $-^{2/3}\vec{S}_3$  and  $-^{1/3}\tilde{R}_2$ ) decay to quark-neutrino 100% of the time (thus  $\beta = 0$ ). One species of scalar leptoquark ( $^{2/3}R_2$ ) can decay to quark-neutrino at least 50% of the time (thus  $\beta < 0.5$ ), depending on the couplings  $\lambda_{L,R}$ . For the two scalar leptoquarks which decay to quark-neutrino 100% of the time, the search placed upper limits on the leptoquark mass of 73.4 GeV/c<sup>2</sup> for  $-^{2/3}\vec{S}_3$ , and 53.0 GeV/c<sup>2</sup> for  $-^{1/3}\tilde{R}_2$ , at the 95% confidence level. For the scalar leptoquark  $^{2/3}R_2$ , which does not have a fixed value of  $\beta$ , regions in the  $\beta$ - $M_{LQ}$  plane were excluded, with  $\beta$  ranging from 0 to 0.5. For first-generation decays of  $^{2/3}R_2$ , the excluded region is  $M_{LQ} < 69$  GeV/c<sup>2</sup>, and for second-generation decays, the excluded region is  $M_{LQ} < 72$  GeV/c<sup>2</sup>, at the 95% confidence level.

The OPAL collaboration also searched for single leptoquark production in electron-photon scattering at centre-of-mass energies of 161 GeV and 172 GeV [17]. The assumption is that a single leptoquark may be produced in the process  $e + q \rightarrow LQ$ , where the initial state quark originates from a hadronic fluctuation of a quasi-real photon which has been radiated by one of the LEP beams. The results are the most stringent LEP limits, however, they are  $\lambda_{L,R}$ -dependent. The search was for first-generation scalar leptoquarks, with  $\beta = 0.5$  or  $\beta = 1.0$ . In both cases, leptoquark masses below 131 GeV/c<sup>2</sup> are excluded, for  $\lambda_{L,R} \geq \lambda_{em} = 0.3$ . However, for  $\lambda_{L,R} = 0.1$ , the mass limit is only about 60 GeV/c<sup>2</sup>, and for  $\lambda_{L,R} < 0.1$ , the LEP limit from searches for pair-produced leptoquarks is more stringent.

The CDF [18] and D0 [19] experiments at Fermilab searched for first-, second- and third-generation leptoquarks between 1993 and 1995, using the Tevatron proton-anti-proton collider. Provided that the leptoquarks decay to two jets and two charged leptons 100% of the time (i.e.  $\beta = 1.0$ ), the D0 experiment put a lower limit on the mass of first-generation scalar leptoquarks of 133 GeV/c<sup>2</sup>, and the CDF

experiment excluded second-generation scalar leptoquarks below  $131 \text{ GeV}/c^2$ . Due to very large background contributions, the channels where one or both leptoquarks decay to a quark and a neutrino were not searched for directly. The two experiments placed limits on  $\sigma_{prod}\beta^2$  and  $2\sigma_{prod}\beta(1-\beta)$ , where  $\beta$  is the decay branching ratio to quark and charged lepton, and  $\sigma_{prod}$  is the production cross-section.

Recently, the limits determined for scalar leptoquarks by CDF [20] and D0 [21] were improved. Assuming  $\beta = 1.0$ , first-generation leptoquarks were excluded for masses below  $225 \text{ GeV}/c^2$  by D0, and  $213 \text{ GeV}/c^2$  by CDF, at the 95% confidence level. For  $\beta < 1.0$ , the limits are weaker: around  $176 \text{ GeV}/c^2$  for  $\beta = 0.5$ . For second-generation scalar leptoquarks, CDF and D0 exclude masses below  $184 \text{ GeV}/c^2$ , and for third-generation scalar leptoquarks, the limit is  $98 \text{ GeV}/c^2$  (both results are at the 95% confidence level, and assume that  $\beta = 1.0$ ).

The most recent results from D0 [22] exclude first-generation scalar leptoquarks with mass below  $225 \text{ GeV}/c^2$  for  $\beta = 1.0$ ,  $204 \text{ GeV}/c^2$  for  $\beta = 0.5$ , and  $79 \text{ GeV}/c^2$  for  $\beta = 0.0$ , at the 95% confidence level. The limits are again less stringent for second- and third-generation leptoquarks.

It is apparent that the Fermilab results are sensitive to the branching fraction  $\beta$ , and for small  $\beta$ , the limits are the least stringent.

The ZEUS [23] and H1 [24] experiments searched for first-generation leptoquarks between 1993 and 1996. These two detectors are located on the HERA electron-proton collider at DESY. The mass limits obtained by the HERA experiments depend on the Yukawa couplings  $\lambda_{L,R}$ . Assuming that  $\lambda_{L,R} = \lambda_{em}$  (the electromagnetic coupling strength  $\lambda_{em} = 0.3$ ), the HERA experiments set lower limits on the leptoquark mass at the 95% confidence level. The ZEUS limits ranged from  $207$  to  $272 \text{ GeV}/c^2$ , depending on the type of leptoquark. However, the limits

<i>Experiment</i>	<i>Year</i>	<i>Type of Leptoquark</i>	<i>Lower Limit on Mass (GeV/c<sup>2</sup>)</i>	<i>Assumptions</i>
OPAL	1997	Scalar	53 - 73	none
D0	1997	Scalar	225	$\beta = 1.0$
			204	$\beta = 0.5$
			79	$\beta = 0.0$
CDF	1997	Scalar	213	$\beta = 1.0$
ZEUS	1996	Scalar & Vector	207 - 272	$\lambda_{L,R} = 0.3, \beta = 1.0$
			< 100	$\lambda_{L,R} = 0.01, \beta = 1.0$
H1	1995	Scalar & Vector	216 - 275	$\lambda_{L,R} > 0.3$

Table 2.2: A summary of the most recent leptoquark mass lower limits obtained by various experiments, including the assumptions that were made. The mass limits are all at the 95% confidence level.

are less stringent for  $\lambda_{L,R} < \lambda_{em}$ . Typically, for  $\lambda_{L,R} = 0.1$ , these limits are lowered by about 50 GeV/c<sup>2</sup>. And for  $\lambda_{L,R} < 0.01$ , most of the limits are in the range 50 to 100 GeV/c<sup>2</sup>. The results were obtained under the assumption that the leptoquark states are degenerate in mass.

The LEP and Fermilab experiments have the advantage that the production cross-sections are independent of  $\lambda_{L,R}$ , when  $\lambda_{L,R} \ll \lambda_{em}$ . However, the Fermilab results are sensitive to the branching fraction  $\beta$ , and for small  $\beta$ , the limits are the least stringent. Of all these searches, for low values of  $\beta$  and/or small values of  $\lambda_{L,R}$ , the best limit is the one given by the direct searches at LEP. Further, all of the stated results above have focused on scalar leptoquarks; vector leptoquarks have been given little consideration.

Table 2.2 shows the most recent lower limits for the leptoquark mass obtained by various experiments.

## 2.7 Leptoquarks at LEP

At LEP, leptoquarks could be pair-produced via s-channel  $\gamma$  and  $Z^0$  exchange, and in the case of first-generation leptoquarks carrying the electron number, also via t-channel exchange of a  $u$  or  $d$  quark. The t-channel process involves the unknown Yukawa couplings  $\lambda_{L,R}$ . The production cross-section depends on the quantum numbers of the leptoquark and on the leptoquark mass. It can vary from a few hundredths of a picobarn, to over 10 picobarns.

Furthermore, leptoquarks in the LEP mass range are relatively narrow states. The partial width for a single decay channel is expected to be much less than  $100 \text{ MeV}/c^2$ , for  $\lambda_{L,R} < \lambda_{em}$ .

The lifetime of a particle is inversely proportional to its width. Equations 2.2.5.29 and 2.2.5.30 show that the width of a leptoquark is proportional to the mass, and to the square of the couplings. So a leptoquark with a large mass will have a short lifetime. For a mass width of  $100 \text{ MeV}/c^2$ , the lifetime is  $6.6 \times 10^{-24}$  seconds. This corresponds to a decay length of approximately 2 fm.

However, leptoquarks carry colour, and so they will fragment into hadrons within about 1 fm of the leptoquark pair-production vertex at LEP, as is the case for any quark. Thus, it is not possible to detect leptoquarks directly; one must search for the decay products.

We only search for first- and second-generation leptoquarks. Third-generation leptoquarks would decay to either a top ( $t$ ) or bottom ( $b$ ) quark, and a tau lepton ( $\tau$ ) or tau neutrino ( $\nu_\tau$ ). Top quarks are too massive to be produced in the decay of a pair-produced leptoquark at LEP, and bottom quarks are challenging to identify and would require a substantially different search methodology.

For large masses and small couplings, the formation of leptoquark bound states is possible, either with another leptoquark (forming leptoquarkonium,  $LQ\text{-}\overline{LQ}$ ) or with a quark (forming a leptomeson,  $LQ\text{-}\bar{q}$ ). If such objects exist, it should be possible to observe them at future colliders [25].

## CHAPTER 3

### The LEP Collider

The Large Electron Positron (LEP) collider is located at the European Laboratory for Particle Physics (CERN<sup>1</sup>), near Geneva, Switzerland. LEP accelerates electrons and positrons in a circular underground tunnel, and collides them at centre-of-mass energies of up to 189 GeV (achieved in 1998). In 1997, LEP operated primarily at 183 GeV.

LEP began operation in 1989, colliding electrons and positrons at centre-of-mass energies of about 91 GeV (45.5 GeV per beam), in order to produce  $Z^0$  bosons. Operation at this energy was continued until 1995, when the centre-of-mass energy was increased to about 140 GeV. Further upgrades have resulted in collisions at centre-of-mass energies of 161 GeV, 172 GeV, 183 GeV and 189 GeV. The maximum LEP luminosity (number of particles per unit area per unit time) that was achieved in 1997 is  $3.9 \times 10^{31} \text{ cm}^{-2}\text{s}^{-1}$ .

The LEP collider itself is actually the last step in a series of particle accelerators at CERN. Electrons are initially accelerated to 200 MeV by the LEP Injector Linac (LIL). These electrons may be directed onto a target, to produce positrons. The electrons (or positrons) are then accelerated to 600 MeV, before entering the Electron Positron Accumulator (EPA), where they are stored until eight compressed bunches have been accumulated. The beam is then injected into the Proton Synchrotron (PS), where the energy is increased to 3.5 GeV. Next, the beam energy is

---

<sup>1</sup>The French name for the facility is “Conseil Européen pour la Recherche Nucléaire”.

increased to 20 GeV by the Super Proton Synchrotron (SPS). Finally, the beam enters the LEP collider, where the beam energy is increased to 91.5 GeV for collisions with centre-of-mass energies of 183 GeV, for example. The only difference in this process between electron beams and positron beams is that LEP accelerates the two beams in opposite directions.

The electron and positron beams are made to collide at four interaction points around LEP. Large, general-purpose detectors (OPAL, ALEPH, DELPHI, L3) exist at each of these interaction points. Figure 3.1 shows the location of the four experiments along the LEP collider ring.

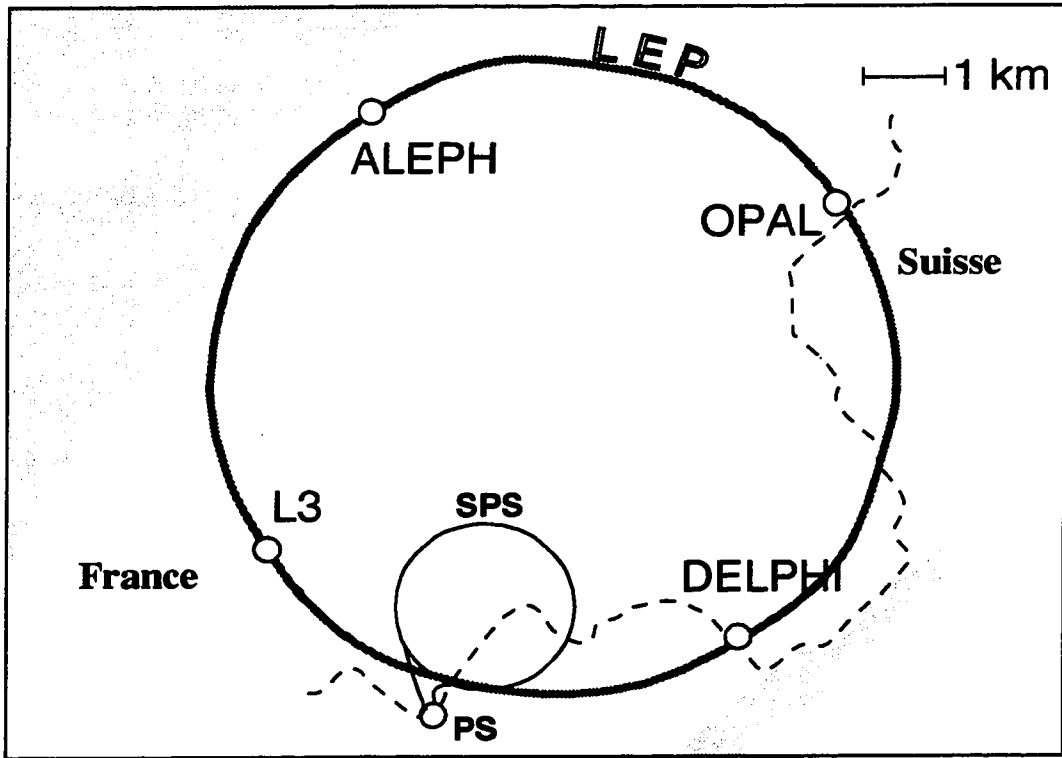


Figure 3.1: The LEP collider at CERN, showing the location of the four  $e^+e^-$  interaction points. Also shown are the PS and SPS accelerators.

## CHAPTER 4

### The OPAL Detector

The Omni-Purpose Apparatus for LEP (OPAL) [26] is a large detector located at one of LEP's four interaction points. It has been operating since LEP first collided electrons and positrons in 1989. The OPAL detector was designed to study a wide range of physics issues. Increased LEP energies have recently provided a new energy region for OPAL to explore. A cutaway view of the OPAL detector is shown in Figure 4.1.

The coordinate system used by OPAL is defined such that the  $z$  axis lies along the beam pipe in the direction of the electron beam; the  $y$  axis points vertically upwards; and the  $x$  axis points to the centre of the LEP ring. The polar angle  $\theta$  is the angle from the  $z$  axis, and the azimuthal angle  $\phi$  is the angle from the  $x$  axis. By convention, the  $x$ - $y$  plane is usually referred to as the  $r$ - $\phi$  plane.

The OPAL collaboration currently consists of over 300 physicists and technicians, from over 30 institutions. The numerous development, construction, maintenance and operation tasks are divided among the participating institutions.

#### 4.1 Overview

The OPAL detector was intended to be a reliable, general-purpose detector, which would study the interactions which occur in electron-positron collisions. The major

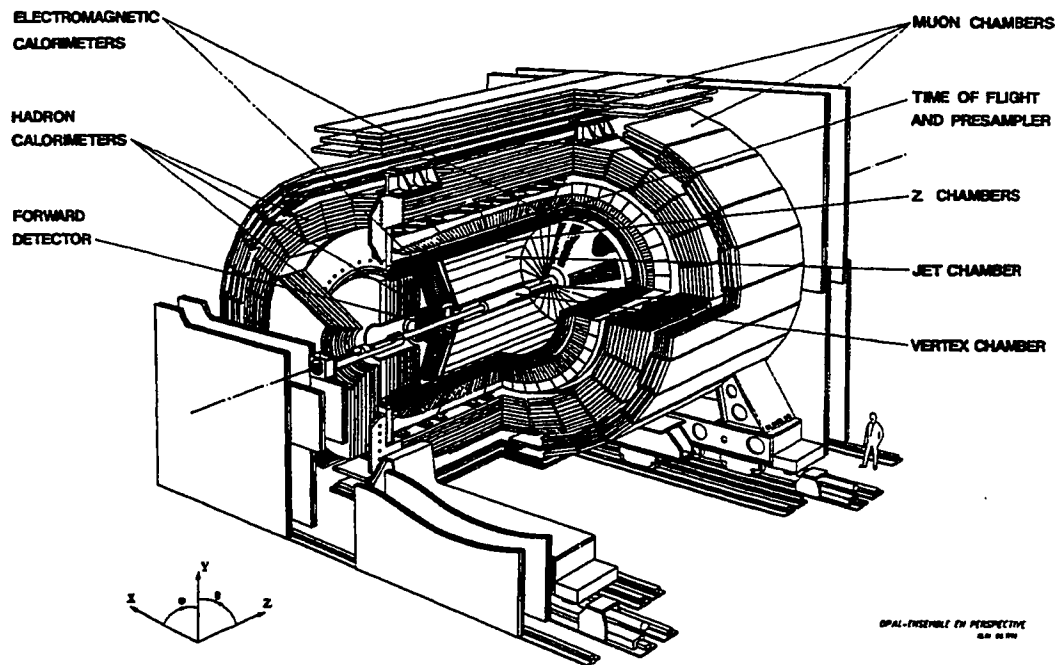


Figure 4.1: A cutaway view of the OPAL detector.

design goals of the detector include:

- charged particle tracking near the interaction point, including the reconstruction of primary and secondary vertices.
- accurate identification of electrons, positrons and photons, including measurement of their energies,
- good measurement of hadronic energy,
- good identification of muons.

These goals were achieved through the combined use of several different systems. The central tracking system measures the momentum of charged particles near the interaction point, and determines their direction. The electromagnetic calorimetry identifies and measures the energy of electrons, positrons and photons. The hadronic calorimetry measures the energy of hadronic showers. The muon system identifies muons.

Several upgrades have been performed on the OPAL detector during its existence, in the form of new subdetectors, including:

- the Silicon Microvertex Detector [27], added in 1991, which provides precise vertex position measurements near the interaction point,
- the Time-of-Flight Endcap (TE) Detector [28], added in 1996, which extends the coverage of the time-of-flight system, thus improving overall triggering.

The OPAL detector can be divided into six subdetector regions, both geometrically and according to task: the Central Detector, the Electromagnetic Calorimeter, the Hadron Calorimeter, the Muon Detector, the Forward Detector, and

the Silicon Tungsten Detector. Also of importance is the readout system, consisting of the trigger and the online data acquisition system.

## **4.2 The Magnet and Beam Pipe**

The OPAL magnet consists of a solenoidal coil and a return yoke. The solenoidal coil must be “transparent” to particles originating from the interaction region. A self-supporting water-cooled solenoid is used, composed of a hollow aluminum conductor, held together with glass-epoxy. The solenoidal coil is situated at a mean radius of 2.18 meters from the beamline, between the central detector and the calorimetry. The return yoke is composed of iron, and consists of five pieces which may be moved apart to allow access to the apparatus located within it. The magnet system provides a magnetic field of 0.435 Tesla in the central detector region, accurate to within  $\pm 0.5\%$ .

The beam pipe consists of a 0.11 mm thick beryllium tube. The radius of the pipe is 53.5 mm. There is a tube consisting of layers of carbon fibre, 2.0 mm thick in total, at a distance of 80 mm from the beam. The carbon fibre tube supports the 4 bar absolute pressure of the gas of the central tracking system. The gap between the beam pipe and the carbon fibre tube is filled by the silicon microvertex detector.

## **4.3 The Central Detector**

The Central Detector consists of four components. A Silicon Microvertex Detector is situated closest to the beampipe and interaction point, followed by three drift chamber devices: the Vertex Chamber, the Jet Chamber and the Z-Chambers. The

drift chambers are situated within a pressure vessel which maintains a pressure of 4 bar. The gas mixture used by the drift chambers is argon (88.2%), methane (9.8%) and isobutane (2.0%). A solenoid surrounds the central detector, providing a magnetic field of 0.435 Tesla.

#### **4.3.1 Silicon Microvertex Detector**

The Silicon Microvertex Detector [27], added in 1991, consists of two barrel-shaped layers of Silicon Microstrip Detectors. These two layers are at radii of 6 cm and 7.5 cm from the beam axis.

Located directly around the electron-positron interaction point, the Silicon Microvertex Detector makes precise position measurements and thus can track particles back to their point of origin, called a vertex. Vertex finding is very useful for identifying particles with long decay lengths.

The Silicon Microvertex Detector was replaced in 1993 by a two coordinate readout Silicon Microvertex Detector [29], which is capable of readout in both the  $z$  and  $\phi$  directions. A cutaway view of the Silicon Microvertex Detector is shown in Figure 4.2.

#### **4.3.2 Vertex Chamber**

The OPAL Vertex Chamber [30], shown in Figure 4.3, is a cylindrical drift chamber, which surrounds the Silicon Microvertex Detector. It is 1 meter in length, and has inner and outer radii of 88 mm and 235 mm respectively. It consists of two layers of drift chambers. The inner layer contains axial wires, which are strung parallel to the beam direction. The outer layer contains stereo wires, which are inclined

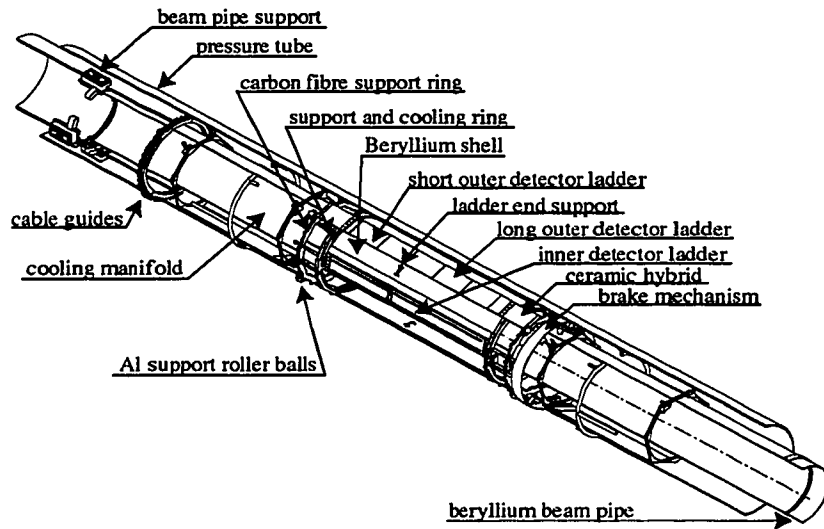


Figure 4.2: A cutaway view of the OPAL Silicon Microvertex Detector.

at an angle of  $4^\circ$  to the beam direction. The anode planes consist of alternating  $200\ \mu\text{m}$  diameter gold plated copper-beryllium potential wires and  $20\ \mu\text{m}$  diameter gold plated tungsten-rhodium anode wires.

The Vertex Chamber's main task is to determine the position of secondary vertices, due to long-lived particles. It also contributes to the overall momentum resolution of the central detector system.

The  $r$ - $\phi$  position can be precisely measured using the drift time on to the axial sense wires. A fast  $z$  coordinate measurement may be made by using the time difference between signals at either end of the axial sense wires. A more precise  $z$  coordinate measurement may be obtained by combining axial and stereo drift time information offline.

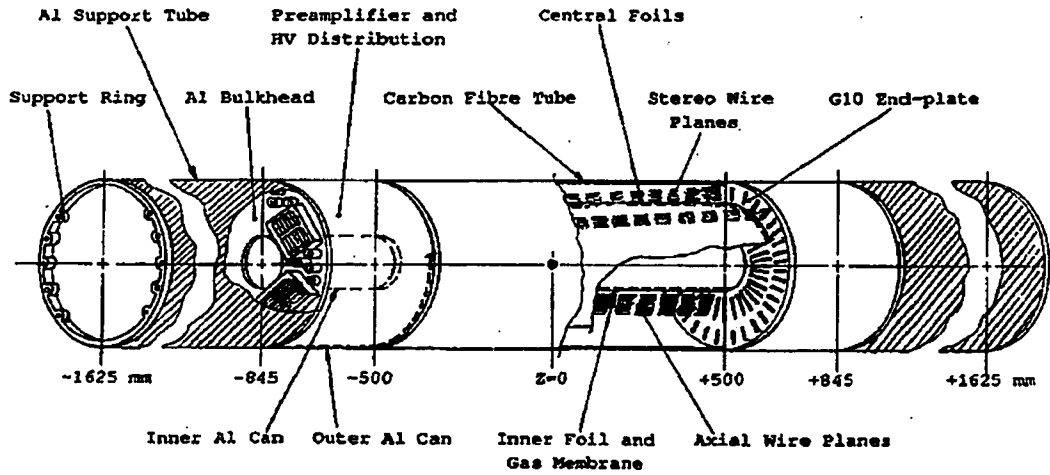


Figure 4.3: The OPAL Vertex Chamber.

### 4.3.3 Jet Chamber

The OPAL Jet Chamber [31] is a cylindrical drift chamber, which surrounds the vertex chamber. It is 4 meters in length, and has inner and outer radii of 0.25 meters and 1.85 meters respectively. The Jet Chamber provides tracking and particle identification.

The Jet Chamber is subdivided into 24 identical sectors, each containing a plane of 159 anode wires, strung parallel to the beam direction. The radial spacing of the anode wires is 10 mm.

Position measurements in the  $r$ - $\phi$  plane are made directly from the drift time. The  $z$  coordinate is determined using a charge division method. The integrated charge collected at each end of a wire, along with the track momentum, allow the energy loss,  $dE/dx$ , to be calculated [32]. The  $dE/dx$  value is used for particle identification.

#### 4.3.4 Z-Chambers

The OPAL Z-Chambers [33] are a layer of 24 drift chambers, in the form of a 4 meter long cylinder, with the axis being the beam pipe. The diameter of the cylinder is 3.85 meters. The purpose of the Z-Chambers is to measure the  $z$  coordinate of tracks when they leave the Jet Chamber.

Each chamber is subdivided into 8 cells, each of which has six  $20\ \mu\text{m}$  diameter gold plated tungsten anode wires in the  $\phi$  direction, spaced 4 mm apart at increasing radii. The drift field within the Z-Chambers is 800 V/cm, which gives a spatial resolution of about  $150\ \mu\text{m}$  in the  $z$  direction. An  $r$ - $\phi$  spatial resolution of 1.5 cm is obtained using a charge division (also called current division) technique, which requires amplifiers at both ends of the anode wires.

### 4.4 Electromagnetic Calorimeter

The purpose of the Electromagnetic Calorimeter [26] is to detect and identify electrons, positrons and photons. It is a lead glass calorimeter, and consists of a barrel region and two endcap regions. It operates under the principle that a relativistic charged particle traversing the lead glass blocks will emit Čerenkov photons. The Electromagnetic Calorimeter combined with two forward lead scintillator calorimeters provides an acceptance of almost 99% of the solid angle.

There are about 2 radiation lengths of material in front of the calorimeter, so most electromagnetic showers begin before the particle has reached the lead glass. Therefore, in both the barrel and endcap regions, presampling devices are placed in front of the lead glass, to measure the energy and position of showers. In front of the presamplers in both the barrel and endcap regions are Time-of-Flight Detectors.

#### **4.4.1 Time-of-Flight Systems**

In the barrel region, the Time-of-Flight system [26] consists of 160 scintillation counters, forming a cylindrical layer at a radius of 236 cm from the beam axis. In the endcap region, the Endcap Time-of-Flight system [28], added in 1996, consists of 10 mm thick scintillator tiles, located between the Endcap Presampler and the Endcap Electromagnetic Calorimeter. The Endcap Time-of-Flight scheme utilizes wavelength-shifting fibres embedded within the scintillation material. The Barrel Time-of-Flight system provides fast triggering, rejection against cosmic rays, and contributes to charged particle identification in the range 0.6 GeV to 2.5 GeV. The Endcap Time-of-Flight system provides triggering in the forward region, is used for cosmic ray rejection, and gives an accurate measurement of the time of collision of the LEP beams.

#### **4.4.2 Barrel Electromagnetic Presampler**

Located between the Barrel Time-of-Flight counters and the Barrel Electromagnetic Calorimeter, the Barrel Electromagnetic Presampler [34] consists of 16 chambers in the shape of a cylinder at a radius of 239 cm. Each chamber contains two layers of drift tubes. The anode wires run parallel to the beam direction, while each layer of drift tubes also contains 1 cm wide cathode strips, at an angle of  $45^\circ$  to the anode wires. By combining a measurement of the charge collected at each of the wires with a reading of the strips, one can determine the spatial position of incoming particles. The barrel electromagnetic presampler can be used to correct the calorimeter shower energy, because the hit multiplicity is roughly proportional to the energy deposited prior to the presampler.

### 4.4.3 Barrel Lead Glass Calorimeter

The Barrel Lead Glass Calorimeter is made up of 9440 lead glass blocks, arranged in a cylindrical array at a radius of 246 cm from the beam axis. Each block has a 10 cm  $\times$  10 cm face, and a depth of 37 cm, which corresponds to 24.6 radiation lengths. The blocks are angled so that they each point towards the interaction point. As relativistic charged particles pass through the lead glass, they emit Čerenkov light, which is detected by 3 inch diameter phototubes at the base of each lead glass block.

### 4.4.4 Endcap Electromagnetic Presampler

Located between the Endcap Time-of-Flight system and the Endcap Electromagnetic Calorimeter, the Endcap Electromagnetic Presampler is a multiwire proportional counter. There are 32 chambers which extend from polar angles of about  $|\cos \theta| = 0.83$  to  $|\cos \theta| = 0.95$ .

### 4.4.5 Endcap Electromagnetic Calorimeter

Similar to the Barrel Electromagnetic Calorimeter, the Endcap Electromagnetic Calorimeter consists of lead glass blocks. Each endcap utilizes 1132 blocks in a dome-shaped array. The Endcap Electromagnetic Calorimeter provides coverage from about  $|\cos \theta| = 0.81$  to  $|\cos \theta| = 0.98$ . Each lead glass block has a 10 cm  $\times$  10 cm face, and a length of either 38 cm, 42 cm or 52 cm, depending on its location. Typically 22 radiation lengths of material are provided by the blocks. Each block is oriented parallel to the beam axis. The emitted Čerenkov light is collected by Vacuum Photo-Triodes, which are single-stage photomultipliers.

## 4.5 Hadron Calorimeter

The purpose of the Hadron Calorimeter [26] is to measure hadronic energy. The Hadron Calorimeter consists of a barrel region and two endcap regions. Both the barrel and endcap regions use wire chambers, and together cover 97% of the solid angle. There are at least four interaction lengths of iron present, so only muons should emerge from the Hadron Calorimeter. The hadronic energy is in fact determined by combining information from both the Electromagnetic Calorimeter and the Hadron Calorimeter, because there are already 2.2 interaction lengths in front of the Hadron Calorimeter.

The Hadron Calorimeter makes use of alternating layers of iron absorbers and wire chambers. Due to the high density of iron, most of the incident particles' energy will be deposited in the iron plates. The iron is necessary to prevent any of the energy from escaping from the calorimeter and hence avoiding detection and measurement.

### 4.5.1 Barrel and Endcap Hadron Calorimeters

The Barrel Hadron Calorimeter has 9 layers of wire chambers, separated by 8 regions of 10 cm thick iron slabs as an absorber. The Endcap Hadron Calorimeter consists of 8 layers of wire chambers around 7 layers of 10 cm thick iron slabs.

The wire chambers are planes of streamer tubes in a gas mixture of isobutane (75%) and argon (25%). The streamer tubes run parallel to the beam axis, with a distance of 1 cm between the anode wires of neighbouring tubes. The collected charge is read out from cathode pads which are located on the sides of the streamer tubes. Also read out are 4 mm wide aluminum strips which run the length of the

chamber. In the barrel region, the aluminum strips are parallel to the beam axis, however in the endcap region, the strips are arranged in a plane perpendicular to the beam axis.

The cathode pads and aluminum strips provide the chamber signals. The signals from the anode wires are only used for monitoring.

#### **4.5.2 Pole-Tip Hadron Calorimeter**

The Pole-Tip Hadron Calorimeter [35] extends the coverage of the Hadron Calorimeter from  $|\cos \theta| = 0.91$  down to  $|\cos \theta| = 0.99$ . Each pole tip consists of ten 0.7 cm thick multiwire proportional chambers, separated by nine 8 cm thick iron slabs. The chambers contain a gas mixture of  $\text{CO}_2$  (55%) and n-pentane (45%), with a distance of 2 cm between anode wires. The same charge collection scheme of cathode pads and aluminum strips is utilized.

### **4.6 Muon Detector**

The goal of the Muon Detector [26] is to separate muons from the hadronic background. Particles which reach the Muon Detector have already traveled through the equivalent of 1.3 meters of iron, so the likelihood of a pion not interacting is less than 0.1%. The Muon Detector consists of a barrel region and two endcap regions, which together cover over 93% of the solid angle.

### 4.6.1 Barrel Muon Detector

The barrel region consists of four layers of drift chambers which form a cylinder at a radius of 5 cm. Each chamber has a cross-sectional area of  $120\text{ cm} \times 9\text{ cm}$ . The chambers vary in length between 10.4 meters and 6 meters, so that they can fit between the magnet support legs. There are 110 chambers in total. Each chamber consists of two drift cells, each with one anode wire running parallel to the beamline. Parallel to the anode wires run diamond-shaped cathode pads [36]. Four signals are read from the cathode pads of each cell, and two additional signals are read from the ends of each anode wire. The drift chambers operate with a gas mixture of argon (90%) and ethane (10%).

The drift time in the chambers provides a coordinate in the  $r$ - $\phi$  plane. A rough measurement of the  $z$  coordinate is obtained using the difference in time and pulse height of the signals arriving at both ends of an anode wire. A more accurate measurement of the  $z$  position is determined from the cathode pads.

### 4.6.2 Endcap Muon Detector

Each Endcap Muon Detector uses two layers of drift chambers, providing coverage from  $|\cos \theta| = 0.67$  down to  $|\cos \theta| = 0.985$ . Each chamber contains two layers of streamer tubes, oriented perpendicular to the beamline. One layer of the streamer tubes has its anode wires vertical, the other layer has its anode wires horizontal. The streamer tubes are read out using 0.8 cm wide aluminum strips, which run parallel to the anode wires on one side of the tubes, and perpendicular to the wires on the other side. The gas mixture used is argon (25%) and isobutane (75%).

## 4.7 Forward Detector

The Forward Detector [37] contains several devices, whose purpose is to detect low angle Bhabba scattering events. An accurate measurement of the Bhabba scattering rate is used to determine the total integrated luminosity delivered to OPAL by LEP.

The Forward Detector can detect particles which originate at the interaction point and travel at an angle between 47 mrad and 120 mrad to the beam axis. The Forward Detector consists of a calorimeter, tube chambers, drift chambers, a Gamma Catcher, and a Far Forward Monitor. A cross-sectional view of the Forward Detector region is shown in Figure 4.4.

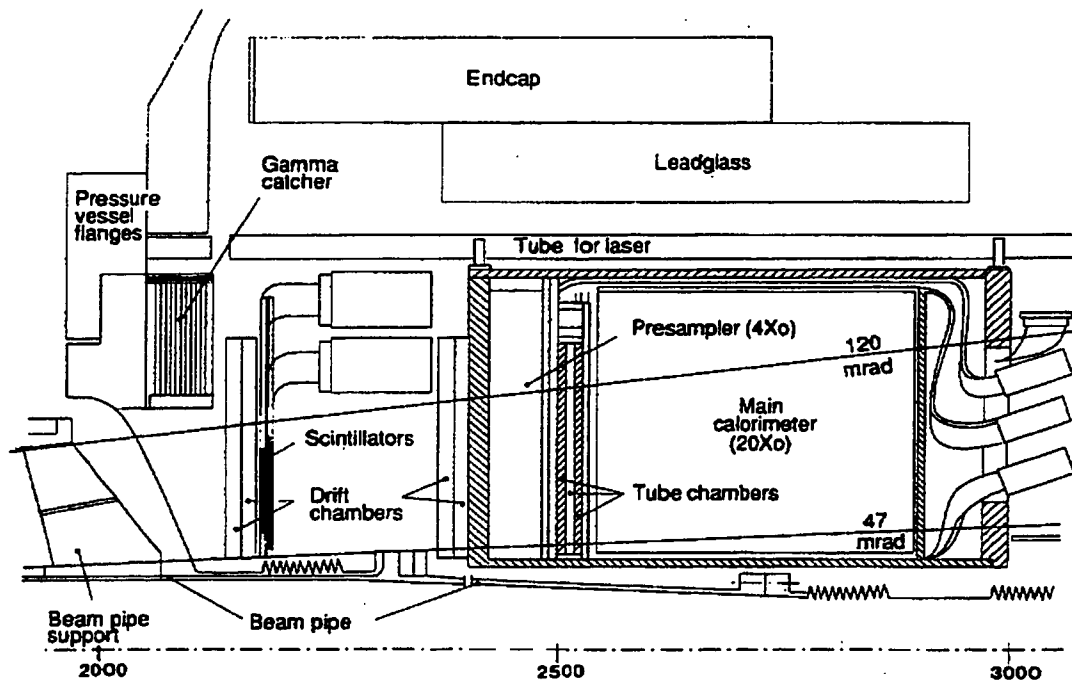


Figure 4.4: Cross-sectional view of the OPAL Forward Detector region.

The Forward Calorimeter consists of 35 layers of plastic scintillator, separated by lead as an absorber. There are 24 radiation lengths of material present, divided into a presampler and a main calorimeter. There are three layers of proportional tube chambers situated between the presampler and main sections of the Forward Calorimeter. There are two layers of drift chambers in front of the Presampler Calorimeter, which give a position measurement using a charge division technique. The Gamma Catcher is in the form of a ring of alternating layers of lead and scintillator, providing 7 radiation lengths of material. It is located in the gap between the Electromagnetic Endcap and the Forward Calorimeter. The Far Forward Monitor consists of lead-scintillator calorimeter modules, providing 20 radiation lengths of material. They are located 7.85 meters from the interaction point, on each side. Their purpose is to identify electrons which have been scattered at angles between 5 mrad and 10 mrad, but which are deflected outwards due to the LEP quadrupole magnets.

## 4.8 Silicon Tungsten Detector

The Silicon Tungsten Detector [38] was added to OPAL in 1994 to improve the luminosity measurement. It is a sampling calorimeter used to detect low angle Bhabha scattering events. It consists of two calorimeters located 2.39 meters from the interaction point on each side. It accepts particles which originate at the interaction point and travel at an angle between 25 mrad and 59 mrad to the beam axis. Each calorimeter has 19 layers of silicon detectors, spaced by 18 layers of tungsten. There is a layer of silicon at the front to detect preshowering. The first 14 layers of tungsten are 3.8 mm thick, providing 1 radiation length each, while the final 4 layers of tungsten are 7.6 mm thick, providing 2 radiation lengths each.

## 4.9 The Trigger

Only those events which pass certain trigger conditions [39] are actually read out of the OPAL detector. This reduces the total amount of data recorded.

There are two types of signals which are used for triggering: “stand-alone” signals such as multiplicity counts and energy sums, and lower threshold signals formed from a trigger matrix of  $6 \times 24$  binning in  $\theta$  and  $\phi$  respectively. The trigger matrix takes signals from the central tracks, the Time-of-Flight counters, the Electromagnetic Calorimeter, and the Muon Detector. The trigger processor forms correlations in space between subdetectors in  $\theta$  and  $\phi$  together with the stand-alone signals, to make a decision.

There is a pretrigger used by OPAL, which also includes the bunch crossing signal from LEP. The pretrigger gives a fast reading of the probability of a good  $e^+e^-$  collision. Energy sums form the stand-alone signals, and the pretrigger matrix consists of 12 bins in  $\phi$ . The pretrigger processor uses multiplicity counting to make a decision, and may form correlations in  $\theta$  and  $\phi$  between subdetectors, together with the stand-alone signals.

Overall, the trigger reduces the event rate to around 10 Hz.

## 4.10 Online Data Acquisition System

When the trigger selects an event as being a potentially interesting event, all of the OPAL subdetectors are read out. Each subdetector is read out separately by its own frontend electronics into its Local System Crate(s) (LSC). The subevent structures from the various LSCs are then assembled in the Event Builder (EVB). The EVB is

connected to the LSCs via high-speed memory-map links, and is situated in a single VME crate.

After the complete events have been assembled by the EVB, they are sent to a filter which checks the events and compresses them for storage on disk. Events which are clearly bad (typically 15% to 20% of all triggers) are rejected. Every event which reaches the filter has its event header recorded, even if the event is rejected.

Events which pass the filter are recorded as 20 MB data files called partitions. These files are then copied from the filter disk to a reconstruction farm of Unix workstations, which determine various event parameters. Finally, the reconstructed events are recorded and stored for future offline analysis.

## CHAPTER 5

### Leptoquark Simulation and Search

This chapter presents the various steps that were taken in the search for vector leptoquarks.

If leptoquarks exist with masses below  $91.5 \text{ GeV}/c^2$ , it should be possible to pair-produce them in electron-positron collisions at a centre-of-mass energy of 183 GeV. However, the leptoquarks would decay quickly. Therefore, rather than detecting the leptoquarks, the goal is to detect the decay products of leptoquarks: the leptons and the quarks. In the OPAL detector, quarks are detected as jets of particles, leptons are identified as charged tracks, and neutrinos are not directly detected, but are inferred with the observation of missing energy.

Since each leptoquark can decay to either a quark and a charged lepton, or to a quark and a neutrino, there are three possible event topologies that must be considered when studying leptoquark pair-production in  $e^+e^-$  collisions: two jets with two charged leptons, two jets with one charged lepton and missing energy, and two jets with missing energy.

Previous searches for leptoquarks have only looked for scalar leptoquarks. This thesis presents a search for evidence of vector leptoquarks in electron-positron annihilations at a centre-of-mass energy of 183 GeV, using data collected by the OPAL detector in 1997. Only leptoquarks which decay to first- or second-generation fermions were considered.

## 5.1 General Method of Searching for Evidence of Vector Leptoquarks

The search for evidence of vector leptoquarks was a multi-step process. First, simulated signal events in which leptoquarks were pair-produced in  $e^+e^-$  collisions at 183 GeV centre-of-mass energy, and subsequently decay, were generated. This was done for both first- and second-generation leptoquarks, for leptoquark masses ranging from 50 GeV/ $c^2$  to 90 GeV/ $c^2$ , in steps of 5 GeV/ $c^2$ , and for all three decay topologies. Decays to two jets and two neutrinos were termed Topology A, decays to two jets, one charged lepton and one neutrino were termed Topology B, and decays to two jets and two charged leptons were termed Topology C. Figure 5.1 shows the different decay topologies available to pair-produced leptoquarks.

Then, the various background processes were simulated for electron-positron collisions at a centre-of-mass energy of 183 GeV. Any event that can arise from an  $e^+e^-$  collision and can yield decay products similar to those of pair-produced leptoquarks, must be considered as a background to the signal.

The simulated signal events and simulated background events were passed through a full simulation of the OPAL detector.

At this point, various kinematic selection criteria (or *cuts*) were placed on both the simulated signal events and the simulated background events, in order to maximize the ratio of signal to background. Finally, these same selection criteria were applied to real data, collected using the OPAL detector, from  $e^+e^-$  collisions at a centre-of-mass energy of 183 GeV.

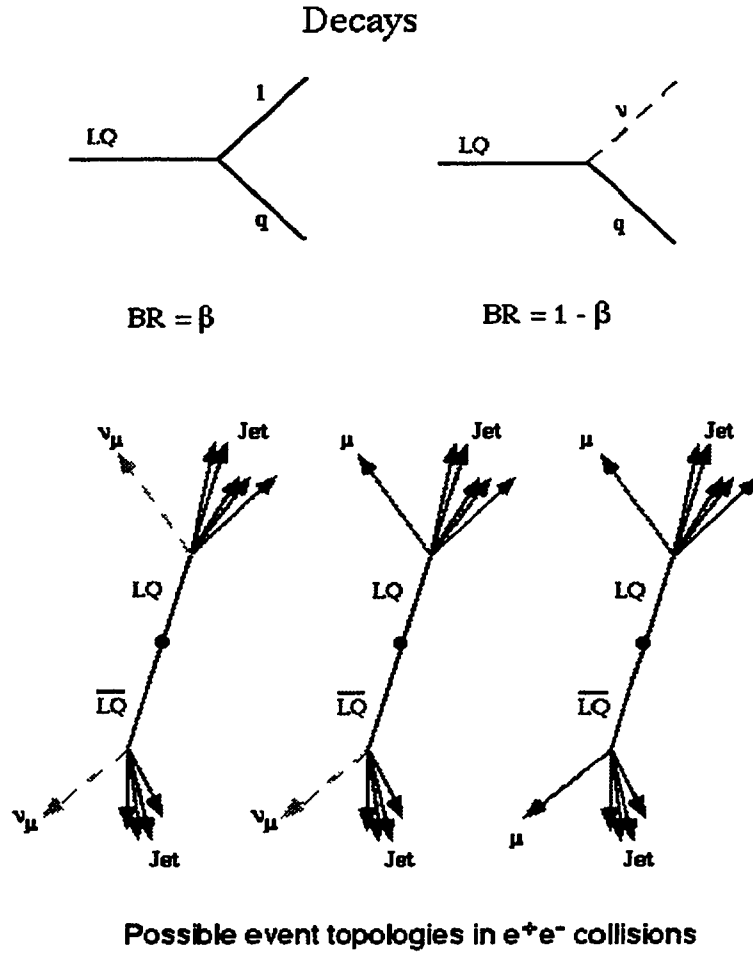


Figure 5.1: (*top*) Definition of branching fraction (also known as branching ratio (BR)); (*bottom*) the three decay topologies (A, B & C left-to-right) available to pair-produced leptoquarks.

## 5.2 Simulated Signal Events

Pair-produced leptoquark events in  $e^+e^-$  collisions at 183 GeV centre-of-mass energy were simulated using the Monte Carlo generator LQ2 [40]. Each leptoquark was forced to decay to a lepton-quark pair prior to fragmentation. Hadronization of the resulting quarks was simulated by the JETSET [41] package. The couplings  $\lambda_L$  and  $\lambda_R$  were both set to 0.001, in order to suppress the t-channel diagram, yet still allow leptoquark decays.

The most important QED (quantum electrodynamics) correction arises from initial state radiation, in which the beam electron or positron emits a photon prior to collision. The effect of initial state radiation has been calculated [42] and was included in the simulation. First-order soft and virtual corrections were also included. It is possible that QCD (quantum chromodynamics) corrections could be significant, however they were not included in the simulation.

1000 simulated signal events were generated for each decay topology (A, B & C) and for both first- and second-generation decays, for leptoquark masses of 50 GeV/ $c^2$  to 90 GeV/ $c^2$ , in steps of 5 GeV/ $c^2$ . Thus, there were a total of 54 different signal event samples.

Each signal event sample was passed through a full simulation of the OPAL detector, called GOPAL [43], which is based on the detector simulation package GEANT [44].

<i>Background</i>	<i>Run Number</i>	<i>Energy (GeV)</i>	<i>Cross-Section (pb)</i>	<i>Events Processed</i>
$e^+e^- \rightarrow Z^{0*}/\gamma^* \rightarrow q\bar{q}(\gamma)$	5050	183	$107.43 \pm 0.15$	93,500

Table 5.1: Cross-section for hadronic events from  $e^+e^- \rightarrow Z^{0*}/\gamma^* \rightarrow q\bar{q}(\gamma)$  at 183 GeV (PYTHIA).

### 5.3 Simulated Background Events

The following sources of background to the leptoquark signal from Standard Model processes were considered:

- Hadronic events from  $e^+e^- \rightarrow Z^{0*}/\gamma^* \rightarrow q\bar{q}(\gamma)$ . These events were simulated using the PYTHIA [41] generator.
- Hadronic events from two-photon processes ( $\gamma\gamma \rightarrow \text{hadrons}$ ). Two samples were generated: events where the  $Q^2$  of both photons is smaller than  $1.0 \text{ GeV}^2$  (untagged hadronic) were simulated using the PHOJET [45] generator, and events where the  $Q^2$  was greater than  $1.0 \text{ GeV}^2$  (tagged hadronic) were simulated using the HERWIG [46] generator.
- Four-lepton two-photon  $e^+e^-l^+l^-$  processes (where  $l^\pm$  is any charged lepton); simulated using the VERMASEREN [47] generator.
- All other four-fermion events; simulated using the GRC4F [48] generator.

Tables 5.1, 5.2, 5.3 and 5.4 show the background process, the OPAL Monte Carlo run number, the centre-of-mass energy of the simulation, the production cross-section, and the number of events simulated for each of the types of background.

<i>Background</i>	<i>Run Number</i>	<i>Energy (GeV)</i>	<i>Cross-Section (pb)</i>	<i>Events Processed</i>
<i>e-e-q-q</i>	1018	183	14,100	999,999
<i>e-e-q-q</i>	1126	184	$335.4 \pm 9.6$	100,000
<i>e-e-e-e</i>	1005	184	$795 \pm 26$	800,000
<i>e-e-<math>\mu</math>-<math>\mu</math></i>	1013	184	$600 \pm 20$	598,129
<i>e-e-<math>\tau</math>-<math>\tau</math></i>	1786	184	$432 \pm 4$	428,974

Table 5.2: Cross-sections for two-photon hadronic events (1018 (PHOJET) and 1126 (HERWIG)) and two-photon eell (VERMASEREN) at 183/4 GeV.

<i>Background</i>	<i>Run Number</i>	<i>Energy (GeV)</i>	<i>Cross-Section (pb)</i>	<i>Events Processed</i>
<i>e-e-e-e</i>	6819	184	19.0	100,000
<i>e-e-<math>\mu</math>-<math>\mu</math></i>	6615	184	13.0	100,000
<i>e-e-<math>\tau</math>-<math>\tau</math></i>	6616	184	1.81	18,122
<i>e-e-q-q</i>	7055	183	26.7	100,000

Table 5.3: Cross-sections for neutral current eeff via s-channel ( $\gamma/Z$ - $\gamma/Z$ ) and t-channel ( $\gamma/Z$ -ee) (GRC4F) at 183/4 GeV.

<i>Background</i>	<i>Run Number</i>	<i>Energy (GeV)</i>	<i>Cross-Section (pb)</i>	<i>Events Processed</i>
<i>q-q-q-q</i>	7051	183	7.86	16,024
<i>l-l-q-q</i>	7050	183	8.11	35,223
<i>l-l-l-l</i>	6641	184	3.05	30,000

Table 5.4: Cross-sections for neutral current (eg.  $Z\gamma$ ,  $ZZ$ ) and charged current (eg.  $WW$ ,  $W\nu$ ) processes (final states:  $qqqq$ ,  $llqq$ ,  $llll$ ) (GRC4F) at 183/4 GeV.

As was done for signal events, each background event sample was passed through GOPAL [43], the full simulation of the OPAL detector.

Figure 5.2 shows the various steps taken in the production and analysis of simulated signal and background events, and in the analysis of OPAL data. ROPE is the OPAL offline analysis software, capable of processing both raw OPAL data and simulated data. ROPE generates variables such as track parameters, vertex information,  $dE/dx$  of tracks in the jet chamber, energy deposition in calorimeters, and paths of muon candidates.

The OPAL Matching (MT) software package [49] was used to correct for the double counting of energy. The energy of charged particles is measured both in the central tracking chambers and in the calorimetry. It is therefore possible that a given charged particle will have its energy measured twice. So the contribution to the total energy will be twice as large as the correct amount. In order to minimize this possibility, the MT package matches tracks in the central tracking chambers with clusters in the calorimetry, and uses information from both subdetector systems to determine particle energies.

## 5.4 Selection Criteria

The output of the OPAL detector simulation when signal events were processed was compared to the output when background events were processed. Event variables such as missing momentum, visible energy, and number of charged tracks were computed in each case. Also, topological properties such as the number of jets, angular distributions and invariant masses were computed. These variables and features of the simulated signal and background events were compared, in order to

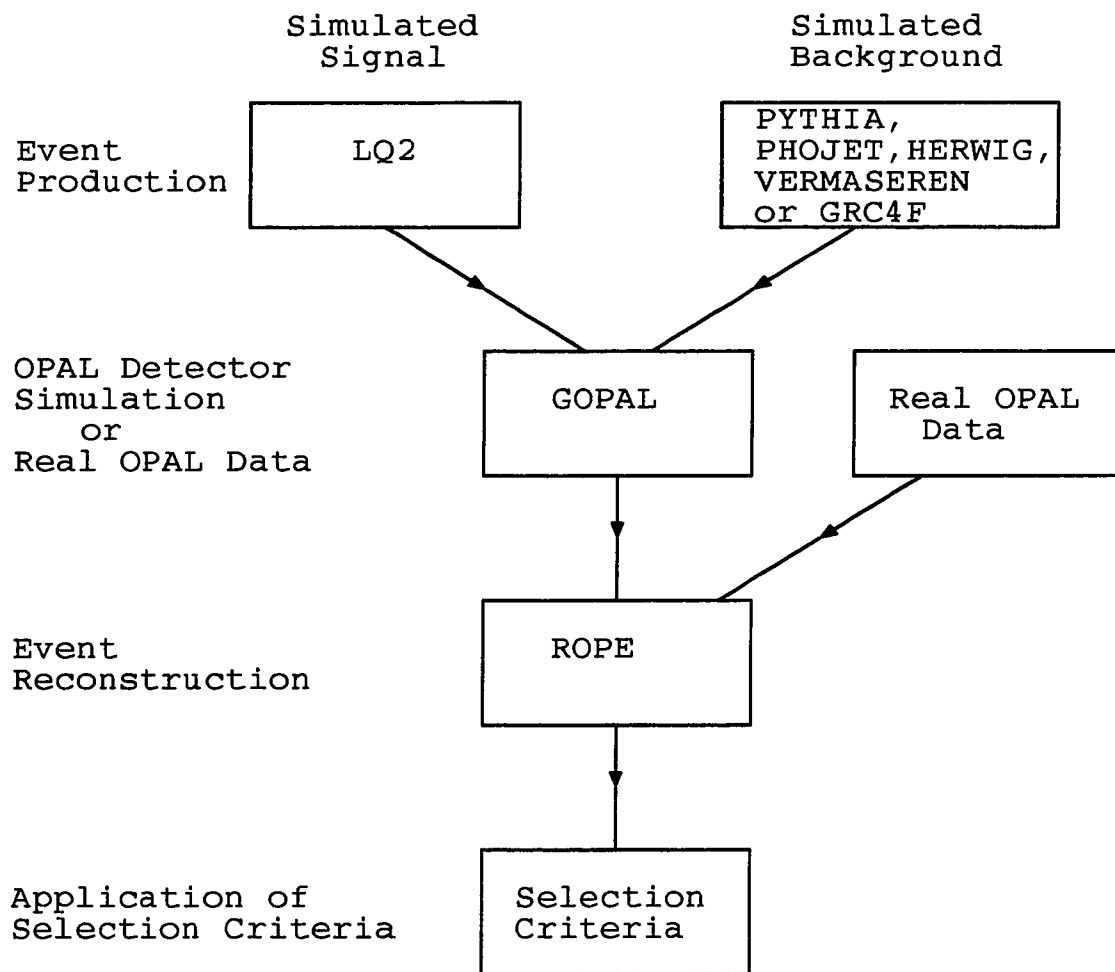


Figure 5.2: Flow chart showing the steps taken in the production and analysis of simulated signal and background events, and in the analysis of OPAL data.

find differences between the signal events and the background events. The goal was to develop a set of kinematic selection criteria which select (or accept) the signal events, but reject the background events. In reality, some of the signal events will be rejected and a few of the background events will be accepted, however, each selection criterion is designed to minimize the background while preserving as much of the signal as possible.

Jet-finding was performed using the Durham jet-finding scheme [50]. Lepton identification was performed using the ID package, as described in reference [51].

Charged tracks were required to have at least 20 measured space points, a transverse momentum relative to the beam direction of at least 120 MeV/c, and at least 50% of the hits which are geometrically expected. Good electromagnetic clusters are defined as having energy greater than 100 MeV in the barrel or 250 MeV in the endcaps. Clusters in the endcaps were also required to contain at least two adjacent lead glass blocks. Clusters in the hadron calorimeter were required to have an energy of at least 0.6 GeV.

The selection criteria that were used are similar to those in reference [16].

#### 5.4.1 Preselection Criteria

Loose preselection criteria (or *cuts*) were used in order to remove any events which clearly did not fit the profile required for pair-produced leptoquark events.

The preselection criteria require that for each event:

- The fraction of good charged tracks must be greater than 0.2
- There must be at least 5 good charged tracks

- There must be at least 5 good electromagnetic clusters
- The visible energy must be greater than 36.6 GeV, which is 0.2 times the centre-of-mass energy of 183 GeV

The first preselection criteria is intended to eliminate beam-wall and beam-gas interactions. The last three preselection criteria reject a large fraction of the two-photon background events.

The selection criteria that were applied after the preselection criteria differ for each of the three topologies (Type A - two jets and two neutrinos; Type B - two jets, one neutrino and one charged lepton; Type C - two jets and two charged leptons). Thus, each topology was searched for separately.

#### 5.4.2 Type A Selection Criteria

To search for events where the pair-produced leptoquarks decay to two quarks and two neutrinos, the following selection criteria were applied:

- Cut A1 - Require  $R_{vis} = E_{vis}/E_{cm}$  to satisfy  $0.25 < R_{vis} < 0.75$  ( $E_{vis}$  is the visible energy, and  $E_{cm}$  is the centre-of mass energy)
- Cut A2 - Require the angle  $\theta_{mis}$  between missing momentum and the  $z$ -axis to satisfy  $|\cos(\theta_{mis})| < 0.9$
- Cut A3 - Require missing transverse momentum to be greater than 30 GeV/c
- Cut A4 - Require  $Y_{23}$ , the resolution parameter when reconstructing events into two jets, to be less than 0.05

- Cut A5 - Require angle  $\theta_{jj}$  between jets (acolinear) to satisfy  $\cos(\theta_{jj}) > -0.25$ , and the angle  $\phi_{jj}$  between jet projections onto the  $r$ - $\phi$  plane (acoplanar) to satisfy  $\cos(\phi_{jj}) > -0.75$
- Cut A6 - Require the invariant mass of the two jets to lie outside the mass region between 75 and 95 GeV/c<sup>2</sup>
- Cut A7 - Require no identified charged lepton with energy greater than 10 GeV

Cuts A1, A2 and A3 were useful in rejecting two-photon background events. Cuts A2 and A5 greatly reduce  $Z^{0*}/\gamma^* \rightarrow q\bar{q}(\gamma)$  background events. Cuts A4, A6 and A7 are most useful in rejecting four-fermion background events.

### 5.4.3 Type B Selection Criteria

To search for events where the pair-produced leptoquarks decay to two quarks, one charged lepton and one neutrino, the following selection criteria were applied:

- Cut B1 - Require  $R_{vis} = E_{vis}/E_{cm}$  to satisfy  $0.5 < R_{vis} < 1.0$
- Cut B2 - Require the angle  $\theta_{mis}$  between missing momentum and the  $z$ -axis to satisfy  $|\cos(\theta_{mis})| < 0.9$
- Cut B3 - Require  $R_{mis}$  (the ratio between missing momentum and  $\sqrt{s}$ ) to satisfy  $R_{mis} > 0.23$
- Cut B4 - Require at least one identified lepton with energy greater than 14 GeV
- Cut B5 - Require no charged tracks and at most one electromagnetic cluster within a cone of half-aperture 20 degrees around the most energetic lepton

- Cut B6 - Require the angle  $\theta_{jj}$  between the two jet directions to satisfy  $\cos(\theta_{jj}) > -0.20$
- Cut B7 - Require the invariant mass of the two jets to lie outside the mass region between 75 and 85 GeV/c<sup>2</sup>

Cuts B1, B2, B3 and B4 were useful in rejecting two-photon background events. Cuts B2, B4, B6 and B7 greatly reduce four-fermion background events. Cuts B2, B4 and B5 are particularly useful in rejecting  $Z^{0*}/\gamma^* \rightarrow q\bar{q}(\gamma)$  background events.

#### 5.4.4 Type C Selection Criteria

To search for events where the pair-produced leptoquarks decay to two quarks and two charged leptons, the following selection criteria were applied:

- Cut C1 - Require  $R_{vis} = E_{vis}/E_{cm}$  to satisfy  $0.75 < R_{vis} < 1.25$
- Cut C2 - Require  $Y_{43}$ , the resolution parameter when reconstructing events into four jets, to be greater than 0.01
- Cut C3 - Require at least one pair of oppositely charged leptons
- Cut C4 - Require lepton 1 energy to be greater than 32 GeV, lepton 2 energy to be greater than 30 GeV for electrons; require lepton 1 energy to be greater than 35 GeV, lepton 2 energy to be greater than 30 GeV for muons
- Cut C5 - Require no charged tracks and at most one electromagnetic cluster within a cone of half-aperture 15 degrees around the most energetic lepton

Cuts C1, C2 and C3 were useful in rejecting two-photon background events. Cuts C3 and C4 greatly reduce four-fermion and  $Z^{0*}/\gamma^* \rightarrow q\bar{q}(\gamma)$  background events. Cut C5 is particularly useful in rejecting  $Z^{0*}/\gamma^* \rightarrow q\bar{q}(\gamma)$  background events.

## 5.5 Effect of Selection Criteria on Signal

The effect of the selection criteria on a signal sample is expressed as an efficiency. If no signal events are rejected by the cuts, then the efficiency of the cut would be 100%. In reality, efficiencies are much lower than this, which is a result of designing cuts which greatly reduce the background. The efficiency is simply the number of simulated signal events which pass the cuts, divided by the total number of signal events.

Simulated signal samples were generated for first- and second-generation decays, for all three topologies, and for masses of 50 GeV/c<sup>2</sup> to 90 GeV/c<sup>2</sup> in steps of 5 GeV/c<sup>2</sup>. Each signal sample consisted of 1000 events. Tables 5.5, 5.6 and 5.7 show the number of signal events remaining after each successive cut, and the signal efficiencies for the three decay topologies (A, B & C) for first-generation leptoquark decays. Tables 5.8, 5.9 and 5.10 show the number of signal events remaining after each successive cut, and the signal efficiencies for the three decay topologies for second-generation leptoquark decays.

Figure 5.3 shows plots of signal efficiency versus leptoquark mass for all three topologies (C, B & A), for first-generation leptoquarks. Figure 5.4 shows plots of signal efficiency versus leptoquark mass for all three topologies (C, B & A), for second-generation leptoquarks. The efficiencies increase in all six cases as the leptoquark mass approaches the kinematic threshold of  $M_{LQ} = \sqrt{s}/2$ . This is

<i>LQ Mass (GeV/c<sup>2</sup>)</i>	50	55	60	65	70	75	80	85	90
<i>Original</i>	1000	1000	1000	1000	1000	1000	1000	1000	1000
<i>Preselection</i>	938	955	954	953	966	968	971	977	979
<i>After A1</i>	775	808	816	840	868	900	918	946	963
<i>After A2</i>	707	747	758	773	816	842	854	882	901
<i>After A3</i>	510	553	579	603	654	669	695	734	759
<i>After A4</i>	481	528	545	569	621	641	673	710	729
<i>After A5</i>	208	265	303	348	391	423	480	509	526
<i>After A6</i>	198	256	282	323	357	382	424	447	478
<i>After A7</i>	165	209	218	258	278	284	308	330	334
<i>Efficiency (%)</i>	16.5	20.9	21.8	25.8	27.8	28.4	30.8	33.0	33.4

Table 5.5: Number of events remaining after selection criteria have been applied, and corresponding efficiency for first-generation decays via Topology A.

<i>LQ Mass (GeV/c<sup>2</sup>)</i>	50	55	60	65	70	75	80	85	90
<i>Original</i>	1000	1000	1000	1000	1000	1000	1000	1000	1000
<i>Preselection</i>	981	972	986	981	988	979	981	986	983
<i>After B1</i>	892	912	917	918	940	919	945	956	964
<i>After B2</i>	811	831	839	836	861	836	864	884	888
<i>After B3</i>	479	514	532	556	568	560	564	583	597
<i>After B4</i>	407	450	488	507	523	517	516	546	537
<i>After B5</i>	338	379	392	426	454	434	433	469	472
<i>After B6</i>	133	178	190	206	223	223	253	278	286
<i>After B7</i>	130	171	177	195	207	209	235	260	260
<i>Efficiency (%)</i>	13.0	17.1	17.7	19.5	20.7	20.9	23.5	26.0	26.0

Table 5.6: Number of events remaining after selection criteria have been applied, and corresponding efficiency for first-generation decays via Topology B.

<i>LQ Mass (GeV/c<sup>2</sup>)</i>	50	55	60	65	70	75	80	85	90
<i>Original</i>	1000	1000	1000	1000	1000	1000	1000	1000	1000
<i>Preselection</i>	990	985	985	987	985	989	990	987	987
<i>After C1</i>	938	924	948	949	940	930	965	952	957
<i>After C2</i>	575	570	586	575	574	614	634	697	755
<i>After C3</i>	524	528	543	519	534	570	584	655	709
<i>After C4</i>	244	266	282	298	320	358	402	561	658
<i>After C5</i>	229	254	274	284	307	342	389	538	624
<i>Efficiency (%)</i>	22.9	25.4	27.4	28.4	30.7	34.2	38.9	53.8	62.4

Table 5.7: Number of events remaining after selection criteria have been applied, and corresponding efficiency for first-generation decays via Topology C.

<i>LQ Mass (GeV/c<sup>2</sup>)</i>	50	55	60	65	70	75	80	85	90
<i>Original</i>	1000	1000	1000	1000	1000	1000	1000	1000	1000
<i>Preselection</i>	942	954	957	964	959	966	991	981	987
<i>After A1</i>	795	817	839	855	872	891	951	958	971
<i>After A2</i>	736	750	769	803	830	831	884	891	907
<i>After A3</i>	495	539	575	637	670	682	711	726	743
<i>After A4</i>	462	508	549	603	645	665	690	699	711
<i>After A5</i>	187	253	304	345	399	435	485	507	545
<i>After A6</i>	185	243	293	322	358	387	439	459	512
<i>After A7</i>	147	191	233	249	288	292	324	331	360
<i>Efficiency (%)</i>	14.7	19.1	23.3	24.9	28.8	29.2	32.4	33.1	36.0

Table 5.8: Number of events remaining after selection criteria have been applied, and corresponding efficiency for second-generation decays via Topology A.

<i>LQ Mass (GeV/c<sup>2</sup>)</i>	50	55	60	65	70	75	80	85	90
<i>Original</i>	1000	1000	1000	1000	1000	1000	1000	1000	1000
<i>Preselection</i>	977	985	980	985	986	988	984	988	982
<i>After B1</i>	866	876	898	897	906	916	914	934	930
<i>After B2</i>	772	791	822	827	815	835	848	866	867
<i>After B3</i>	514	535	559	564	555	559	590	576	578
<i>After B4</i>	469	481	527	529	516	534	566	547	539
<i>After B5</i>	395	399	454	452	446	465	506	483	470
<i>After B6</i>	172	206	242	257	269	292	329	348	349
<i>After B7</i>	172	202	237	249	257	280	315	331	330
<i>Efficiency (%)</i>	17.2	20.2	23.7	24.9	25.7	28.0	31.5	33.1	33.0

Table 5.9: Number of events remaining after selection criteria have been applied, and corresponding efficiency for second-generation decays via Topology B.

<i>LQ Mass (GeV/c<sup>2</sup>)</i>	50	55	60	65	70	75	80	85	90
<i>Original</i>	1000	1000	1000	1000	1000	1000	1000	1000	1000
<i>Preselection</i>	985	978	982	991	980	985	987	988	986
<i>After C1</i>	905	898	889	912	899	888	907	910	896
<i>After C2</i>	552	537	532	535	541	554	583	680	706
<i>After C3</i>	516	515	504	502	511	524	561	640	677
<i>After C4</i>	240	263	255	288	308	317	406	543	633
<i>After C5</i>	229	256	247	280	296	309	399	526	617
<i>Efficiency (%)</i>	22.9	25.6	24.7	28.0	29.6	30.9	39.9	52.6	61.7

Table 5.10: Number of events remaining after selection criteria have been applied, and corresponding efficiency for second-generation decays via Topology C.

due to the fact that the selection criteria were designed to select leptoquarks with large masses, since leptoquarks with lower masses have previously been excluded. It is also worth noting that the high-mass leptoquarks are less boosted, and so their decay products are more separated, and thus easier to identify.

There is an uncertainty on the signal efficiencies due to the number of signal events simulated. For each vector leptoquark mass, 1000 signal events were simulated. The number of events which passed all of the selection criteria ranged from 130 to 624. This corresponds to statistical uncertainties of 9% to 4% respectively. We are most interested in the high mass region, where our signal efficiencies have a statistical uncertainty of 4% to 6%, depending on the topology. We also estimate a systematic uncertainty of 10% in the signal simulation. This was obtained by displacing the values of the selection criteria by an amount corresponding to the difference between the mean values of each variable in the simulation and in the data, and then taking the difference between the efficiency so obtained and the original efficiency as a systematic error. The systematic uncertainty includes a small error associated with lepton identification (3.2% for electrons; 2.5% for muons) [52]. The statistical and systematic uncertainties were assumed to be independent, and were added in quadrature.

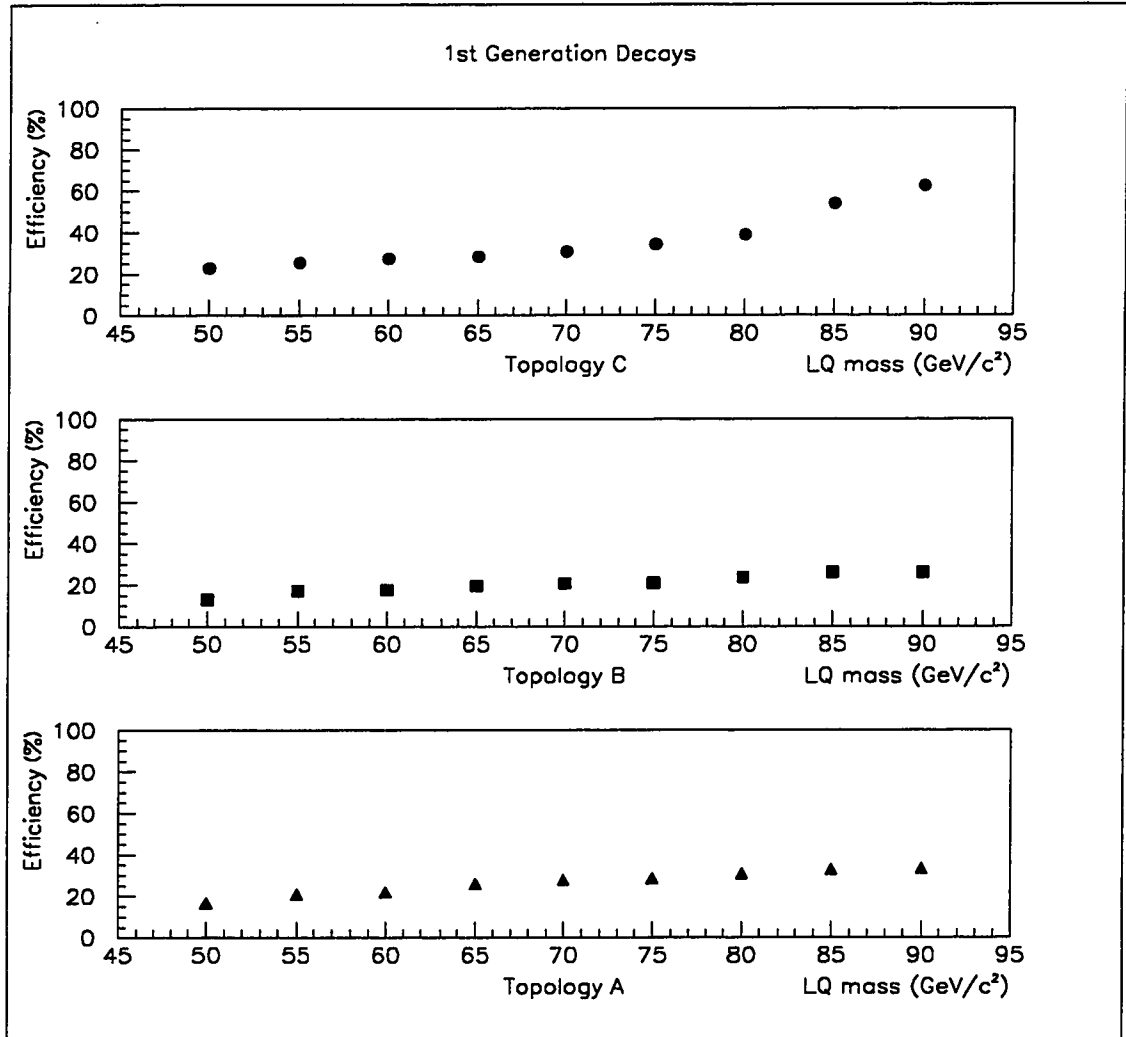


Figure 5.3: Signal efficiency versus leptoquark mass for all three topologies (C, B & A), for first-generation leptoquarks.

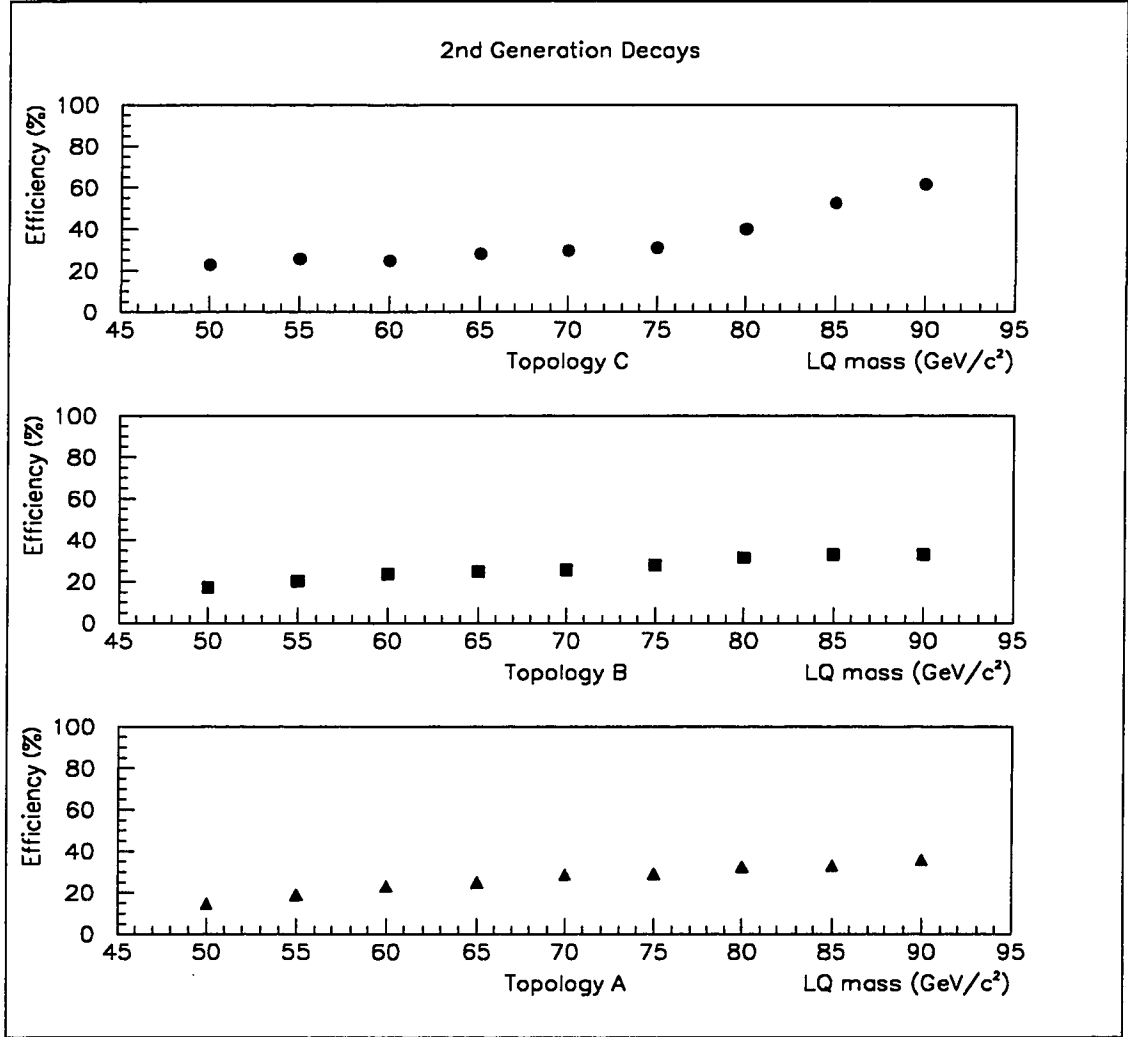


Figure 5.4: Signal efficiency versus leptoquark mass for all three topologies (C, B & A), for second-generation leptoquarks.

<i>Background</i>	$Z^{0*}/\gamma^* \rightarrow q\bar{q}(\gamma)$	Two-photon $eeqq$ Untagged Hadronic	Two-photon $eeqq$ Tagged Hadronic
<i>Run Number</i>	5050	1018	1126
<i>Original</i>	93,500	999,999	100,000
<i>Preselection</i>	88,804	17,565	19,526
<i>After A1</i>	42,245	8,540	15,792
<i>After A2</i>	13,013	3,018	9,002
<i>After A3</i>	2,126	6	19
<i>After A4</i>	2,030	6	18
<i>After A5</i>	0	1	0
<i>After A6</i>	0	1	0
<i>After A7</i>	0	1	0
<i>Remaining</i>	0.00%	0.0001%	0.00%

Table 5.11: Number of events remaining after each successive cut, for type A selection criteria. (Runs 5050, 1018 & 1126.)

## 5.6 Effect of Selection Criteria on Backgrounds

The intent of the selection criteria is to reject the background events. Ideally, the cuts would reject all of the background events. In reality, some of the background events do pass the cuts, but, the vast majority (>99%) of the background events are rejected.

Tables 5.11, 5.12, 5.13, and 5.14 show the effect of each of the type A selection criteria on the various background samples. Tables 5.15, 5.16, 5.17, and 5.18 show the effect of each of the type B selection criteria on the various background samples. Tables 5.19, 5.20, 5.21, and 5.22 show the effect of each of the type C selection criteria on the various background samples.

Table 5.23 summarizes the results of the cuts, and shows the number of events processed and the number of events which pass the selection criteria for each

<i>Background</i>	Two photon <i>eell</i> <i>e-e-e-e</i>	Two-photon <i>eell</i> <i>e-e-μ-μ</i>	Two-photon <i>eell</i> <i>e-e-τ-τ</i>
<i>Run Number</i>	1005	1013	1786
<i>Original</i>	800.000	598,129	428,974
<i>Preselection</i>	2	0	275
<i>After A1</i>	1	0	223
<i>After A2</i>	1	0	130
<i>After A3</i>	0	0	3
<i>After A4</i>	0	0	3
<i>After A5</i>	0	0	0
<i>After A6</i>	0	0	0
<i>After A7</i>	0	0	0
<i>Remaining</i>	0.00%	0.00%	0.00%

Table 5.12: Number of events remaining after each successive cut, for type A selection criteria. (Runs 1005, 1013 & 1786.)

<i>Background</i>	<i>eeff</i> <i>e-e-e-e</i>	<i>eeff</i> <i>e-e-μ-μ</i>	<i>eeff</i> <i>e-e-τ-τ</i>	<i>eeff</i> <i>e-e-q-q</i>
<i>Run Number</i>	6819	6615	6616	7055
<i>Original</i>	100,000	100,000	18,122	100,000
<i>Preselection</i>	5	1	187	12,151
<i>After A1</i>	1	0	128	8,416
<i>After A2</i>	1	0	46	2,278
<i>After A3</i>	0	0	12	349
<i>After A4</i>	0	0	9	328
<i>After A5</i>	0	0	0	0
<i>After A6</i>	0	0	0	0
<i>After A7</i>	0	0	0	0
<i>Remaining</i>	0.00%	0.00%	0.00%	0.00%

Table 5.13: Number of events remaining after each successive cut, for type A selection criteria. (Runs 6819, 6615, 6616 & 7055.)

<i>Background</i>	<i>ffff</i>	<i>ffff</i>	<i>ffff</i>
	<i>q-q-q-q</i>	<i>l-l-q-q</i>	<i>l-l-l-l</i>
<i>Run Number</i>	7051	7050	6641
<i>Original</i>	16,024	35,223	30,000
<i>Preselection</i>	15,947	33,903	164
<i>After A1</i>	377	17,895	139
<i>After A2</i>	154	15,948	125
<i>After A3</i>	28	10,886	68
<i>After A4</i>	23	6,122	66
<i>After A5</i>	0	443	25
<i>After A6</i>	0	311	24
<i>After A7</i>	0	168	14
<i>Remaining</i>	0.00%	0.477%	0.047%

Table 5.14: Number of events remaining after each successive cut, for type A selection criteria. (Runs 7051, 7050 & 6641.)

<i>Background</i>	$Z^0/\gamma^* \rightarrow q\bar{q}(\gamma)$	Two-photon <i>eeqq</i> Untagged Hadronic	Two-photon <i>eeqq</i> Tagged Hadronic
<i>Run Number</i>	5050	1018	1126
<i>Original</i>	93,500	999,999	100,000
<i>Preselection</i>	88,804	17,565	19,526
<i>After B1</i>	63,229	157	11,967
<i>After B2</i>	27,129	67	7,755
<i>After B3</i>	5,979	4	35
<i>After B4</i>	1,775	1	14
<i>After B5</i>	62	0	9
<i>After B6</i>	6	0	5
<i>After B7</i>	6	0	5
<i>Remaining</i>	0.0064%	0.00%	0.005%

Table 5.15: Number of events remaining after each successive cut, for type B selection criteria. (Runs 5050, 1018 & 1126.)

<i>Background</i>	Two photon <i>eell</i> <i>e-e-e-e</i>	Two-photon <i>eell</i> <i>e-e-μ-μ</i>	Two-photon <i>eell</i> <i>e-e-τ-τ</i>
<i>Run Number</i>	1005	1013	1786
<i>Original</i>	800,000	598,129	428,974
<i>Preselection</i>	2	0	275
<i>After B1</i>	1	0	181
<i>After B2</i>	1	0	110
<i>After B3</i>	0	0	4
<i>After B4</i>	0	0	3
<i>After B5</i>	0	0	1
<i>After B6</i>	0	0	0
<i>After B7</i>	0	0	0
<i>Remaining</i>	0.00%	0.00%	0.00%

Table 5.16: Number of events remaining after each successive cut, for type B selection criteria. (Runs 1005, 1013 & 1786.)

<i>Background</i>	<i>eeff</i> <i>e-e-e-e</i>	<i>eeff</i> <i>e-e-μ-μ</i>	<i>eeff</i> <i>e-e-τ-τ</i>	<i>eeff</i> <i>e-e-q-q</i>
<i>Run Number</i>	6819	6615	6616	7055
<i>Original</i>	100,000	100,000	18,122	100,000
<i>Preselection</i>	5	1	187	12,151
<i>After B1</i>	3	0	102	8,280
<i>After B2</i>	3	0	47	2,582
<i>After B3</i>	1	0	14	647
<i>After B4</i>	1	0	11	239
<i>After B5</i>	0	0	7	103
<i>After B6</i>	0	0	1	14
<i>After B7</i>	0	0	1	13
<i>Remaining</i>	0.00%	0.00%	0.0055%	0.013%

Table 5.17: Number of events remaining after each successive cut, for type B selection criteria. (Runs 6819, 6615, 6616 & 7055.)

<i>Background</i>	<i>ffff</i> <i>q-q-q-q</i>	<i>ffff</i> <i>l-l-q-q</i>	<i>ffff</i> <i>l-l-l-l</i>
<i>Run Number</i>	7051	7050	6641
<i>Original</i>	16,024	35,223	30,000
<i>Preselection</i>	15,947	33,903	164
<i>After B1</i>	6,526	31,045	65
<i>After B2</i>	4,975	27,943	55
<i>After B3</i>	712	15,262	21
<i>After B4</i>	205	10,989	17
<i>After B5</i>	2	7,532	11
<i>After B6</i>	0	166	6
<i>After B7</i>	0	142	6
<i>Remaining</i>	0.00%	0.403%	0.02%

Table 5.18: Number of events remaining after each successive cut, for type B selection criteria. (Runs 7051, 7050 & 6641.)

<i>Background</i>	$Z^{0*}/\gamma^* \rightarrow q\bar{q}(\gamma)$	Two-photon <i>eeqq</i> Untagged Hadronic	Two-photon <i>eeqq</i> Tagged Hadronic
<i>Run Number</i>	5050	1018	1126
<i>Original</i>	93,500	999,999	100,000
<i>Preselection</i>	88,804	17,565	19,526
<i>After C1</i>	45,370	8	2,974
<i>After C2</i>	3,238	0	614
<i>After C3</i>	1,557	0	11
<i>After C4</i>	22	0	1
<i>After C5</i>	0	0	1
<i>Remaining</i>	0.00%	0.00%	0.001%

Table 5.19: Number of events remaining after each successive cut, for type C selection criteria. (Runs 5050, 1018 & 1126.)

<i>Background</i>	Two photon <i>eell</i> <i>e-e-e-e</i>	Two-photon <i>eell</i> <i>e-e-μ-μ</i>	Two-photon <i>eell</i> <i>e-e-τ-τ</i>
<i>Run Number</i>	1005	1013	1786
<i>Original</i>	800,000	598,129	429,974
<i>Preselection</i>	2	0	275
<i>After C1</i>	1	0	33
<i>After C2</i>	0	0	0
<i>After C3</i>	0	0	0
<i>After C4</i>	0	0	0
<i>After C5</i>	0	0	0
<i>Remaining</i>	0.00%	0.00%	0.00%

Table 5.20: Number of events remaining after each successive cut, for type C selection criteria. (Runs 1005, 1013 & 1786.)

<i>Background</i>	<i>eeff</i> <i>e-e-e-e</i>	<i>eeff</i> <i>e-e-μ-μ</i>	<i>eeff</i> <i>e-e-τ-τ</i>	<i>eeff</i> <i>e-e-q-q</i>
<i>Run Number</i>	6819	6615	6616	7055
<i>Original</i>	100,000	100,000	18,122	100,000
<i>Preselection</i>	5	1	187	12,151
<i>After C1</i>	4	1	54	3,415
<i>After C2</i>	0	0	2	401
<i>After C3</i>	0	0	2	246
<i>After C4</i>	0	0	1	79
<i>After C5</i>	0	0	1	53
<i>Remaining</i>	0.00%	0.00%	0.006%	0.053%

Table 5.21: Number of events remaining after each successive cut, for type C selection criteria. (Runs 6819, 6615, 6616 & 7055.)

<i>Background</i>	<i>ffff</i> <i>q-q-q-q</i>	<i>ffff</i> <i>l-l-q-q</i>	<i>ffff</i> <i>l-l-l-l</i>
<i>Run Number</i>	7051	7050	6641
<i>Original</i>	16,024	35,223	30,000
<i>Preselection</i>	15,947	33,903	164
<i>After C1</i>	15,249	15,830	19
<i>After C2</i>	10,744	2,272	4
<i>After C3</i>	7,089	1,210	4
<i>After C4</i>	28	125	2
<i>After C5</i>	0	103	2
<i>Remaining</i>	0.00%	0.292%	0.007%

Table 5.22: Number of events remaining after each successive cut, for type C selection criteria. (Runs 7051, 7050 & 6641.)

topology (A, B and C) and for each background process studied (by run number).

We can define a background rejection factor for each set of cuts and for each background process studied, as the number of events remaining after applying the selection criteria, divided by the number of events processed.

So we have obtained rejection factors for each of the background processes, and for each of the three sets of selection criteria. We know the production cross-section for each of the background processes. However, to calculate the expected number of background events in the data that would pass the selection criteria, we need to know the luminosity of the data collected.

During 1997, the OPAL detector collected a total of  $65.2 \text{ pb}^{-1}$  of data. However, not all of the data samples were collected when LEP was operating at a centre-of-mass energy of 183 GeV. Some data samples were collected for centre-of-mass energies of 91 GeV, 130 GeV and 136 GeV. The total integrated luminosity recorded at centre-of-mass energies between 182 GeV and 184 GeV is  $57.3 \text{ pb}^{-1}$ . The amount

<i>Background Process</i>	<i>Total Number of Events Processed</i>	Type A	Type B	Type C
5050	93.500	0	6	0
1018	999.999	1	0	0
1126	100.000	0	5	1
1005	800.000	0	0	0
1013	598.129	0	0	0
1786	428.974	0	0	0
6819	100.000	0	0	0
6615	100.000	0	0	0
6616	18.122	0	1	1
7055	100.000	0	13	53
7051	16.024	0	0	0
7050	35.223	168	142	103
6641	30.000	14	6	2

Table 5.23: Number of events processed and the number of events which pass the selection criteria for each topology (A, B and C) and for each background process (by run number).

of data collected while all of the subdetector components were operating correctly is  $55.9 \text{ pb}^{-1}$ . This is the data sample that was analyzed for this thesis, and is referred to as the 183 GeV data sample. It corresponds to OPAL data-taking periods 84, 85, 86, 88 and 89.

The expected number of events in the data sample for each background process is calculated as the production cross-section of the background process multiplied by the integrated luminosity:

$$N_{expected}^{before\ cuts} = \sigma_{prod} \cdot \int Ldt. \quad (5.5.6.1)$$

The number of events  $n$  (for a particular background process) that are expected to survive a set of selection criteria is this product multiplied by the rejection factor:

$$n = \frac{n_0}{N} \cdot \sigma_{prod} \cdot \int Ldt, \quad (5.5.6.2)$$

where  $n_0$  is the number of background events that pass the selection criteria, and  $N$  is the total number of events in the background sample.

Table 5.24 shows the number of background events in the  $55.9 \text{ pb}^{-1}$  of data that are expected to pass the cuts, for each of the background processes and for each of the three sets of selection criteria, including uncertainties.

The uncertainties include statistical errors on the number of events passing the selection criteria, a small error on the integrated luminosity, and an error on the cross-section for each background process.

To determine the statistical error on the number of background events passing the selection criteria, we have calculated the 68.27% confidence level interval using the results of Feldman and Cousins [53], as recommended by the Particle Data Group [54]. When determining a confidence level interval, an additional criterion is

<i>Background</i>	Type A	Type B	Type C
5050	$0^{+0.0828}$	$0.385^{+0.211}_{-0.140}$	$0^{+0.0828}$
1018	$0.788^{+1.379}_{-0.497}$	$0^{+1.016}$	$0^{+1.016}$
1126	$0^{+0.242}$	$0.937^{+0.527}_{-0.423}$	$0.187^{+0.328}_{-0.118}$
1005	$0^{+0.0716}$	$0^{+0.0716}$	$0^{+0.0716}$
1013	$0^{+0.0723}$	$0^{+0.0723}$	$0^{+0.0723}$
1786	$0^{+0.0726}$	$0^{+0.0726}$	$0^{+0.0726}$
6819	$0^{+0.0137}$	$0^{+0.0137}$	$0^{+0.0137}$
6615	$0^{+0.00937}$	$0^{+0.00937}$	$0^{+0.00937}$
6616	$0^{+0.00720}$	$0.00558^{+0.00977}_{-0.00352}$	$0.00558^{+0.00977}_{-0.00352}$
7055	$0^{+0.0192}$	$0.194^{+0.0646}_{-0.0560}$	$0.791 \pm 0.113$
7051	$0^{+0.0354}$	$0^{+0.0354}$	$0^{+0.0354}$
7050	$2.161 \pm 0.188$	$1.827 \pm 0.170$	$1.325 \pm 0.141$
6641	$0.0795^{+0.0248}_{-0.0213}$	$0.0341^{+0.0187}_{-0.0125}$	$0.0114^{+0.0128}_{-0.0072}$
Totals:	$3.028^{+1.421}_{-0.532}$	$3.382^{+1.186}_{-0.480}$	$2.320^{+1.094}_{-0.216}$

Table 5.24: Number of background events in the  $55.9 \text{ pb}^{-1}$  of data that are expected to pass the selection criteria, including statistical uncertainties, for each of the background processes and for each of the three sets of selection criteria.

needed to determine the interval uniquely. The most common criterion is to choose the central interval, such that the area of the excluded tail on either side of the Poisson probability distribution is  $(1 - 0.6827)/2 = 16\%$ . Feldman and Cousins have developed a general ordering principle which reduces to the central interval in the usual cases but produces confidence intervals with better properties when in the neighbourhood of a physical limit.

For cases where a large number of background events passed the selection criteria, the uncertainties are taken to be the square root of the number of events.

The error on the integrated luminosity of the 183 GeV data sample is 0.5%. The errors on the background cross-sections are taken as they appear in Section 5.3, or are assumed to be 4% if not specified.

The error in the number of background events  $n$  in the 183 GeV data sample that are expected to survive the selection criteria is given by:

$$\frac{\delta n}{n} \approx \left[ \left( \frac{\delta n_0}{n_0} \right)^2 + \left( \frac{\delta N}{N} \right)^2 + \left( \frac{\delta \sigma_{prod}}{\sigma_{prod}} \right)^2 + \left( \frac{\delta(\int Ldt)}{\int Ldt} \right)^2 \right]^{\frac{1}{2}}, \quad (5.5.6.3)$$

where  $n_0$  is the number of background events that pass the selection criteria,  $N$  is the total number of events in the background sample,  $\sigma_{prod}$  is the cross-section of the background process, and  $\int Ldt$  is the integrated luminosity. The correlation between  $n_0$  and  $N$  is neglected, giving us uncertainties that are overestimated by less than 0.07%.

In cases where no background events passed the selection criteria, the error in the number of events is given by:

$$\delta n = \frac{\sigma_{prod} \cdot \int Ldt}{N} \delta n_0. \quad (5.5.6.4)$$

The total expected number of background events in the data sample, for

each topology, is simply the sum of the contributions from each background process. These totals are also shown in Table 5.24. The uncertainties from each background process have been added in quadrature.

The uncertainties in Table 5.24 are statistical only. We estimate a systematic error of 10% in the background simulation. This value was determined using the same approach as for the systematic error in the signal efficiencies: the values of the selection criteria were displaced by an amount corresponding to the difference between the mean values of each variable in the simulation and in the data. Then, the systematic error was taken to be the difference between the number of background events remaining after the new selection criteria have been applied, and the number of background events that remained after the original selection criteria were applied. The statistical and systematic uncertainties are assumed to be independent, and are added in quadrature.

Thus, when searching for Topology A, the expected number of background events surviving the selection criteria, for  $55.9 \text{ pb}^{-1}$  of data, is  $3.03^{+1.45}_{-0.61}$  events; for Topology B it is  $3.38^{+1.24}_{-0.59}$  events; and for Topology C it is  $2.32^{+1.11}_{-0.32}$  events.

<i>Topology</i>	Type A	Type B	Type C
<i>Number of Data Events Which Pass the Cuts</i>	4	3	1

Table 5.25: The number of data events which pass each set of selection criteria, in the  $55.9 \text{ pb}^{-1}$  of data recorded by OPAL in 1997, at a centre-of-mass energy of 183 GeV.

## 5.7 183 GeV Data Sample

As previously explained, the integrated luminosity of the data sample collected by the OPAL detector in 1997, at a centre-of-mass energy near 183 GeV, is  $55.9 \text{ pb}^{-1}$ .

The previously described sets of selection criteria (types A, B and C) were each applied to the  $55.9 \text{ pb}^{-1}$  data sample. A total of 4 events passed the type A selection criteria, 3 events passed the type B selection criteria, and 1 event passed the type C selection criteria. This is summarized in Table 5.25.

These eight data events which pass the selection criteria could be background events, or they could be actual leptoquark events. The significance of the number of events in the data sample which pass the selection criteria is determined by comparison to the number of background events which are expected to pass the selection criteria. This is explained in Chapter 6.

## 5.8 Comparison of Simulated Data to OPAL Data

In this section, we show histograms of certain variables to illustrate that the simulated background processes are in agreement with the real data recorded by the OPAL detector. We also show histograms of variables for the simulated leptoquark signal events, to illustrate the motivation for certain selection criteria.

Figure 5.5 shows histograms of the visible energy (in GeV) after the pre-selection criteria have been applied, for both the 183 GeV data sample, and the total of the simulated background processes. The general shape is due to a quickly falling two-photon background. The peak near 100 GeV is due to radiative return to the  $Z^0$  mass. A photon is emitted by one of the initial state leptons prior to the electron-positron interaction, and the photon escapes undetected down the beam pipe. The effective centre-of-mass energy is then close to what is needed to produce a  $Z^0$  boson. The peak near 180 GeV corresponds to the centre-of-mass energy (183 GeV). Visible energies above the centre-of-mass energy are a result of double counting.

Figure 5.6 shows histograms of the cosine of the angle between the missing momentum and the  $z$ -axis, after the selection criterion A1 has been applied (for Topology A selection criteria), for both the 183 GeV data sample, and the total of the simulated background processes. Also shown is the same variable, for simulated first-generation  $90 \text{ GeV}/c^2$  leptoquark pair-production and subsequent decay via Topology A.

Figure 5.7 shows histograms of the missing transverse momentum, after the selection criterion A2 has been applied (for Topology A selection criteria), for both the 183 GeV data sample, and the total of the simulated background processes. Also

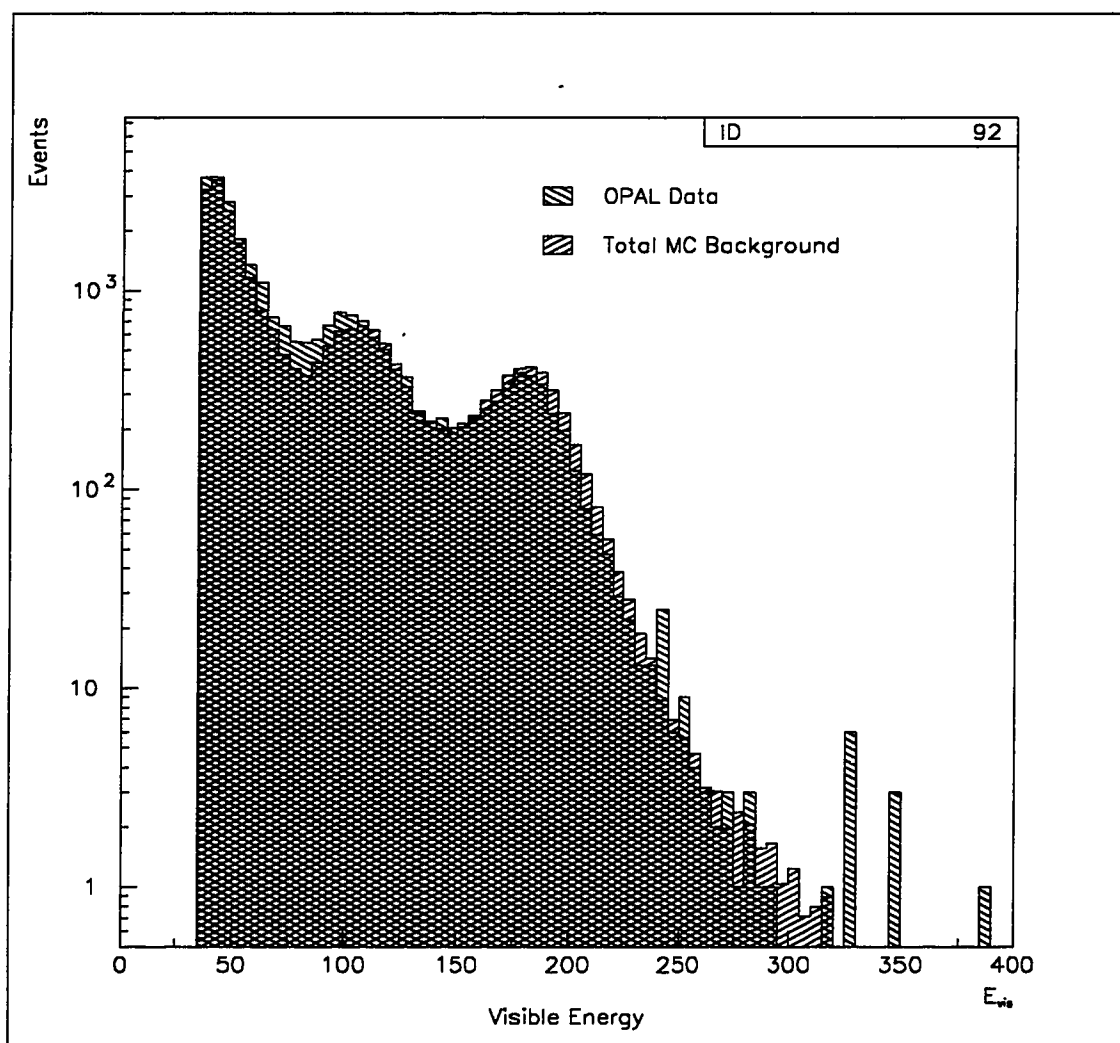


Figure 5.5: The visible energy after the preselection criteria have been applied, for both the 183 GeV data sample, and the total of the simulated background processes. (Energy is in GeV.)

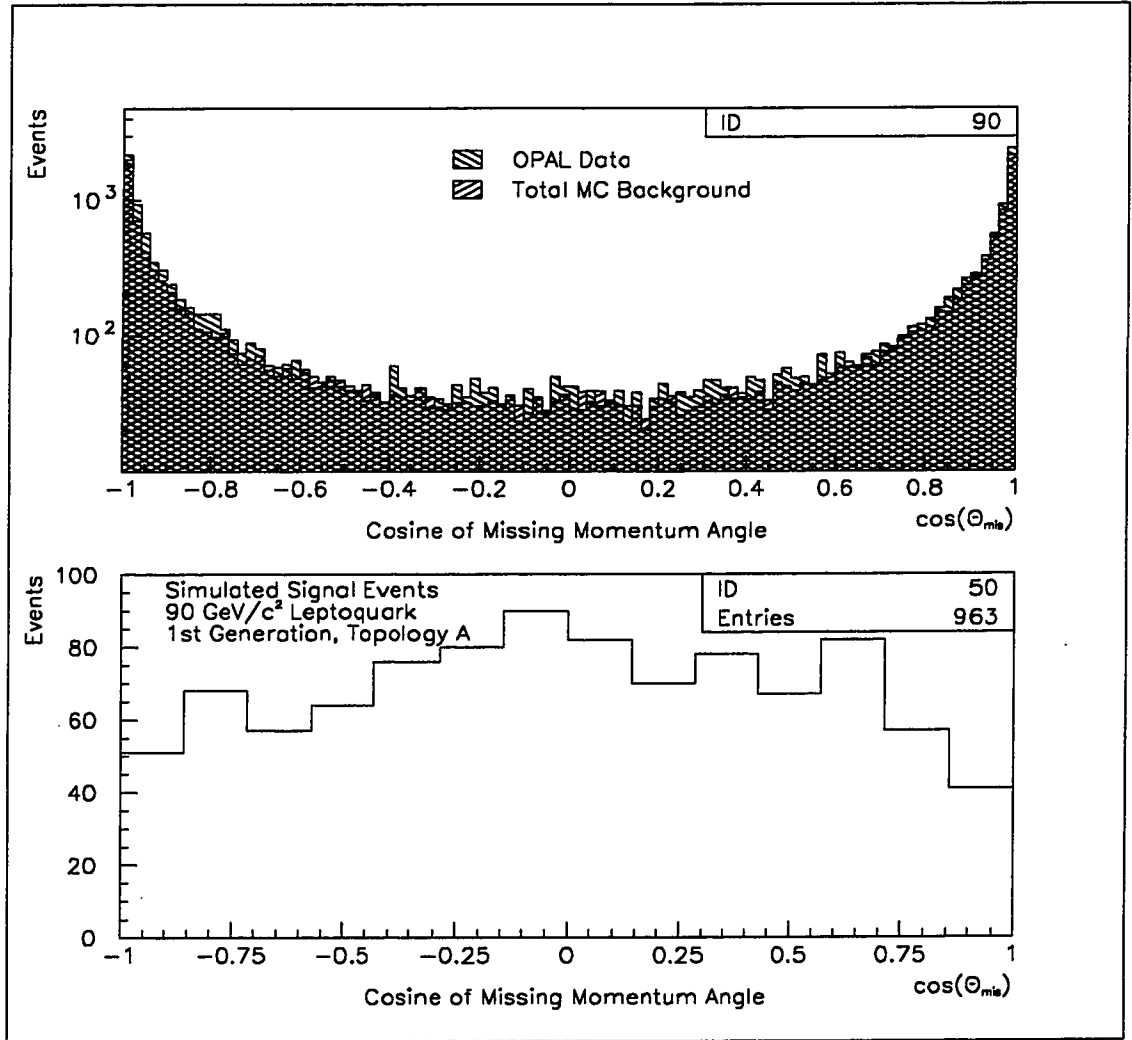


Figure 5.6: The cosine of the angle between the missing momentum and the  $z$ -axis, after the selection criterion A1 has been applied (for Topology A selection criteria), for both the 183 GeV data sample, and the total of the simulated background processes. Also shown is the same variable, for simulated first-generation 90 GeV/ $c^2$  leptoquark pair-production and subsequent decay via Topology A.

shown is the same variable, for simulated first-generation  $90 \text{ GeV}/c^2$  leptoquark pair-production and subsequent decay via Topology A.

Figure 5.8 shows histograms of the value of  $Y_{23}$  (the resolution parameter when reconstructing events into four jets using the Durham algorithm), after the selection criterion A3 has been applied (for Topology A selection criteria), for both the 183 GeV data sample, and the total of the simulated background processes. Also shown is the same variable, for simulated first-generation  $90 \text{ GeV}/c^2$  leptoquark pair-production and subsequent decay via Topology A.

Figure 5.9 shows histograms of the cosine of the angle between the missing momentum and the  $z$ -axis, after the selection criterion B1 has been applied (for Topology B selection criteria), for both the 183 GeV data sample, and the total of the simulated background processes. Also shown is the same variable, for simulated first-generation  $90 \text{ GeV}/c^2$  leptoquark pair-production and subsequent decay via Topology B.

Figure 5.10 shows histograms of  $R_{mis}$  (the ratio between missing momentum and  $\sqrt{s}$ ), after the selection criterion B2 has been applied (for Topology B selection criteria), for both the 183 GeV data sample, and the total of the simulated background processes. Also shown is the same variable, for simulated first-generation  $90 \text{ GeV}/c^2$  leptoquark pair-production and subsequent decay via Topology B.

Figure 5.11 shows histograms of the value of  $Y_{43}$  (the resolution parameter when reconstructing events into four jets using the Durham algorithm), after the selection criterion C1 has been applied (for Topology C selection criteria), for both the 183 GeV data sample, and the total of the simulated background processes. Also shown is the same variable, for simulated first-generation  $90 \text{ GeV}/c^2$  leptoquark pair-production and subsequent decay via Topology C.

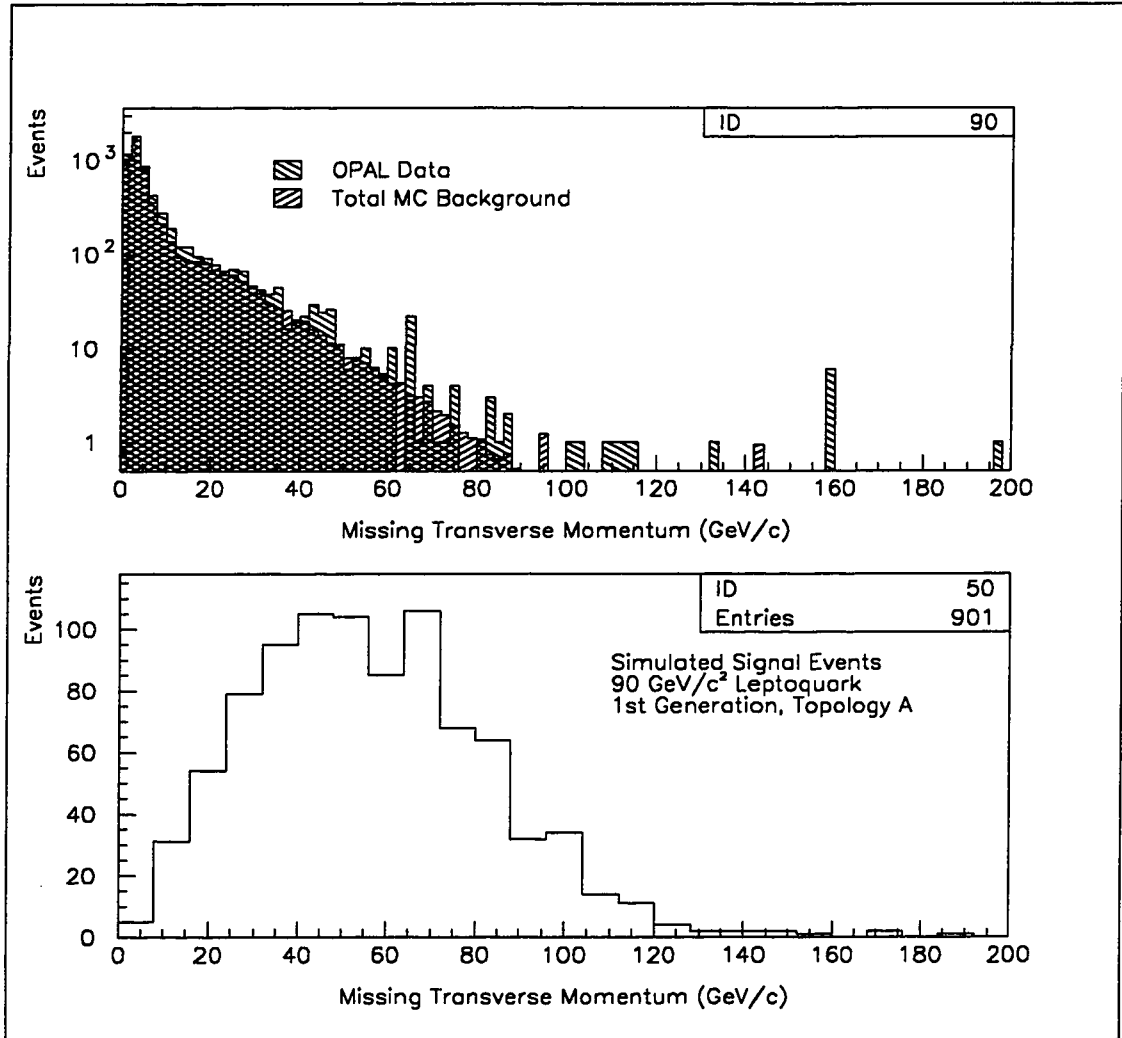


Figure 5.7: The amount of missing transverse momentum, after the selection criterion A2 has been applied (for Topology A selection criteria), for both the 183 GeV data sample, and the total of the simulated background processes. Also shown is the same variable, for simulated first-generation 90 GeV/c<sup>2</sup> leptoquark pair-production and subsequent decay via Topology A.

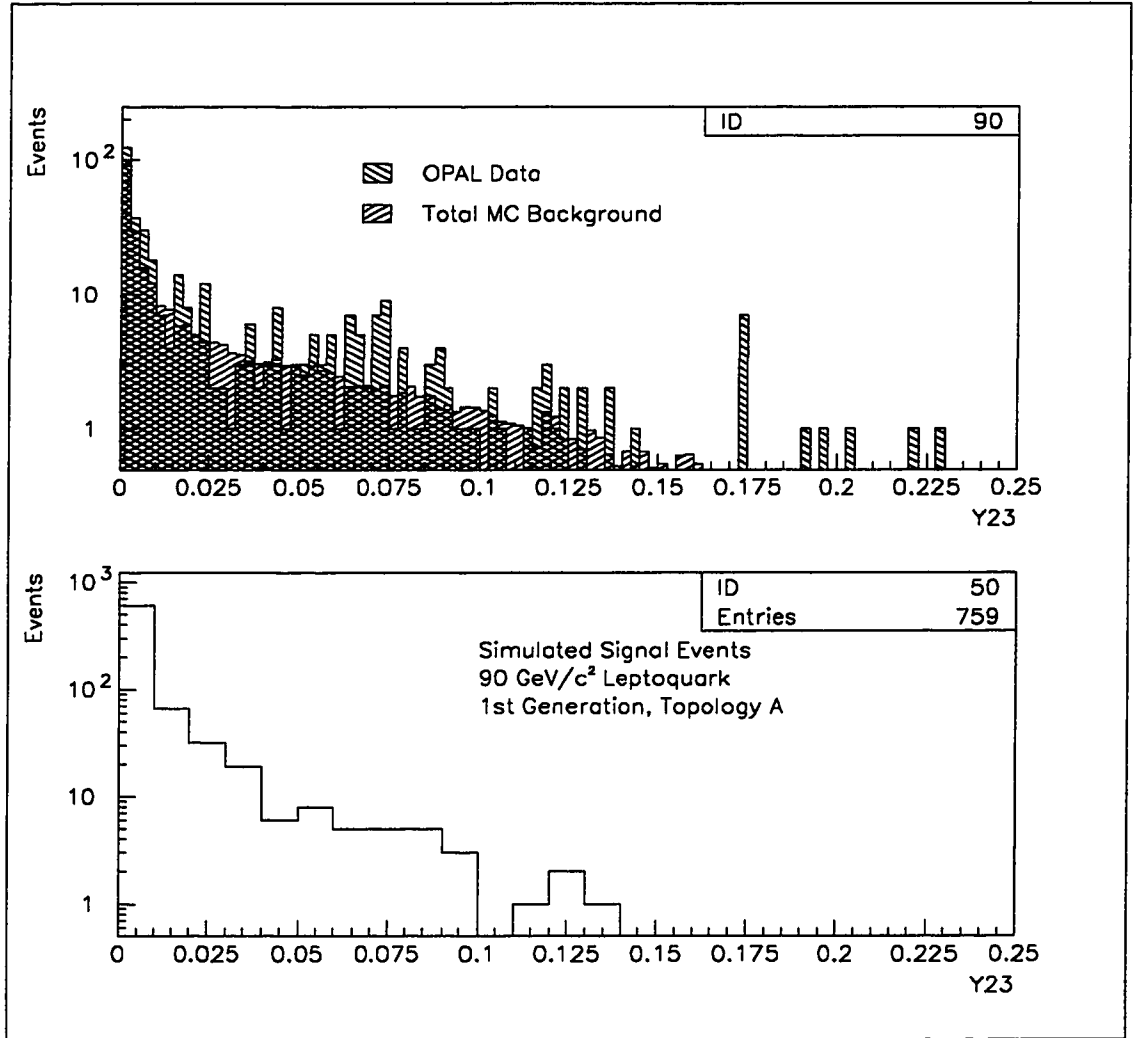


Figure 5.8: The value of  $Y_{23}$  (the resolution parameter when reconstructing events into four jets using the Durham algorithm), after the selection criterion A3 has been applied (for Topology A selection criteria), for both the 183 GeV data sample, and the total of the simulated background processes. Also shown is the same variable, for simulated first-generation 90 GeV/c<sup>2</sup> leptoquark pair-production and subsequent decay via Topology A.

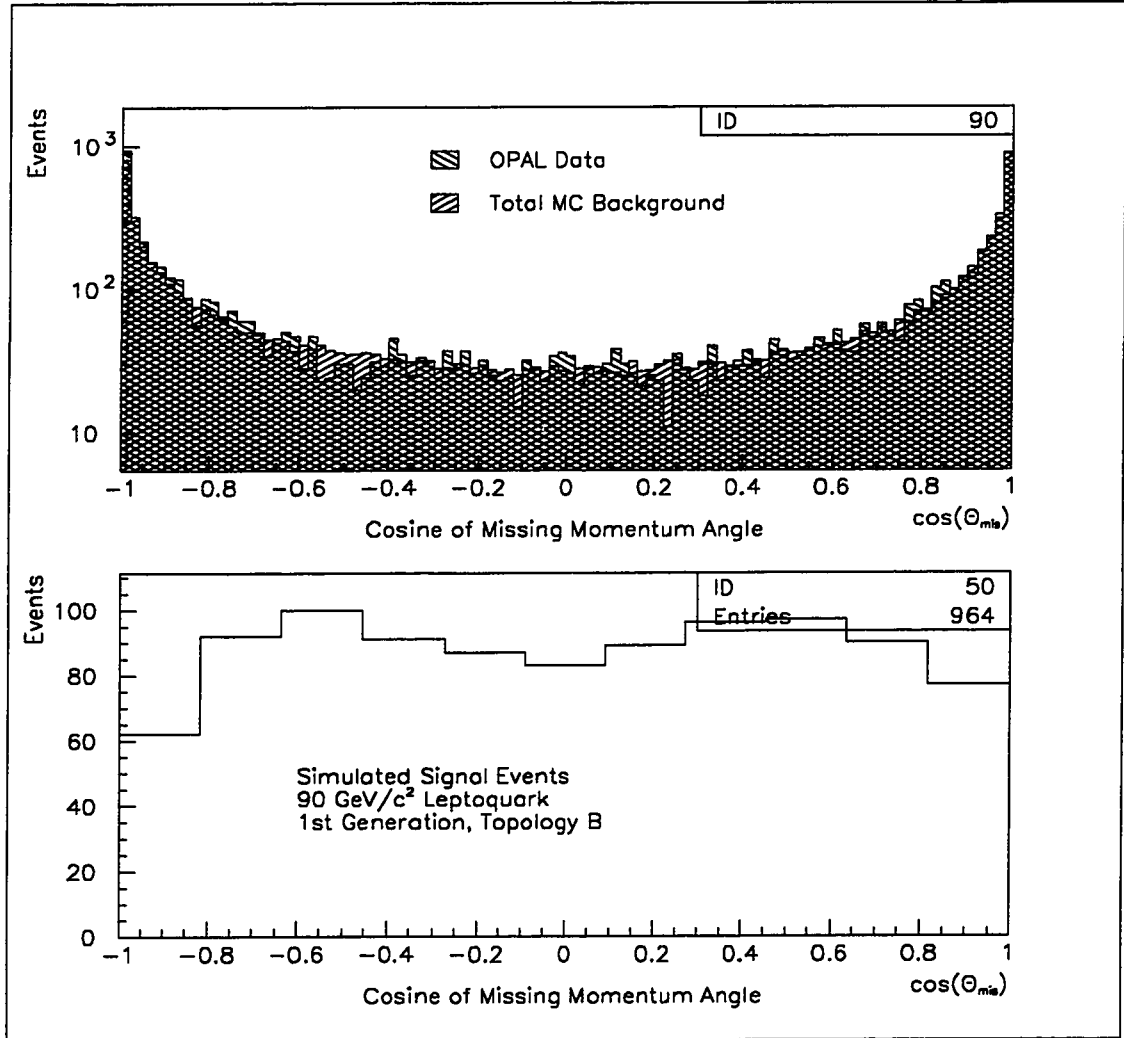


Figure 5.9: The cosine of the angle between the missing momentum and the  $z$ -axis, after the selection criterion B1 has been applied (for Topology B selection criteria), for both the 183 GeV data sample, and the total of the simulated background processes. Also shown is the same variable, for simulated first-generation 90 GeV/ $c^2$  leptoquark pair-production and subsequent decay via Topology B.

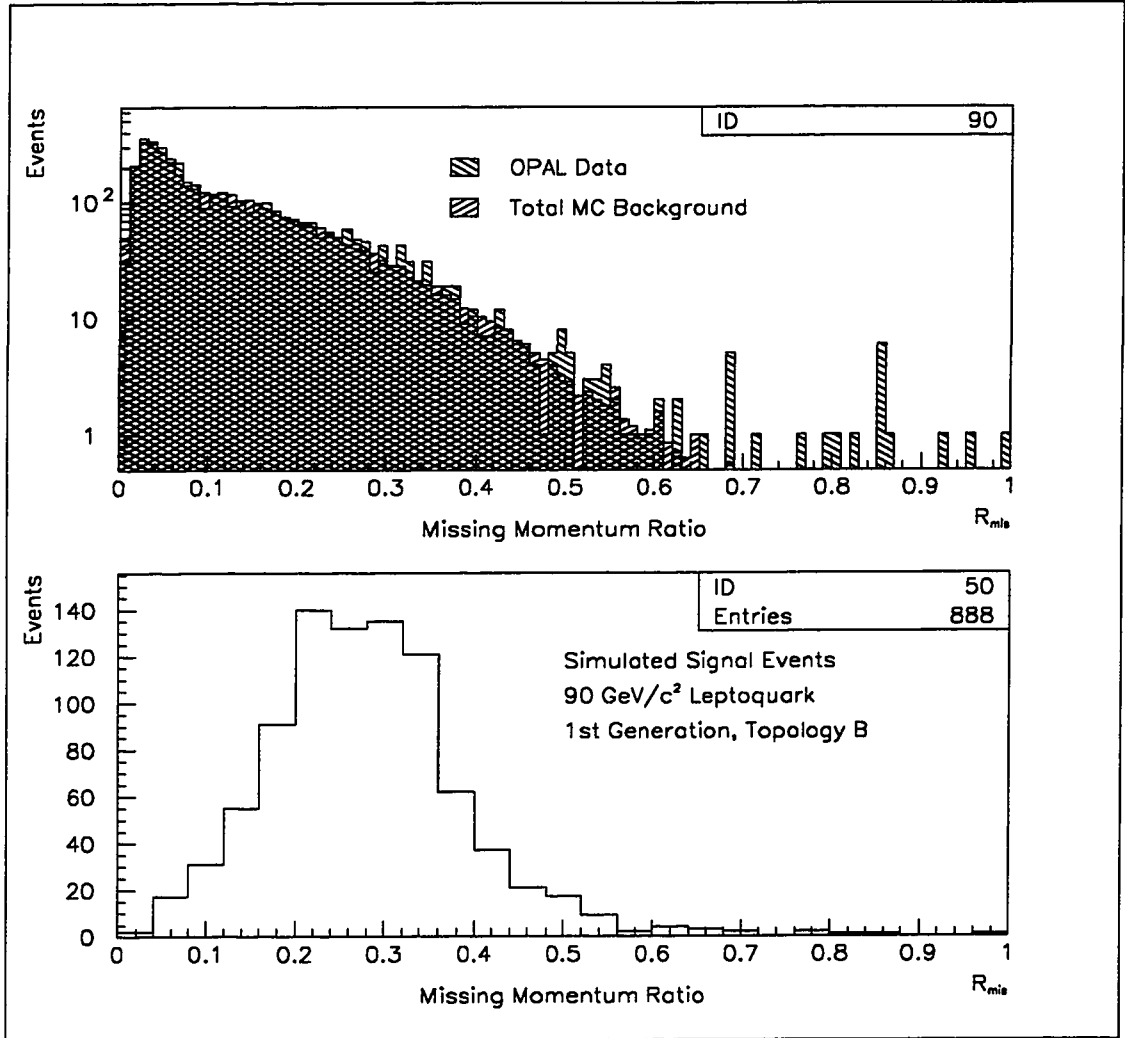


Figure 5.10: Histogram of  $R_{mis}$  (the ratio between missing momentum and  $\sqrt{s}$ ), after the selection criterion B2 has been applied (for Topology B selection criteria), for both the 183 GeV data sample, and the total of the simulated background processes. Also shown is the same variable, for simulated first-generation 90 GeV/c<sup>2</sup> leptoquark pair-production and subsequent decay via Topology B.

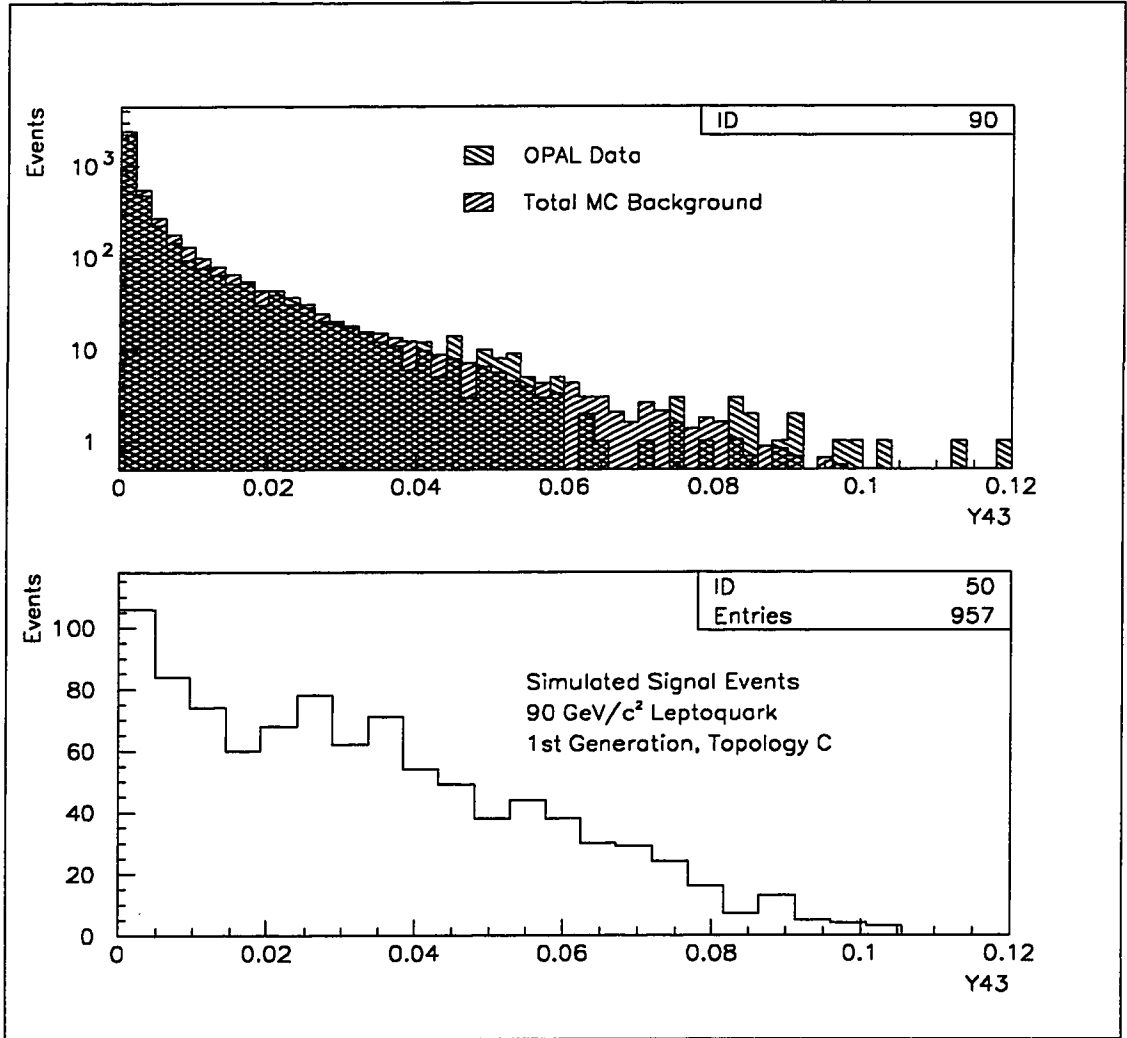


Figure 5.11: The value of  $Y_{43}$  (the resolution parameter when reconstructing events into four jets using the Durham algorithm), after the selection criterion C1 has been applied (for Topology C selection criteria), for both the 183 GeV data sample, and the total of the simulated background processes. Also shown is the same variable, for simulated first-generation 90 GeV/c<sup>2</sup> leptoquark pair-production and subsequent decay via Topology C.

Figure 5.12 shows histograms of the energy of the most energetic electron, after the selection criterion C3 has been applied (for Topology C selection criteria), for both the 183 GeV data sample, and the total of the simulated background processes. Also shown is the same variable, for simulated first-generation  $90 \text{ GeV}/c^2$  leptoquark pair-production and subsequent decay via Topology C.

Figure 5.13 shows histograms of the energy of the most energetic positron, after the selection criterion C3 has been applied (for Topology C selection criteria), for both the 183 GeV data sample, and the total of the simulated background processes. Also shown is the same variable, for simulated first-generation  $90 \text{ GeV}/c^2$  leptoquark pair-production and subsequent decay via Topology C.

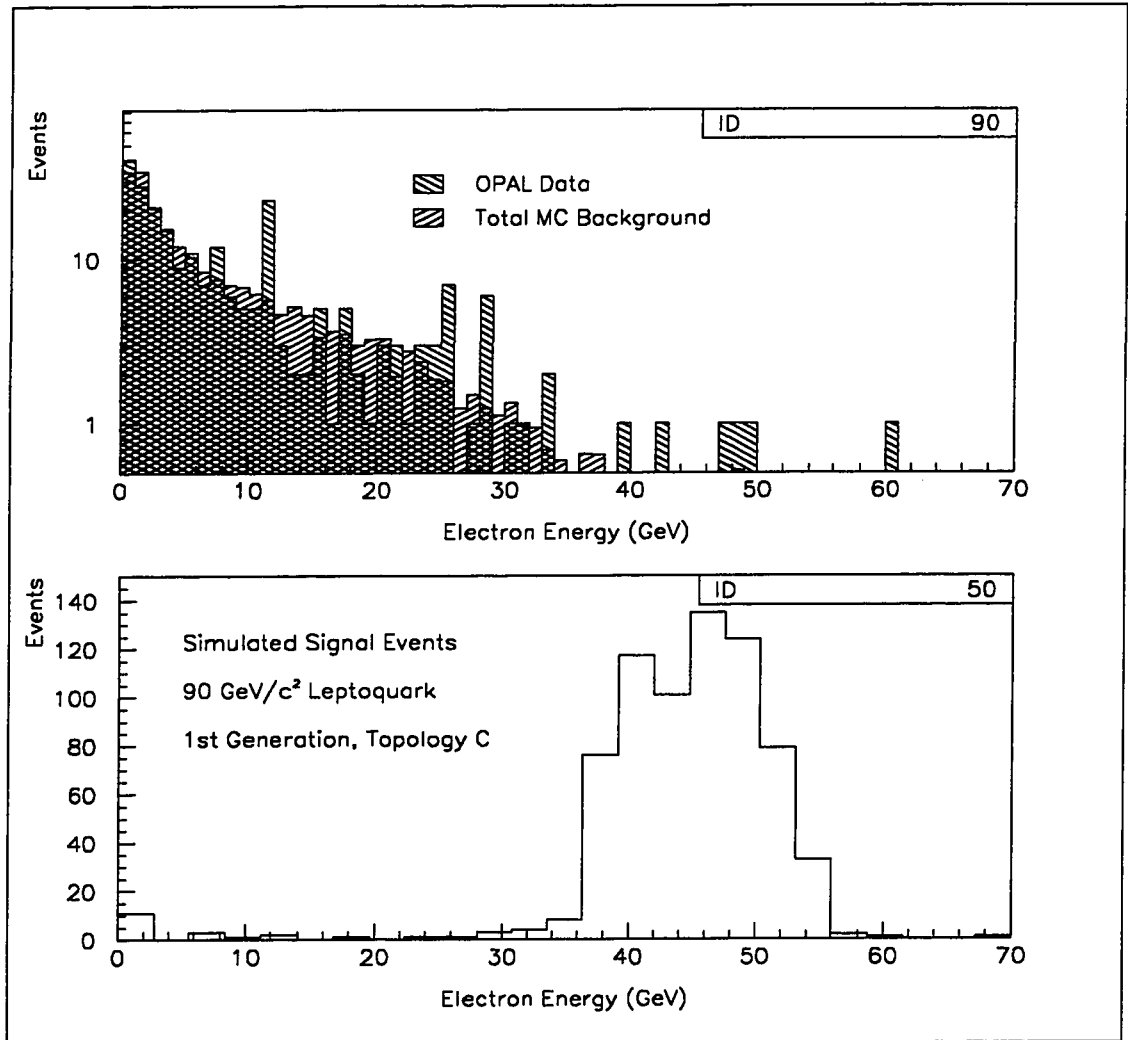


Figure 5.12: The energy of the most energetic electron, after the selection criterion C3 has been applied (for Topology C selection criteria), for both the 183 GeV data sample, and the total of the simulated background processes. Also shown is the same variable, for simulated first-generation 90 GeV/c<sup>2</sup> leptoquark pair-production and decay via Topology C.

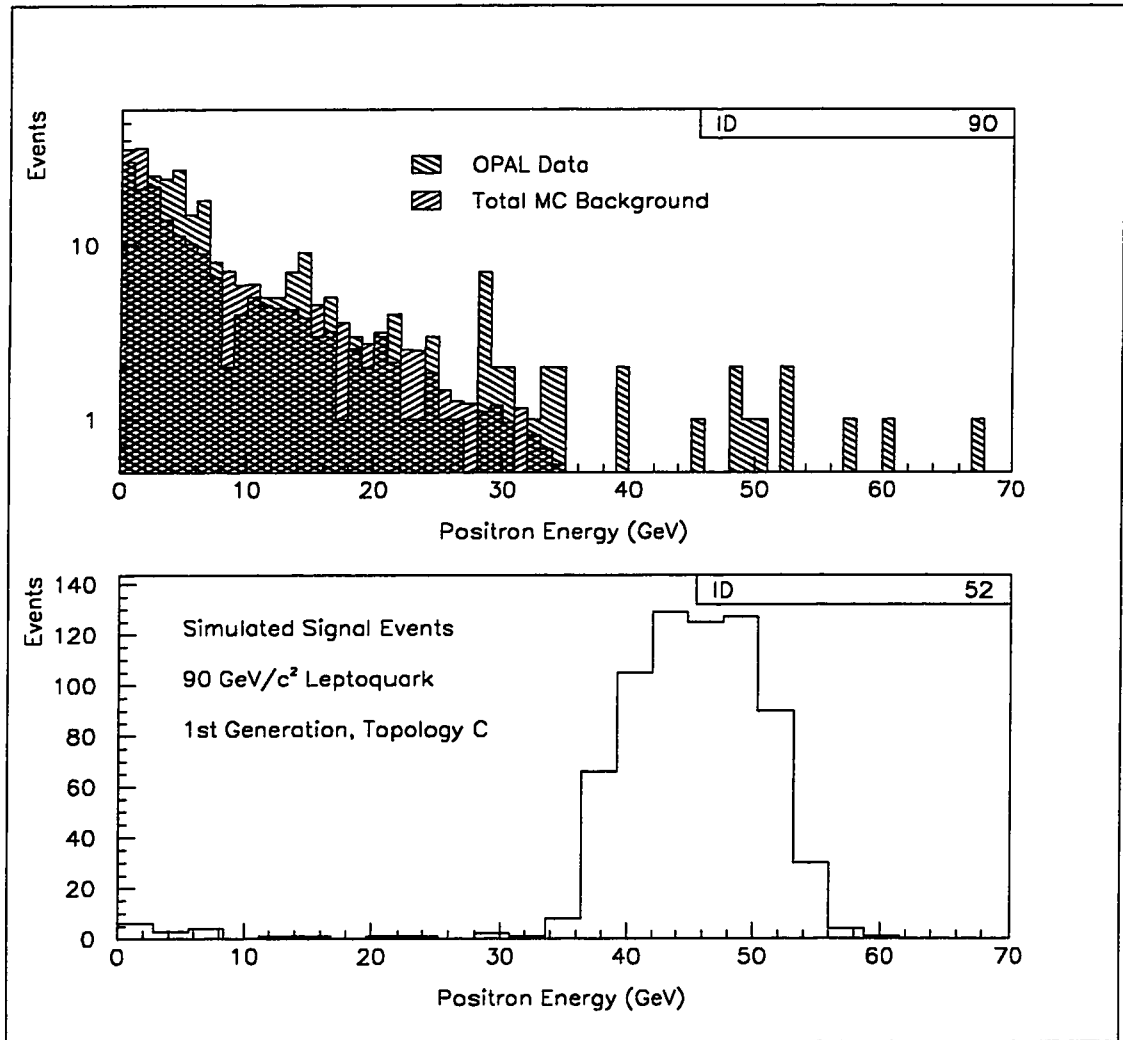


Figure 5.13: The energy of the most energetic positron, after the selection criterion C3 has been applied (for Topology C selection criteria), for both the 183 GeV data sample, and the total of the simulated background processes. Also shown is the same variable, for simulated first-generation 90 GeV/ $c^2$  leptoquark pair-production and decay via Topology C.

## CHAPTER 6

### Limits on Vector Leptoquark Production

This chapter uses all of the information from the previous chapter to obtain several results. The information that we have obtained from our simulations concerning the effects of the cuts on the background processes (background rejection) and on the signal processes (signal efficiency) is combined with the results of the search through real data.

In the previous chapter, it was shown that for  $55.9 \text{ pb}^{-1}$  of data, the number of expected background events are as follows: when searching for Topology A, the expected number of background events surviving the selection criteria is  $3.03^{+1.45}_{-0.61}$  events; for Topology B it is  $3.38^{+1.24}_{-0.59}$  events; and for Topology C it is  $2.32^{+1.11}_{-0.32}$  events.

Also, recall from the previous chapter that after applying the three sets of selection criteria to the  $55.9 \text{ pb}^{-1}$  data sample recorded by OPAL at a centre-of-mass energy of 183 GeV, the number of events surviving the selection criteria is 4 for Topology A, 3 for Topology B, and 1 for Topology C.

These results are summarized in Table 6.1. Looking at the values in this table, it is clear that the number of leptoquark candidate events in the data sample is not significantly greater than the number of background events expected from Standard Model processes, for all three decay topologies. At this point, we conclude that there is no evidence of vector leptoquarks in the data sample.

<i>Topology</i>	Type A	Type B	Type C
<i>Expected Background</i>	$3.03^{+1.45}_{-0.61}$	$3.38^{+1.24}_{-0.59}$	$2.32^{+1.11}_{-0.32}$
<i>Observed in Data</i>	4	3	1

Table 6.1: Expected number of background events to pass the selection criteria for  $55.9 \text{ pb}^{-1}$  of data, and actual number of data events in  $55.9 \text{ pb}^{-1}$  of data which pass the selection criteria, for all three topologies.

## 6.1 Determination of Upper Limits on the Leptoquark Production Cross-Section

Since vector leptoquarks were not discovered in the energy region of the data sample, the next step is to determine upper limits on the cross-sections for vector leptoquark pair-production. These values can be used to determine lower limits on the leptoquark mass.

We use a likelihood approach to determine upper limits at the 95% confidence level on the cross-section for the pair-production of vector leptoquarks. The signal efficiencies, and the number of expected background events are included, along with their uncertainties. The fact that three decay topologies are available is also considered in determining upper limits.

Using the Bayesian approach, for a confidence level  $CL = 1 - \epsilon$  and an observation  $n$ , the upper limit  $\sigma$  on the parameter  $s$ , for the process with probability density function  $W(n; s)$  is

$$\epsilon = \frac{\int_{\sigma}^{\infty} W(n; s) ds}{\int_0^{\infty} W(n; s) ds}. \quad (6.6.1.1)$$

Assuming a Poisson distribution for the total number of signal events and a multinomial distribution for the branching fraction into the different decay channels,

we get the joint probability density function for the total number of events in each decay channel as a product of independent Poisson distributions [55].

For a known fraction of signal events  $p_i$  and known average background  $b_i$ , in decay channel  $i$ ,

$$W(n_i, b_i; \sigma, \beta) = \prod_{i=1}^3 P(n_i; \sigma L p_i \eta_i + b_i), \quad (6.6.1.2)$$

where

- $n_i$  = number of observed events in the data for decay channel  $i$ :  
 $n_1 = 4, n_2 = 3, n_3 = 1,$
- $b_i$  = number of estimated background events for decay channel  $i$ :  
 $b_1 = 3.03, b_2 = 3.38, b_3 = 2.32,$
- $\eta_i$  = detection efficiency for decay channel  $i$ ,
- $p_i$  = branching fraction for decay channel  $i$ :  
 $p_1 = (1 - \beta)^2, p_2 = 2(1 - \beta)\beta, p_3 = \beta^2,$
- $L$  = integrated luminosity,
- $\sigma$  = production cross-section.

Substituting the Poisson probability density function for the expression for  $P$  and integrating gives

$$\epsilon = \prod_{i=1}^3 \sum_{j=0}^{n_i} \frac{e^{-(\sigma L p_i \eta_i + b_i)} (\sigma L p_i \eta_i + b_i)^j}{j!} / \prod_{i=1}^3 \sum_{j=0}^{n_i} \frac{e^{-b_i} b_i^j}{j!}. \quad (6.6.1.3)$$

The uncertainties in the means  $b_i$  [56] and efficiencies  $\eta_i$  [57] can be included by convolution

$$\begin{aligned} \epsilon &= \int_0^\infty \int_0^\infty \prod_{i=1}^3 db'_i d\eta'_i g(b_i, b'_i) g(\eta_i, \eta'_i) \sum_{j=0}^{n_i} \frac{e^{-(\sigma L p_i \eta'_i + b'_i)} (\sigma L p_i \eta'_i + b'_i)^j}{j!} \\ &/ \int_0^\infty \int_0^\infty \prod_{i=1}^3 db'_i d\eta'_i g(b_i, b'_i) g(\eta_i, \eta'_i) \sum_{j=0}^{n_i} \frac{e^{-b'_i} b'^j_i}{j!}, \end{aligned} \quad (6.6.1.4)$$

where  $g(b_i, b'_i)$  and  $g(\eta_i, \eta'_i)$  are the resolution functions given by

$$g(b_i, b'_i) \simeq e^{-(b_i - b'_i)^2 / 2\sigma_{b_i}^2} \quad (6.6.1.5)$$

$$g(\eta_i, \eta'_i) \simeq e^{-(\eta_i - \eta'_i)^2 / 2\sigma_{\eta_i}^2}, \quad (6.6.1.6)$$

where  $\sigma_{b_i}$  is the error in the number of background events (taken to be the larger of the two Poisson errors determined in Section 5.6, for each topology  $i$ ) and  $\sigma_{\eta_i}$  is the error in the efficiency.  $\sigma_{b_i}$  and  $\sigma_{\eta_i}$  include statistical and systematic uncertainties.

One can solve Equation 6.6.1.4 for  $\sigma$  to obtain the desired  $\epsilon$ , for any values of  $b_i$  and  $\eta_i$ .

## 6.2 Determination of Leptoquark Mass Limits

We then compare the upper limits on the cross-sections to the theoretical leptoquark cross-sections, which were calculated using Equation 2.2.5.25. These theoretical cross-sections have been computed for all nine vector leptoquark states, for masses from 50 GeV/c<sup>2</sup> to 90 GeV/c<sup>2</sup> in steps of 5 GeV/c<sup>2</sup>. Because we have determined the upper limit on the cross-section for vector leptoquark production, we can place lower limits on the mass of each vector leptoquark species. However, uncertainties in the theory are not taken into account when determining mass limits.

For each leptoquark, the value of  $\beta$  depends on the magnitude of the couplings. So in general,  $\beta$  can vary from 0 to 1. However, for many leptoquarks, only certain couplings are allowed, based on the theory. This affects the possibilities for  $\beta$ . Of the nine vector leptoquarks, one leptoquark has a value of  $\beta$  which can vary from 0 to 1 ( $^{1/3}V_2$ ), one leptoquark has a value of  $\beta$  which can vary from 0.5 to 1 ( $^{2/3}U_1$ ), four leptoquarks have  $\beta = 1$  ( $^{4/3}V_2$ ,  $^{1/3}\tilde{V}_2$ ,  $^{5/3}\tilde{U}_1$  and  $^{5/3}U_3$ ), one leptoquark

<i>Vector LQ</i>	$\beta$
$^{4/3}V_2$	1
$^{1/3}V_2$	0 to 1
$^{1/3}\tilde{V}_2$	1
$^{-2/3}\tilde{V}_2$	0
$^{2/3}U_1$	0.5 to 1
$^{5/3}\tilde{U}_1$	1
$^{5/3}U_3$	1
$^{2/3}U_3$	0.5
$^{-1/3}U_3$	0

Table 6.2: Allowed value(s) of  $\beta$  for each vector leptoquark.

has  $\beta = 0.5$  ( $^{2/3}U_3$ ), and two leptoquarks have  $\beta = 0$  ( $^{-2/3}\tilde{V}_2$  and  $^{-1/3}U_3$ ).<sup>1</sup> This is summarized in Table 6.2.

For values of  $\beta$  of 0.0, 0.5 and 1.0, we have produced graphs showing the upper limits on the production cross-section at the 95% confidence level, as a function of the leptoquark mass. Also on these graphs, we show the theoretical cross-sections for those leptoquarks which correspond to the value of  $\beta$ . The intersection of these two lines gives the lower limit on the leptoquark mass, at the 95% confidence level. In cases where the value of  $\beta$  is not fixed, the lower limit on the leptoquark mass is determined in this manner for various  $\beta$ , and a plot of  $\beta$  versus leptoquark mass lower limit is shown. In all cases, the results are shown for both first- and second-generation vector leptoquarks.

---

<sup>1</sup>Note: the subscript  $\mu$  has been dropped from the vector leptoquark notation.

### 6.2.1 Vector Leptoquarks Which Have a Fixed Value of $\beta$

There are seven leptoquarks which have a fixed value of  $\beta$ .

Two leptoquarks have  $\beta = 0$  ( $^{-2/3}\tilde{V}_2$  and  $^{-1/3}U_3$ ). Figure 6.1 shows the upper limit on the cross-section at the 95% confidence level as a function of mass, for vector leptoquarks with  $\beta = 0$ , for both first- and second-generation leptoquarks. Also shown is the theoretical cross-section for these two vector leptoquarks. (Line 1 corresponds to  $^{-2/3}\tilde{V}_2$ , and line 2 corresponds to  $^{-1/3}U_3$ .) The lower limit on the mass is the intersection point in each case. For the leptoquark  $^{-2/3}\tilde{V}_2$ , the limit is 86 GeV/c<sup>2</sup> for both first- and second-generation, and for the leptoquark  $^{-1/3}U_3$ , the limit is 89 GeV/c<sup>2</sup> for both first- and second-generation.

One leptoquark has  $\beta = 0.5$  ( $^{2/3}U_3$ ). Figure 6.2 shows the upper limit on the cross-section at the 95% confidence level as a function of mass, for vector leptoquarks with  $\beta = 0.5$ , for both first- and second-generation leptoquarks. Also shown is the theoretical cross-section for this vector leptoquarks. (Line 1 corresponds to  $^{2/3}U_3$ .) The lower limit on the mass is the intersection point. For first-generation  $^{2/3}U_3$  leptoquarks, the limit is 84 GeV/c<sup>2</sup>, and for second-generation  $^{2/3}U_3$  leptoquarks, the limit is 85 GeV/c<sup>2</sup>.

Four leptoquarks have  $\beta = 1$  ( $^{4/3}V_2$ ,  $^{1/3}\tilde{V}_2$ ,  $^{5/3}\tilde{U}_1$  and  $^{5/3}U_3$ ). Figure 6.3 shows the upper limit on the cross-section at the 95% confidence level as a function of mass, for vector leptoquarks with  $\beta = 1.0$ , for both first- and second-generation leptoquarks. It was necessary to extrapolate slightly beyond 90 GeV/c<sup>2</sup>. Also shown is the theoretical cross-section for these four vector leptoquarks. (Line 1 corresponds to  $^{1/3}\tilde{V}_2$ , line 2 corresponds to  $^{4/3}V_2$ , line 3 corresponds to  $^{5/3}\tilde{U}_1$  and line 4 corresponds to  $^{5/3}U_3$ .) The lower limit on the mass is the intersection point in each case. For the leptoquark  $^{1/3}\tilde{V}_2$ , the limit is 89 GeV/c<sup>2</sup> for both first- and second-generation.

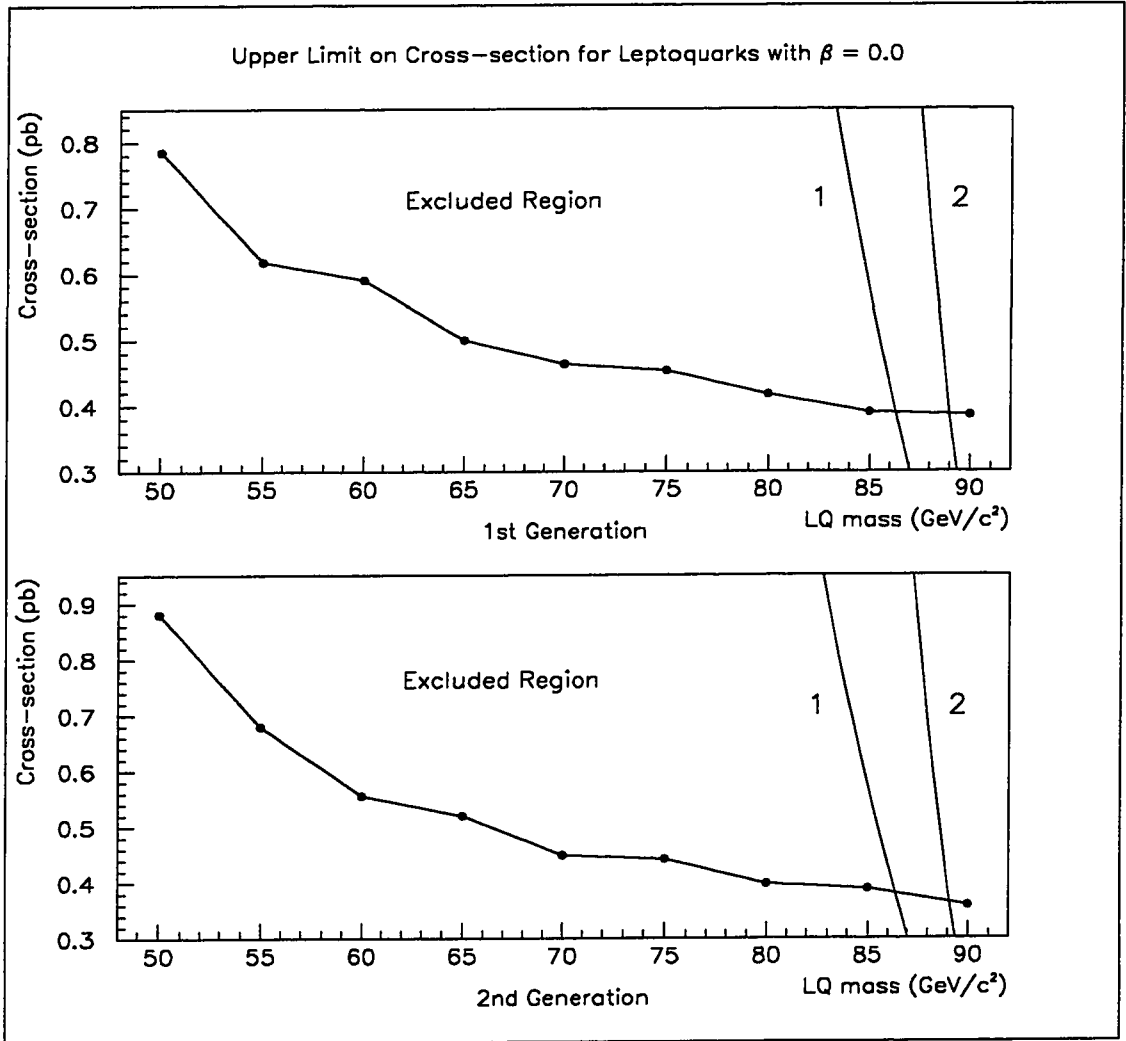


Figure 6.1: Upper limit on the cross-section at the 95% confidence level as a function of leptoquark mass, for  $\beta = 0$ . Also shown are the theoretical cross-sections for the leptoquarks (1)  $^{-2/3}\tilde{V}_2$  and (2)  $^{-1/3}U_3$ .

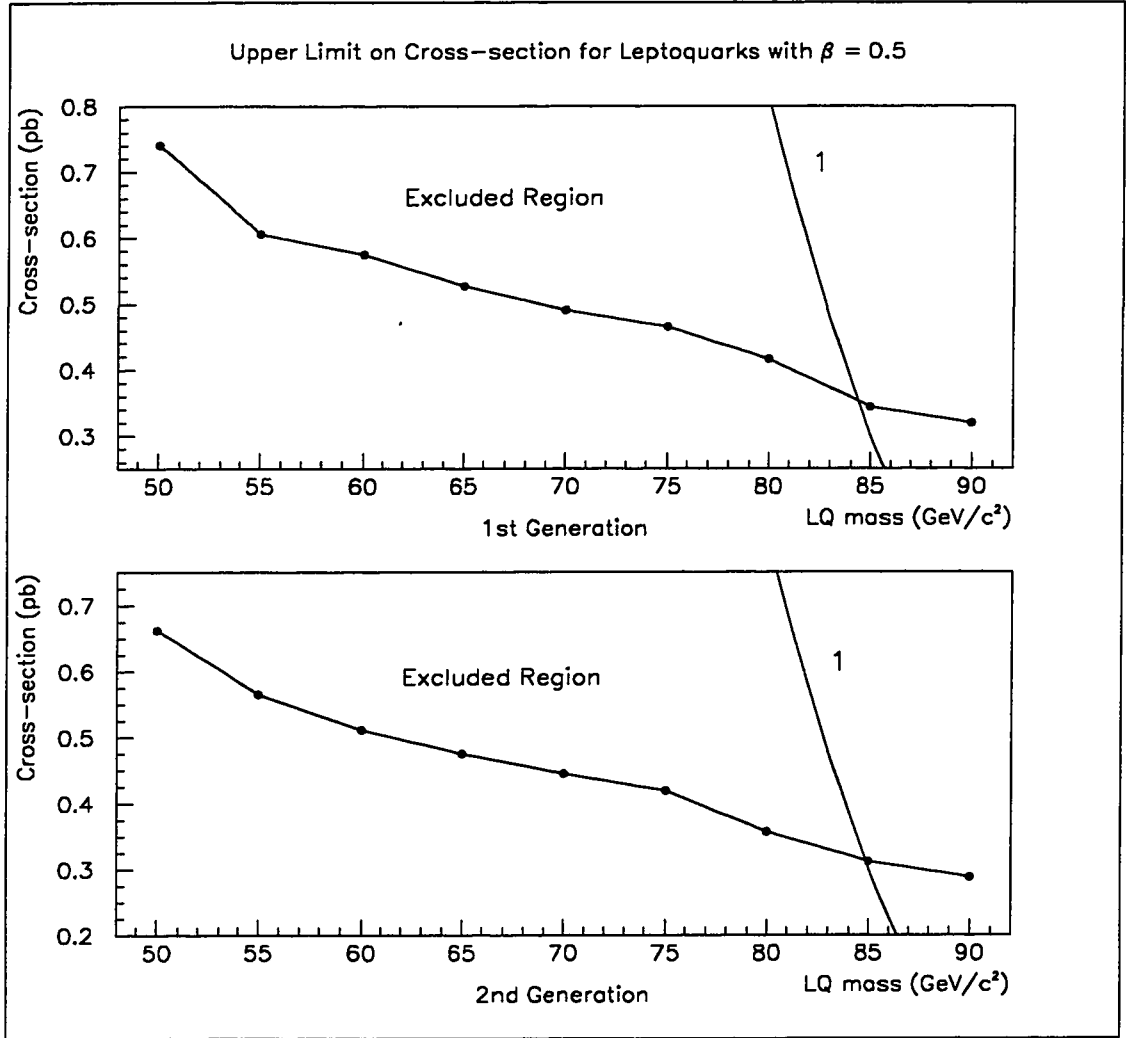


Figure 6.2: Upper limit on the cross-section at the 95% confidence level as a function of leptoquark mass, for  $\beta = 0.5$ . Also shown is the theoretical cross-section for the leptoquark  $(1) {}^{2/3}U_3$ .

<i>Vector Leptoquark</i>	<i>1st Generation Lower Limit (GeV/c<sup>2</sup>)</i>	<i>2nd Generation Lower Limit (GeV/c<sup>2</sup>)</i>
$^{4/3}V_2$	90	90
$^{1/3}\tilde{V}_2$	89	89
$^{-2/3}\tilde{V}_2$	86	86
$^{5/3}\tilde{U}_1$	90	90
$^{5/3}U_3$	90	90
$^{2/3}U_3$	84	85
$^{-1/3}U_3$	89	89

Table 6.3: Lower limits on the mass of those vector leptoquarks which have a fixed value of  $\beta$ , for both first- and second-generation, at the 95% confidence level.

For the vector leptoquarks  $^{4/3}V_2$ ,  $^{5/3}\tilde{U}_1$  and  $^{5/3}U_3$ , the limit is 90 GeV/c<sup>2</sup> for both first- and second generation.

For the seven vector leptoquarks which have a fixed value of  $\beta$ , the lower limits on the leptoquark mass are summarized in Table 6.3.

It is clear from all of these plots of expected number of signal events versus leptoquark mass that a small change in the upper limits on the cross-sections would give a negligible change in the lower limit obtained on the leptoquark mass.

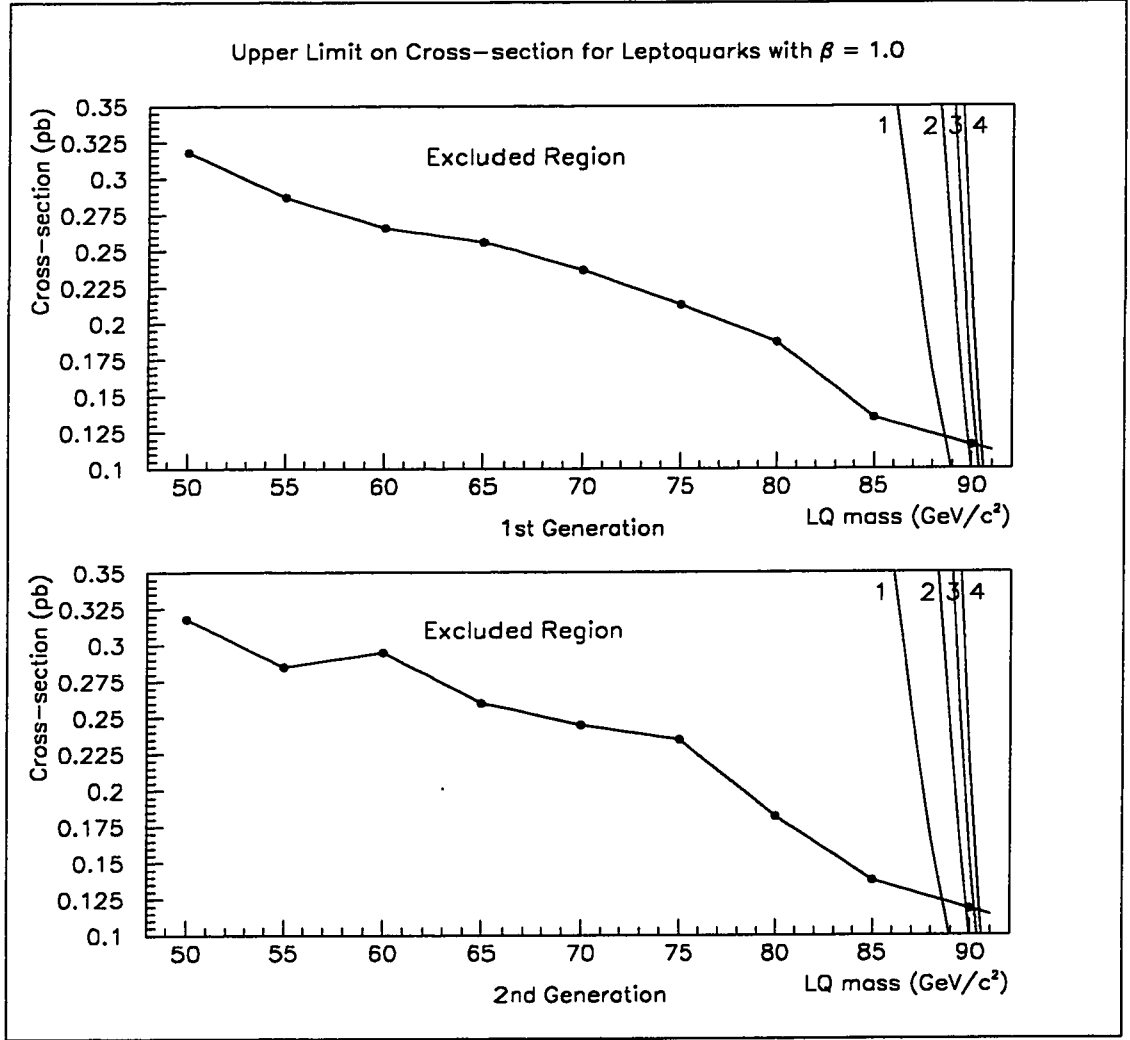


Figure 6.3: Upper limit on the cross-section at the 95% confidence level as a function of leptoquark mass, for  $\beta = 1.0$ . Also shown are the theoretical cross-sections for the leptoquarks (1)  $^{1/3}\tilde{V}_2$ , (2)  $^{4/3}\tilde{V}_2$ , (3)  $^{5/3}\tilde{U}_1$  and (4)  $^{5/3}U_3$ .

### 6.2.2 Vector Leptoquarks Which Do Not Have a Fixed Value of $\beta$

There are two vector leptoquarks which do not have a fixed value of  $\beta$ . In each case, we show plots of upper limit on the cross-section at the 95% confidence level versus leptoquark mass, for various allowed values of  $\beta$ . Also shown is the theoretical cross-section, and hence we determine lower limits in the leptoquark mass as a function of  $\beta$ , from the points of intersection of the theoretical cross-section with the upper limit contours.

The vector leptoquark  $^{1/3}V_2$  has a value of  $\beta$  which can vary from 0 to 1. Figure 6.4 shows the upper limit on the cross-section at the 95% confidence level as a function of mass, for various values of  $\beta$ , for both first- and second-generation leptoquarks. The theoretical cross-section for  $^{1/3}V_2$  is also shown.

The mass limits are then presented as a function of  $\beta$ . Figure 6.5 shows a plot of  $\beta$  versus leptoquark mass lower limit at the 95% confidence level, for both first- and second-generation  $^{1/3}V_2$  leptoquarks. The mass limits are greater than 87 GeV/c<sup>2</sup>, over the allowed range of  $\beta$  (0.0 to 1.0).

The vector leptoquark  $^{2/3}U_1$  has a value of  $\beta$  which can vary from 0.5 to 1. Figure 6.6 shows the upper limit on the cross-section at the 95% confidence level as a function of mass, for various values of  $\beta$ , for both first- and second-generation leptoquarks. The theoretical cross-section for  $^{2/3}U_1$  is also shown.

Figure 6.7 shows a plot of  $\beta$  versus leptoquark mass lower limit at the 95% confidence level, for both first- and second-generation  $^{2/3}U_1$  leptoquarks. The mass limits are greater than 84 GeV/c<sup>2</sup>, over the allowed range of  $\beta$  (0.5 to 1.0).

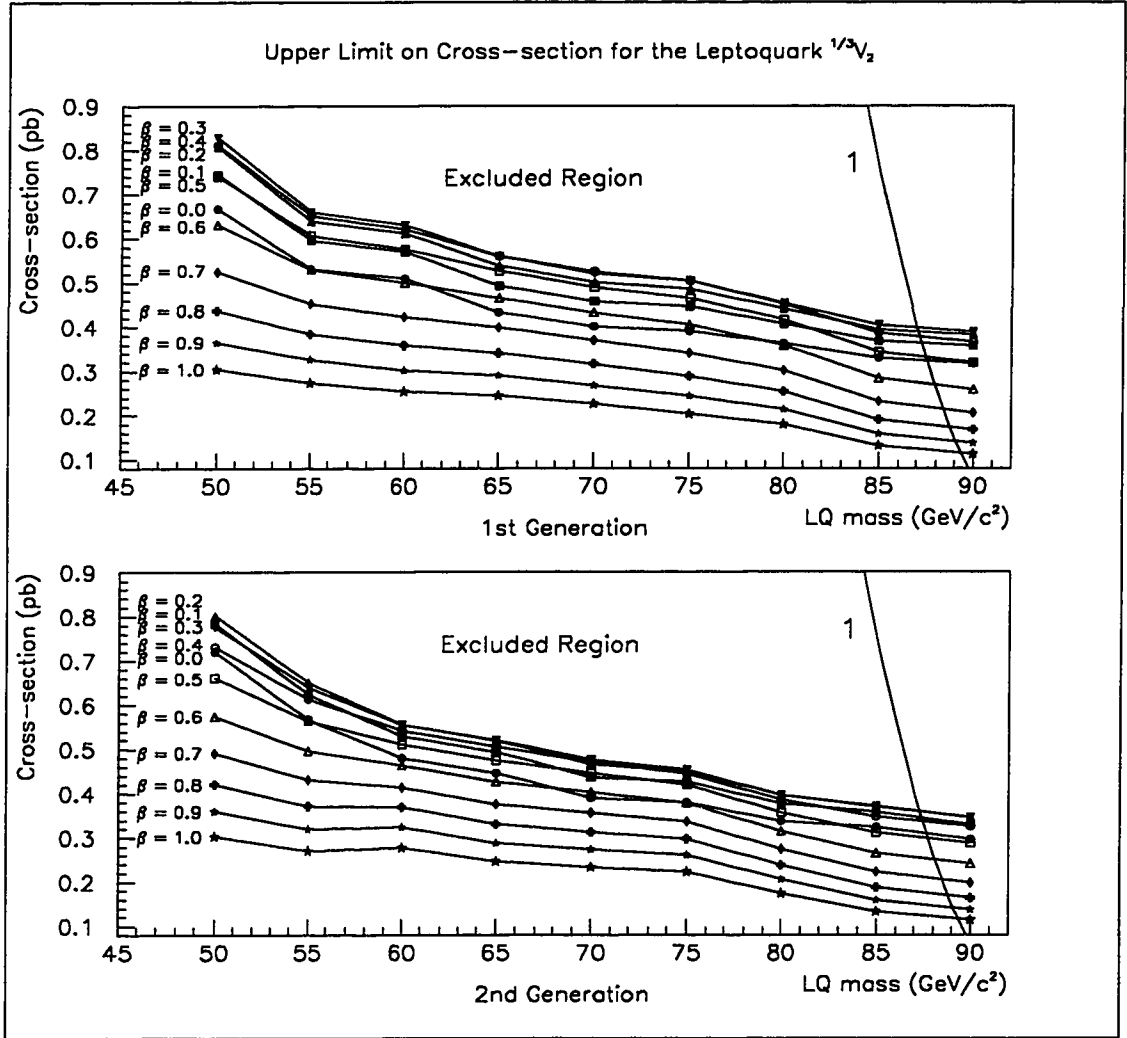


Figure 6.4: The upper limit on the cross-section at the 95% confidence level as a function of mass, for various values of  $\beta$ , for both first- and second-generation leptoquarks. Also shown is the theoretical cross-section for the leptoquark (1)  $^{1/3}V_2$ .

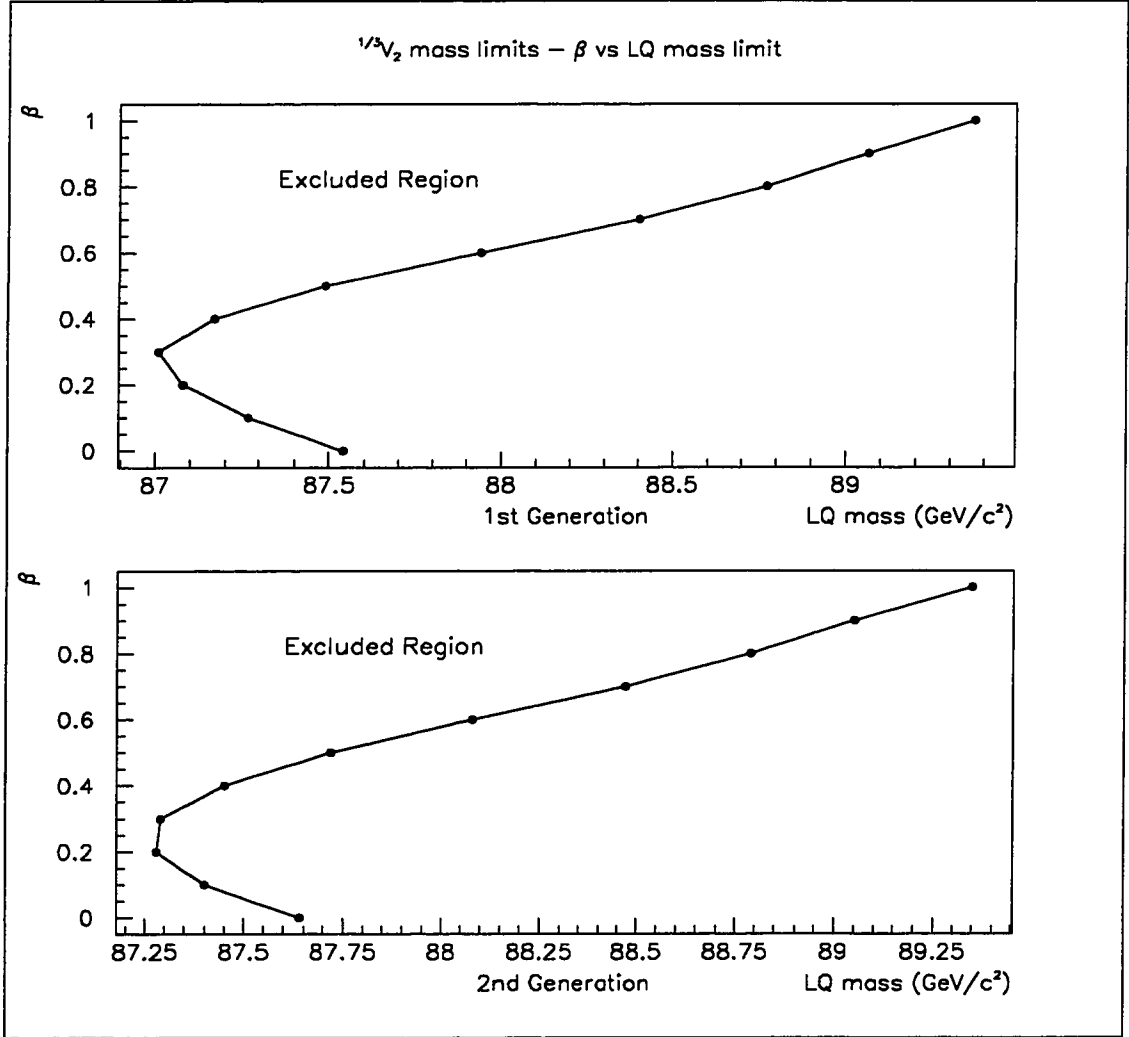


Figure 6.5:  $\beta$  versus lower limit on the mass of the vector leptoquark  $^{1/3}V_2$ , for both first- and second-generation at the 95% confidence level.

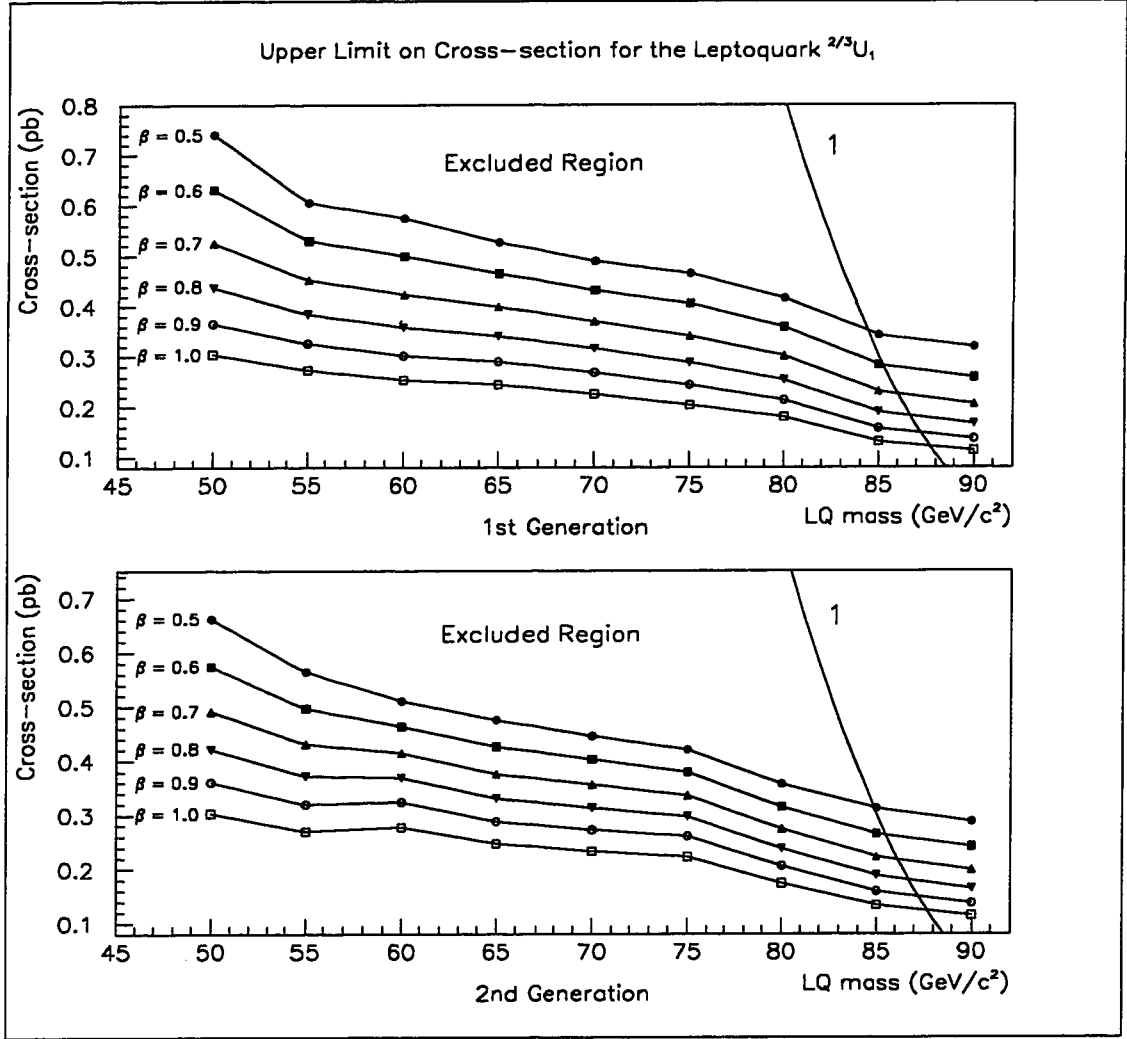


Figure 6.6: The upper limit on the cross-section at the 95% confidence level as a function of mass, for various values of  $\beta$ , for both first- and second-generation leptoquarks. Also shown is the theoretical cross-section for the leptoquark (1)  ${}^{2/3}U_1$ .

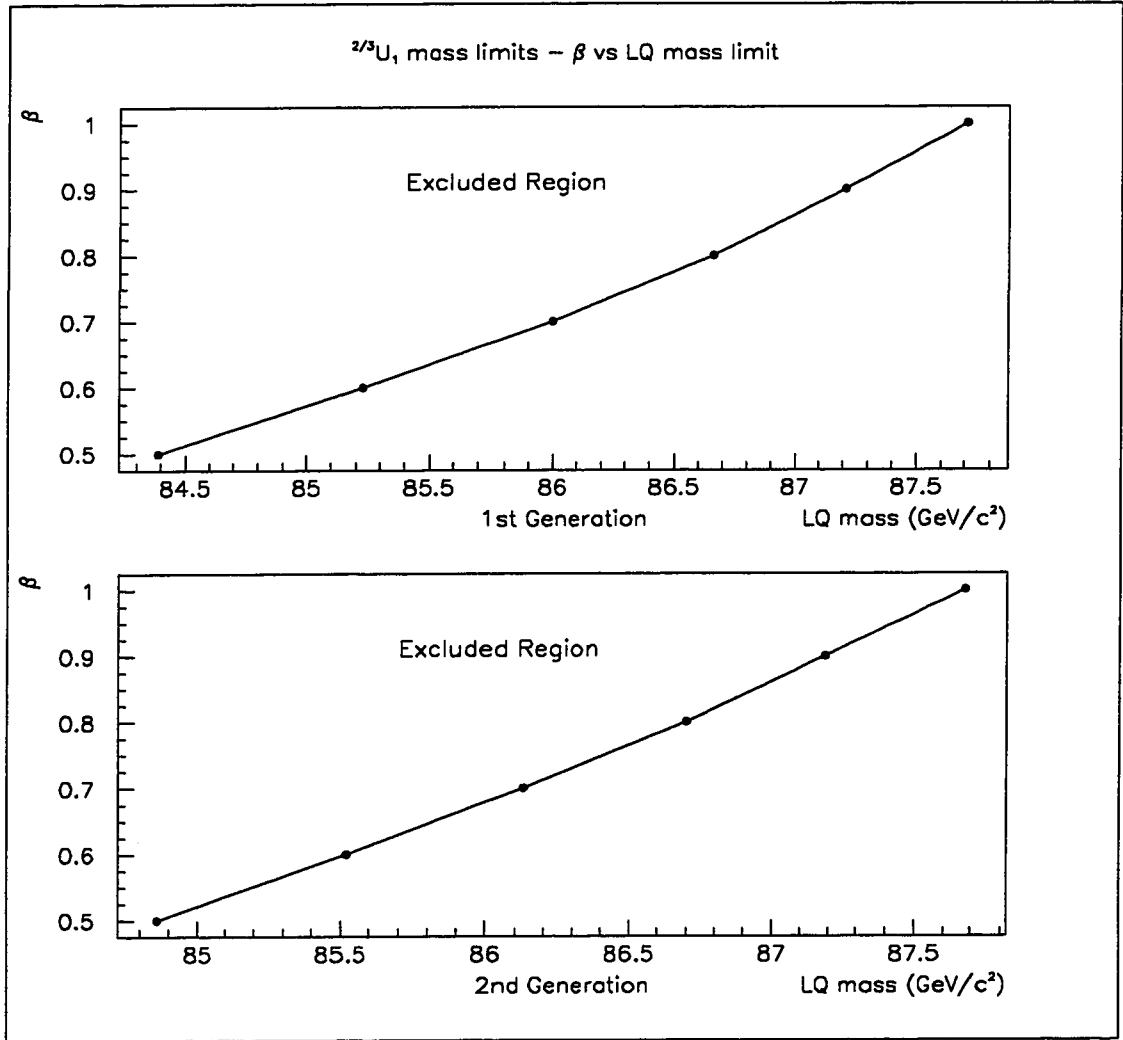


Figure 6.7:  $\beta$  versus lower limit on the mass of the vector leptoquark  $^{2/3}U_1$ , for both first- and second-generation at the 95% confidence level.

### 6.2.3 Upper Limit on Production Cross-Section as a Function of $\beta$ .

We can also determine upper limits on the production cross-section for pair-produced vector leptoquarks, as a function of  $\beta$ , at the 95% confidence level. However, it is necessary to specify a leptoquark mass, because the upper limits are dependent on the signal efficiencies, which vary with mass. The signal efficiencies used were those for leptoquark masses of 85 GeV/c<sup>2</sup> (Figure 6.8) and 90 GeV/c<sup>2</sup> (Figure 6.9), because we have excluded all vector leptoquarks below 84 GeV/c<sup>2</sup>. For these masses, the upper limit on the cross-section is less than 0.4 pb for all values of  $\beta$ .

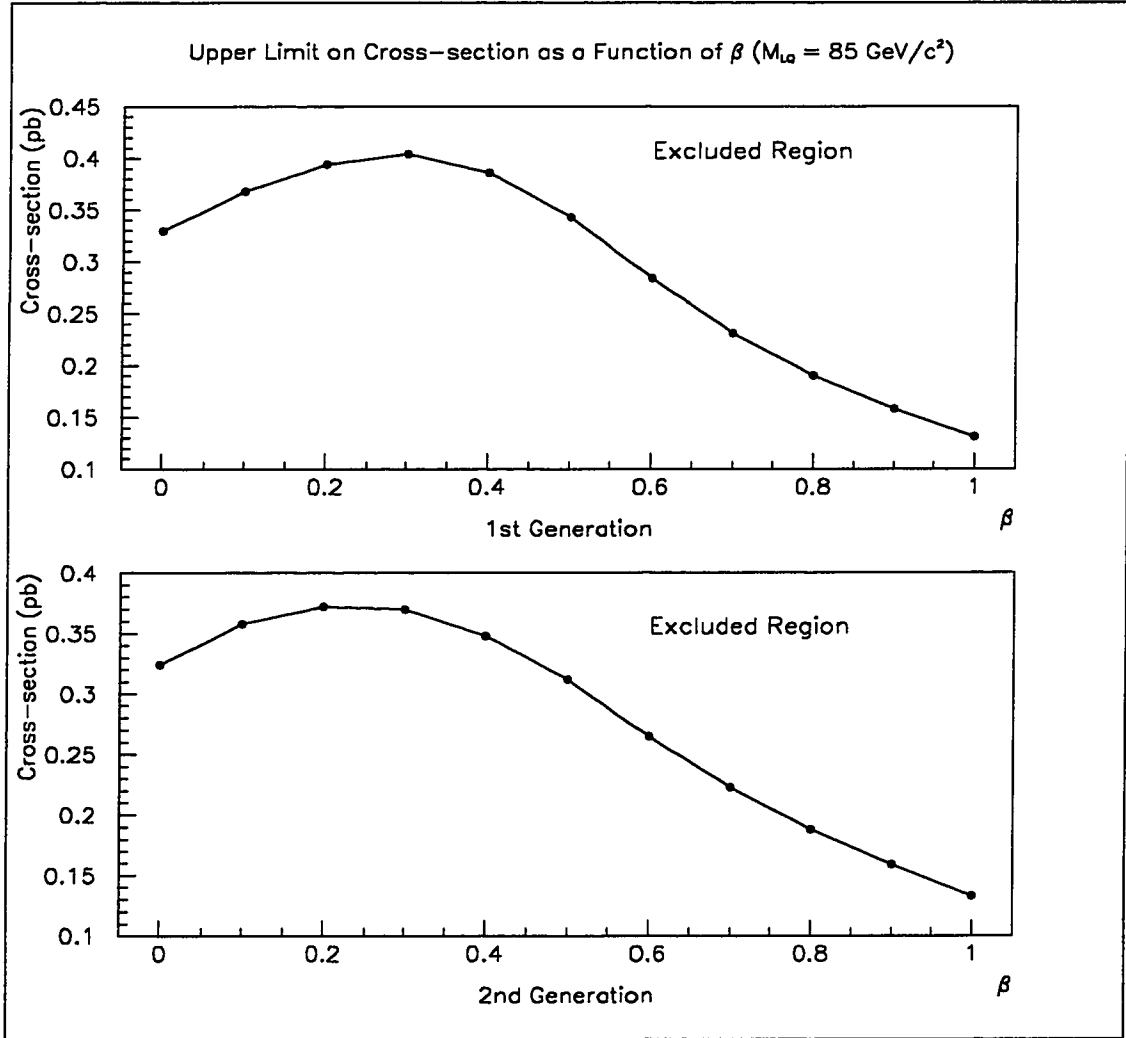


Figure 6.8: Upper limit on the production cross-section versus  $\beta$ , for both first- and second-generation leptiquarks, at the 95% confidence level, assuming a leptiquark mass of  $85 \text{ GeV}/c^2$ .

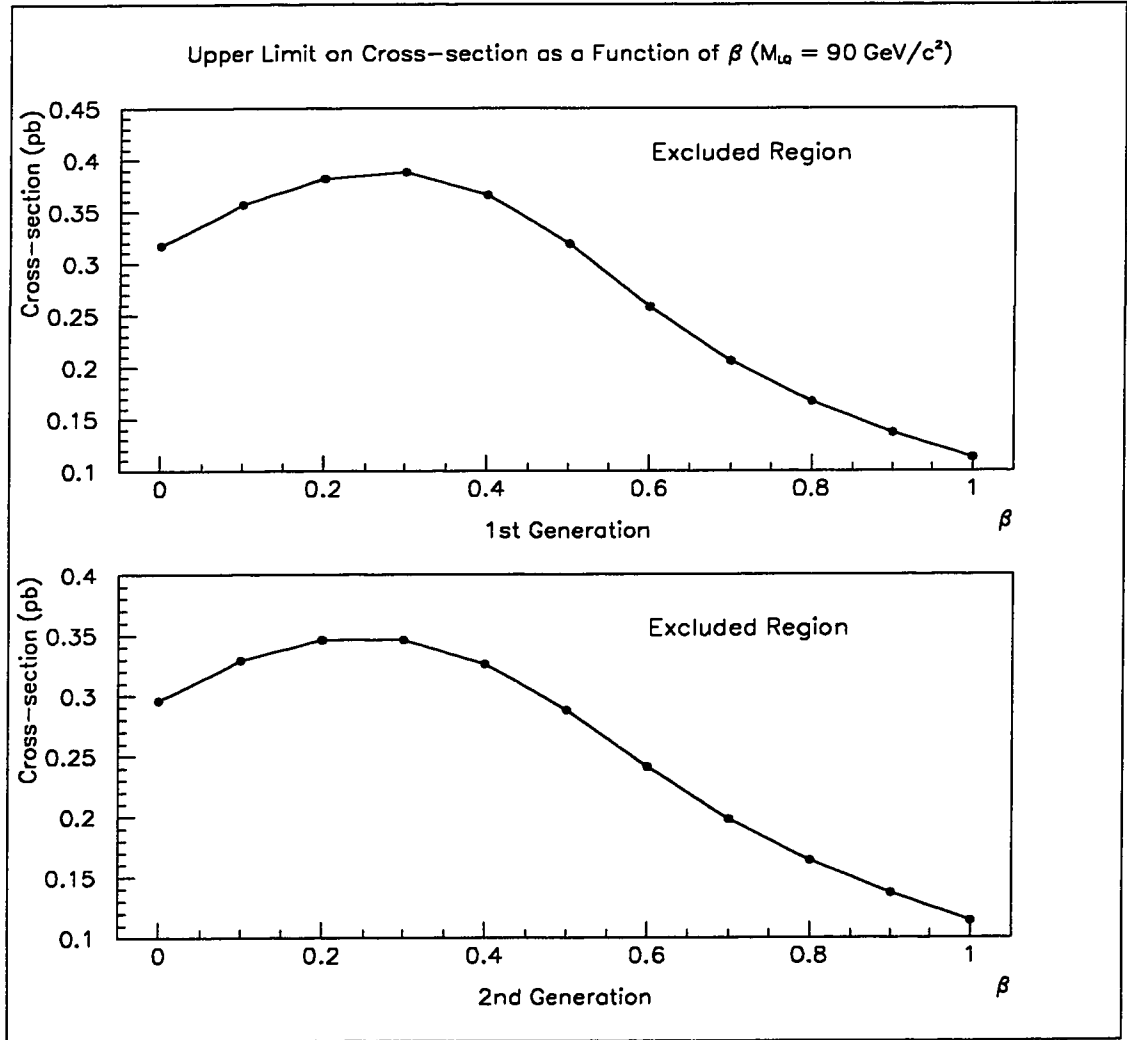


Figure 6.9: Upper limit on the production cross-section versus  $\beta$ , for both first- and second-generation leptoquarks, at the 95% confidence level, assuming a leptoquark mass of  $90 \text{ GeV}/c^2$ .

## 6.3 Discussion of Uncertainties

In this section we discuss the uncertainties present in the analysis. One source of uncertainty in the signal simulation arises because the angular distributions of the vector leptoquark decay products were not correctly simulated. Vector leptoquarks have a particular spin direction. (This is not the case for scalar leptoquarks.) The spin should be taken into account when a vector leptoquark decays into a lepton and a quark, but the angular distribution of vector leptoquark decays was assumed to be flat in the leptoquark's rest frame.

If one were to sum over all the possible final spin states, the dependence of the angular distribution on the spin direction would be removed; that is, the distribution should be flat in solid angle, according to Equation 2.2.5.21.

One could generate vector leptoquarks with a particular spin direction, and then allow the leptoquarks to decay starting from this state of the spin. To do this on an event by event basis, one must know the cross-section for the production of a vector leptoquark in a particular state of spin. Future vector leptoquark generators should incorporate these details.

Another source of uncertainty in the signal simulation may arise because the leptoquarks were made to decay prior to fragmentation (which is the formation of a jet of particles). It is possible that the leptoquark couplings to fermions could be small enough to allow the leptoquarks to begin fragmentation before they decay. This possibility has not been considered here. It could be included in future vector leptoquark generators. If leptoquarks do fragment before they decay, we estimate a systematic error of 10% in our results. This uncertainty is not included in our limit calculations, because it is based on previous leptoquark simulation studies [16] at

lower energies, in which leptoquarks were allowed to fragment before they decay.

The theoretical cross-sections for vector leptoquark pair-production are assumed to be correct. Different production cross-sections would change the mass limits obtained.

## CHAPTER 7

### Summary

A search for vector leptoquarks of the first- or second-generation in electron-positron collisions at a centre-of-mass energy of 183 GeV was performed using data collected by the OPAL detector at LEP.

Our search yielded a total of 8 candidate events. The Standard Model background expectation is 8.7 events. Since the number of events found is consistent with the Standard Model background, there is no evidence for the production of leptoquarks in the data.

Upper limits were placed on the production cross-section for pair-produced vector leptoquarks, for various values of the branching fraction  $\beta$ , and for various leptoquark masses.

Mass limits were obtained for all nine vector leptoquark species, and in all cases, first- and second-generation vector leptoquarks have been excluded at masses below 84 GeV/ $c^2$ , at the 95% confidence level.

Pair-produced vector leptoquarks have not previously been searched for in OPAL data. The mass limits obtained are thus the first for pair-produced vector leptoquarks at OPAL. The most recent search for pair-produced scalar leptoquarks at OPAL [16] placed lower limits on the mass between 53 and 73 GeV/ $c^2$  at the 95% confidence level, for various leptoquark species.

Searches by other experiments are sensitive to either the value of the branching fraction  $\beta$  or to the magnitudes of the couplings of leptoquarks to fermions ( $\lambda_{L,R}$ ). Our results are not as sensitive to  $\beta$  or  $\lambda_{L,R}$ , and thus we have improved the mass limits for certain regions of these parameters.

In the low  $\beta$  region, we have achieved significantly better mass limits than those obtained by other experiments. The most recent results from Fermilab (for scalar leptoquarks) place an upper limit on the leptoquark mass of  $79 \text{ GeV}/c^2$  for  $\beta = 0.0$ , at the 95% confidence level.

The HERA experiments are sensitive to the magnitude of the couplings  $\lambda_{L,R}$ . For small values of  $\lambda_{L,R}$ , the HERA lower limits on the leptoquark mass are as low as  $50 \text{ GeV}/c^2$ , depending on the type of leptoquark.

Continued increases in LEP energies in the next few years will facilitate coupling-independent searches for leptoquarks with higher masses. Future colliders, such as the Large Hadron Collider (LHC) planned for CERN, will be able to search for leptoquarks with a discovery reach of  $1 \text{ TeV}$  [58]. At Fermilab, the experiments D0 and CDF, which use the Tevatron collider, will continue to increase their mass limits with the collection of more data [59]. An increase in HERA energies will result in leptoquark production cross-sections which are 2 to 6 times greater than at present. This will allow for an increase of about  $40 \text{ GeV}/c^2$  on the mass limit [60].

## Bibliography

- [1] J.L. Hewett, “The Standard Model and Why We Believe It”, SLAC-PUB-7930 (hep-ph/9810316) (1998);  
S.L. Glashow, Nucl. Phys. **22** (1961) 579;  
A. Salam, “Elementary Particle Theory”. N. Svartholm editor, Almquist and Wiksell, Stockholm (1968);  
S. Weinberg, Phys. Rev. Lett. **19** (1967) 1264;  
H. Fritsch, M. Gell-Mann & H. Leutwyler, Phys. Lett. **B47** (1973) 365.
- [2] C. Bouchiat, J. Iliopoulos & P. Meyer, Phys. Lett. **38B** (1972) 519.
- [3] J.L. Hewett & T.G. Rizzo, Phys. Rep. **183** (1989) 193.
- [4] J.C. Pati & A. Salam, Phys. Rev. **D10** (1974) 275.
- [5] E. Farhi & L. Susskind, Phys. Rep. **74** (1981) 277.
- [6] B. Schrempp & F. Schrempp, Phys. Lett. **B153** (1985) 101;  
W. Buchmüller, Acta. Phys. Austr. Suppl. **XXVII** (1985) 517.
- [7] W. Buchmüller & D. Wyler, Phys. Lett. **B177** (1986) 377.
- [8] W.C. Louis *et al.*, Phys. Rev. Lett. **56** (1986) 1027.
- [9] Particle Data Group, Review of particle properties, Rev. Mod. Phys. **56** (1984) no. 2, part II.
- [10] J. Blümlein & R. Rückl, “Production of Scalar and Vector Leptoquarks in  $e^+e^-$  Annihilation”, Phys. Lett. **B304** (1993) 337.

- [11] B. Schrempp, Leptoquarks and Leptogluons at HERA - Theoretical Perspectives, Physics at HERA, Proceedings of the Workshop, 29-30 Oct. 1991, Hamburg, W. Buchmüller & G. Ingelman, editors, Vol. 2, pp. 1034-1042.
- [12] OPAL Collab., G. Alexander *et al.*, **B263** (1991) 123.
- [13] ALEPH Collab., D. DeCamp *et al.*, Phys. Rep. **216** (1992) 253.
- [14] DELPHI Collab., P. Abreu *et al.*, Phys. Lett. **B275** (1992) 222.
- [15] L3 Collab., D. Adeva *et al.*, Phys. Lett. **B261** (1991) 169.
- [16] OPAL Collab., K. Ackerstaff *et al.*, OPAL Physics Note PN300 (1997).
- [17] OPAL Collab., K. Ackerstaff *et al.*, OPAL Physics Note PN288 (1997), paper LP138 submitted to the XVIII International Symposium on Lepton-Photon Interactions, Hamburg, 1997.
- [18] CDF Collab., F. Abe *et al.*, Phys. Rev. **D48** (1993) 3939;  
CDF Collab., F. Abe *et al.*, Phys. Rev. Lett. **75** (1995) 1012.
- [19] D0 Collab., S. Abachi *et al.*, Phys. Rev. Lett. **72** (1994) 965;  
D0 Collab., S. Abachi *et al.*, Phys. Rev. Lett. **75** (1995) 3618.
- [20] CDF Collab., F. Abe *et al.*, FERMILAB-PUB-97/280-E (1997).
- [21] D0 Collab., B. Abbott *et al.*, FERMILAB-PUB-97/252-E (hep-ex/9707033) (1997).
- [22] D0 Collab., B. Abbott *et al.*, FERMILAB-PUB-97/344-E (hep-ex/9710032v2) (1997).
- [23] ZEUS Collab., M. Derrick *et al.*, Phys. Lett. **B306** (1993) 173.

- [24] H1 Collab., T. Ahmed *et al.*, Z. Phys. **C64** (1994) 545;  
H1 Collab., S. Aid *et al.*, Phys. Lett. **B369** (1996) 173.
- [25] D. Bowser-Chao, T.D. Imbo, B.A. King & E.C. Martell, UICHEP-TH/97-13  
(hep-ph/9803348v3) (1998).
- [26] OPAL Collab., K. Ahmet *et al.*, Nucl. Instr. and Meth. **A305** (1991) 275.
- [27] P.P. Allport *et al.*, Nucl. Instr. and Meth. **A324** (1993) 34.
- [28] OPAL Collab., K. Ackerstaff *et al.*, OPAL Technical Note TN524 (1997).
- [29] P.P. Allport *et al.*, Nucl. Instr. and Meth. **A346** (1994) 476.
- [30] J.R. Carter *et al.*, Nucl. Instr. and Meth. **A286** (1990) 99.
- [31] O. Biebel *et al.*, Nucl. Instr. and Meth. **A323** (1992) 169.
- [32] M. Hauschild *et al.*, Nucl. Instr. and Meth. **A314** (1992) 74.
- [33] H. Mes *et al.*, Nucl. Instr. and Meth. **A265** (1988) 445.
- [34] J.D. Hobbs *et al.*, Nucl. Instr. and Meth. **A325** (1993) 494.
- [35] S. Dado *et al.*, Nucl. Instr. and Meth. **A252** (1986) 511.
- [36] J. Allison *et al.*, Nucl. Instr. and Meth. **A236** (1985) 284.
- [37] OPAL Collab., G. Alexander *et al.*, Z. Phys. **C52** (1991) 175.
- [38] B.E. Anderson *et al.*, IEEE Trans. on Nuclear Science, **41** (1994) 845.
- [39] M. Arignon *et al.*, Nucl. Instr. and Meth. **A313** (1992) 103.
- [40] D.M. Gingrich, in “Physics at LEP2”, CERN Yellow Report, Vol. 2, Geneva  
(1996) 345.

- [41] T. Sjöstrand, "PYTHIA 5.721 and JETSET 7.408 Generators", *Comp. Phys. Comm.* **82** (1994) 74.
- [42] J. Blümlein, "Radiative Corrections to Leptoquark Pair Production in  $e^+e^-$  Annihilation", DESY 93-153 (1993).
- [43] J. Allison *et al.*, *Nucl. Instr. and Meth.* **A317** (1992) 47.
- [44] "GEANT Detector Description and Simulation Tool", CERN Program Library Long Writeup W5013 (1994).
- [45] R. Engel & J. Ranft, *Phys. Rev.* **D54** (1996) 4244;  
R. Engel, *Z. Phys.* **C66** (1995) 203.
- [46] G. Marchesini, B.R. Webber, G. Abbiendi, L.G. Knowles, M.H. Seymour & L. Stanco, *Comp. Phys. Comm.* **67** (1992) 203.
- [47] J.A.M. Vermaseren, *Nucl. Phys.* **B229** (1983) 347.
- [48] J. Fujimoto *et al.*, KEK-CP-046 (1996).
- [49] T. Omori, S. Asai, I. Nakamura & S. Yamashita, "A Matching Algorithm: MT Package", OPAL Technical Note TN381 (1996).
- [50] S. Catani *et al.*, *Phys. Lett.* **B269** (1991) 432.
- [51] OPAL Collab., K. Ackerstaff *et al.*, *Phys. Lett.* **B389** (1996) 416.
- [52] L. Brigliadori, private communication (1998).
- [53] G.J. Feldman & R.D. Cousins, *Phys. Rev.* **D57** (1998) 3873.
- [54] C. Caso *et al.*, *The European Physical Journal* **C3** (1998) 1.
- [55] V.F. Obraztsov, *Nucl. Instr. and Meth.* **A316** (1992) 388.

- [56] G. Zech, Nucl. Instr. and Meth. **A277** (1989) 608.
- [57] R.D. Cousins & V.L. Highland, Nucl. Instr. and Meth. **A320** (1992) 331.
- [58] B. Dion, L. Marleau, G. Simon & M. de Montigny, The European Physical Journal **C2** (1998) 497.
- [59] J. Blümlein, E. Boos & A. Kryukov, DESY 97-067 (hep-ph/9811271) (1998).
- [60] M. Botje & G. Wolf, DESY-98-140 (hep-ex/9809027) (1998).